UNIVERSITY OF LIVERPOOL

CHARGE TRANSPORT AND ACCUMULATION AROUND HVDC INSULATORS

A thesis presented in fulfilment of the requirement for the degree of

Doctor of Philosophy

Qingying Liu

September 2017

Department of Electrical Engineering and Electronics

The University of Liverpool

Declaration of Authenticity and Author's Rights

‘This thesis is the result of the author’s original research. It has been composed by the author and has not been previously submitted for examination which has led to the award of a degree.’

Signed:

Date:

ACKNOWLEDGEMENTS

I would firstly like to thank Professor Jiu Dun (Joseph) Yan for his continuous supervision, guidance and encouragement throughout the course of this study. His rigorous research attitude and strong commitments to excellence in research have set a good example for me and inspired me to pursue the extraordinary in my future career.

I would also like to express my gratitude to Professor Michael Fang for the opportunity, his support and encouragement. Many thanks to Dr James Walsh for his invaluable technical input provided throughout the study. Many thanks to Dr Lei Su and Dr Lin Jiang for their continuous help whatever in research or life.

I also wish to thank the Department of Electrical Engineering and Electronics for the use of departmental facilities and a scholarship and the enthusiastic support from staff members in the Departmental Office throughout my study.

My special appreciation is addressed to Pinggao Group Co Ltd, State Grid Corporation of China (SGCC) for their financial support.

Lastly, I would also like to thank my family and friends for their love and continuous support in my life.

ABSTRACT

High voltage direct current (HVDC) based transmission of electric power, in comparison with high voltage alternating current (HVAC) transmission over a distance of over 800 km, has the advantages of higher transmission capability, lower line loss, more confined damage by fault, and that all AC lines connected to an HVDC system do not need to be synchronized. However, under DC conditions the electric field across the insulation space remains unidirectional and stable, which results in charge accumulation, leading to significant differences in the dielectric behavior and flashover characteristics of insulation materials in comparison with those under AC conditions. There exists limited amount of test data and research results on HVDC insulation behaviour. It is therefore necessary to carry out in-depth study of the discharge mechanisms and behavioral characteristics of the insulation materials required for HVDC transmission systems.

The research in this thesis aims at the understanding of the charge transport and accumulation process inside and around insulators made of epoxy composite material. Firstly, the physical mechanisms are critically reviewed with appropriate experimental results selected for model verification. The model developed in the work encompasses all important mechanisms. Material properties obtained under different conditions are reviewed and values for the cases investigated in the present work determined. Charge transport is dominated by the drift of two types of oppositely charged particles in electric field with nonlinear generation source terms, giving rise to extreme difficulties for convergence of computation in strong electric field. As a result, special code is developed for a commercial software package (COMSOL based on finite element method) to implement the model and also the complicated boundary conditions. To gain confidence in the model and its implementation including the boundary conditions and material properties the model is verified in the work against experimental cases with different gas, geometry and applied voltage. An experimental study of the effect of surface charge accumulation on the potential distribution along the surface of an epoxy insulator under HVDC stress was carried out under non-ideal conditions.

Contents

List of Abbreviations

AC	Alternating current
BEM	Boundary element method
DC	Direct current
DR	Dielectronic recombination
FEM	Finite element method
GIS	Gas insulated switchgear
HVDC	High voltage direct current
HVAC	High voltage alternating current
IGBT	Insulated gate bipolar transistor
JFET	Junction gate field-effect transistor
MI	Mass impregnated insulation
MTDC	Multi-terminal direct current
OSFET	Odor-sensitive field effect transistor
PDE	Partial differential equation
RR	Radiative recombination
TBR	Three body recombination
XLPE	Crosslinked polyethylene
ns	Nanosecond

List of Symbols

ρ	Charge number density
ε	Permittivity
ε_0	Vacuum permittivity
σ	Conductivity
En	Normal component of electric field
Et	Tangential component of electric field
e	Electric charge
μ	Mobility of charge carrier
V	Velocity
L	Mean free path
D	Diffusion coefficient
K_r	Recombination coefficient
k	Boltzmann constant
E	Electric field
P	Polarization
J	Current density
D	Electric flux density

CHAPTER 1 INTRODUCTION TO HIGH VOLTAGE DIRECT CURRENT POWER TRANSMISSION AND OBJECTIVES OF RESEARCH

High voltage direct current (HVDC) technology is one of the technical options and preferable choices for the bulk long-distance power transmission system. In an AC (alternating current) system, voltage conversion is simple, an AC transformer allows high voltage levels, so that is AC technology was introduced at very early stage in the development of electrical power systems. However, traditional AC transmission has problems of synchronisation and extra connectors (cost) for three phases. And within electronic devices have been developed to make it cost effective to change DC voltage levels. For large distances it is now more cost effective to transmit power using DC rather than AC.

This chapter provides an overview of HVDC technology and the situation in which it is applied. It consists of five sections. Section 1.1 presents an overall background information of HVDC power transmission, the core technology and the development. Section 1.2 introduces the insulation application in the HVDC transmission system. Existing disadvantages and challenges are concluded and analysed in Section 1.3. Section 1.4 introduces the objectives and major contribution in the work. The organization of thesis is presented in the final section 1.5.

1.1 High Voltage Direct Current Power Transmission

DC power generation and distribution first appeared in 1882 at a voltage of only 110 V [1.1]. It soon lost to AC technology in the War of Currents around 1890 largely because there was no practical means to change the DC voltage. As a result, AC technology dominated the electricity industry over the next 100 years and the transmission voltage level increased steadily to 750 kV in 1965 [1.2] and has reached 1100 kV nowadays. Although DC technology was used in specific applications, its

voltage level remained around 100 kV until 1970. With the increase in power demand in developing countries and recent worldwide exploitation of renewable energy resources, long distance and more efficient transmission lines at elevated voltage levels are required to accommodate remote power generation and interconnection. The development in high voltage power electronics technology in the past 50 years [1.3], especially the thyristor valve technology in the past 15 years [1.4], provided core technological support to the installation of high voltage direct current (HVDC) transmission lines with much increased capacity. More than 20 lines have already been installed at a voltage level of 800 kV or above with relatively long transmission distances (> 600 km). Most of the lines above 750 kV were installed in the past ten years [1.2]. Among the countries of large geographical areas, China has the longest HVDC link (800 kV/6400 MW/2071 km), connecting the Xiangjiaba Dam Hydropower Plant with Shanghai [1.2]. A typical HVDC system is shown in Figure 1-1.

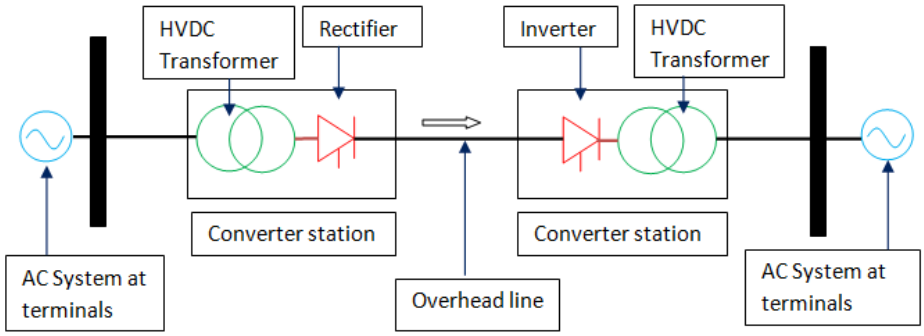

Figure 1-1 Simplified HVDC system [1.5].

There are several main components, i.e. the terminals, transformers, rectifiers and transmission medium. The core process involved in the operation of a converter at the sending terminal acts as a rectifier and converts the AC power into DC and a converter at the receiving terminal acts as an inverter and converts the DC power into AC. This is realized by the use of power electronics devices such as thyristor and IGBT (insulated gate bipolar transistor), and the working principle including PNP and NPN transistors, JFET and OSFET is shown in Figure 1-2. Thyristors are used as switches

and thus the valve becomes controllable. The thyristors are made of highly pure mono-crystalline silicon. Present the maximum individual thyristor ratings are typically 8 kV /6 kA (12 kV thyristors are available but at a reduced current rating of 2.4 kA) [1.6]. Such kind of thyristor devices are light triggered so as to provide electrical isolation of the gate circuitry and to reduce the complexity of firing circuits. They can provide lower conduction and switching loss. IGBT are widely used in commercial voltage source HVDC schemes owing to the lower voltage and power ratings than thyristors (IGBTs are presently available with typical ratings of 4.5 kV/2.4 KA. Higher IGBT voltage ratings are available but with lower current ratings). The advantage of the IGBT over the thyristor is its controlled turn-off capability. The disadvantage is higher switching and conduction losses. On the other hand, in addition to providing voltage transformation between the converter AC terminals and the interconnected AC system the converter transformer provides the correct phase relationship and phase arms for connection to the converter valves strings.

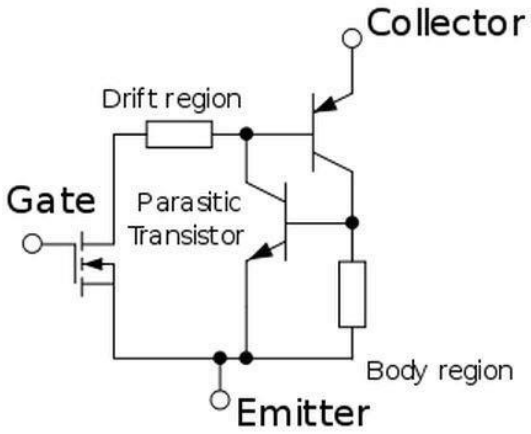

Figure 1-2 Simple circuit diagram of an IGBT.

There are two types of transmission cable technology suitable for use in HVDC application, crosslinked polyethylene (XLPE) and mass impregnated (MI) insulation, as shown in Figure 1-3. All cables consist of a copper or aluminum conductor surrounded by a layer of insulation (the thickness of which is dependent upon the operational voltage), as marked in Figure 1-3(b), a metallic sheath to protect the cable

and prevent moisture ingress and a plastic outer coating.

(a) *(b)*

Figure1-3 Typical cable system in HVDC transmission, (a) MI cable and (b) XLPE cable [1.7].

For single polarity HVDC transmission, only a single conductor is needed when the current is returned through earth, occupying potentially less space in the transmission corridor, as can be seen in Figure 1-4. The insulators have to perform satisfactorily under all weather conditions and fixed direction of electric field. The cost of any transmission system depends on a wide variety of factors such as the power rating, converter design, compensation requirements, losses and the type of transmission medium. Figure 1-5 presents a cost comparison with high voltage alternating current (HVAC) technology as a function of transmission distance. It can be seen that there is a "break-even distance" associated with the cost differentials between technically equivalent AC and DC transmission links. At present "break-even distances" in comparison with their HVAC equivalent for HVDC overhead transmission system are quoted at around 600-800 km [1.7].

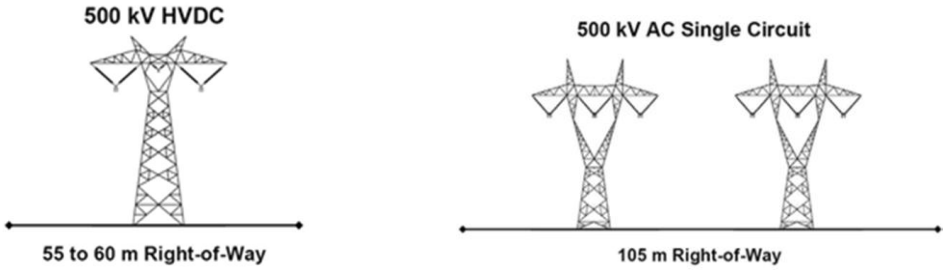

(a) *(b)*

Figure 1-4 Comparison between HVDC and HVAC land use.

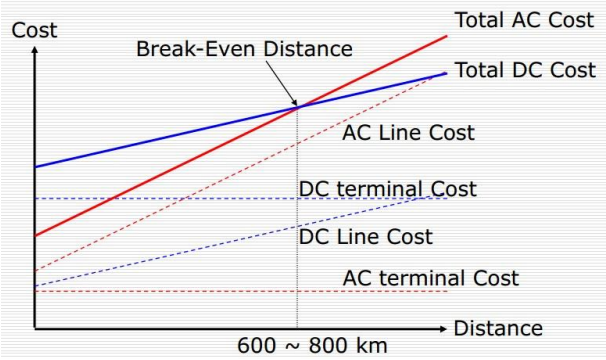

Figure 1-5 Diagram showing the cost variation of HVAC and HVDC systems as a function of transmission distance using bare conductors. It must be noted that the actual absolute cost depends on the material and component price, type of design and geographical location of the transmission corridor [1.5].

Altogether, compared with the HVAC technology, HVDC has many distinct advantages, as detailed below:

- Despite the more expensive terminal convertor devices used in the HVDC system, HVDC provides an overall saving in cost for transmission distances above the so called “break-even distance” (600 km to 800 km) [1.5]. This is due to the fact that HVDC only requires a single live conductor for each polarity, thus a lower profile of wiring and pylons for a given power transmission capacity. A HVDC line also experiences less corona losses compared to HVAC transmission lines of similar power.

- A HVDC system enables power transmission between unsynchronized AC power systems, increasing the stability of an AC dominated power grid.
- A HVDC system is better suited for distribution systems where undersea cables are required causing less power losses compared with AC systems.
- It can be used to increase the capacity of an existing power grid in situations where additional wires are difficult or expensive to install.
- The short circuit current level in transmission networks with an HVDC line as the main link is rather limited. This is due to the "fixed current control" nature of the HVDC system.

Based on these advantages, existing HVDC transmission applications can be broken down into the following different categories [1.8,1.9] with examples given below.

1) Long-distance bulk power transmission

Generally, it is getting difficult to build overhead lines owning to the complicated landscape configuration, public resentment and political resistance. People often worry about the possible health hazards of living close to overhead lines. In comparison, HVDC technology often provides a more economical alternative to HVAC transmission to transmit large capacity of electricity generated remotely (from the consumption center), such as hydroelectric developments, off shore power plants or large-scale wind farms. Bipolar HVDC lines are comparable to a double circuit AC lines since they can operate at half power with one pole out of service but require only one-third the number of insulated sets of conductors as a double circuit AC line.

2) Underground and submarine cable transmission

HVDC cable system does not have the distance limitations or suffer the higher losses of AC cable systems. Therefore, long distance HVDC cable transmission is possible. Extruded HVDC cables are lighter, more flexible and easier to splice than the oil-paper cables used for conventional HVDC transmission thus making them more convenient for land cable applications where transport limitations can drive up cost. The lower cost cable installations made possible by the extruded HVDC cables makes long distance underground transmission economically feasible for use in areas with low constraints. Furthermore, there is a drop-off in cable capacity with AC transmission

over distance due to its reactive component of the charging current. Although this can be compensated by intermediate shunt compensation for underground cables at increased expense, it is not practical to do so for submarine cables.

3) Asynchronous ties

With HVDC transmission systems, interconnections can be made between asynchronous networks for more economic or reliable system operation. The asynchronous interconnection allows interconnections of mutual benefits while providing a buffer between two systems. Often these interconnections use back to back converters with no transmission line in between. For instance [1.5], in Queensland, Australia, HVDC was chosen in an international project to interconnect two independent grids (of New South Wales and Queensland) to: enable electricity trading between the two systems (including change of direction of power flow).

4) Offshore transmission

In many cases, offshore transmission is better suited to HVDC applications than traditional AC. Using AC, offshore cable voltage is limited to 229 kV [1.5], limiting power transfer capabilities unless many cables are used. Also, lengths of AC cable are very difficult and expensive to joint offshore and reactive compensation cannot be installed mid-route, so transmission distance are restricted. Offshore cable installation, for both AC and HVDC requires the use of specially designed cable-laying ships or barges. To protect the cables from anchor strikes, they are preferably buried in the sea bed.

1.2 Insulation in HVDC

Insulators are essential components in an electrical power system. They need to provide adequate mechanical support and electrical insulation to conducting materials under all environmental and operational conditions. The most widely used materials for insulators are porcelain, glass and composite materials. A classification of the types of insulator is shown in Figure 1-6. With the increase of voltage levels in HVDC transmission, reliable insulators of higher electrical and mechanical performances and

minimal overall size are required.

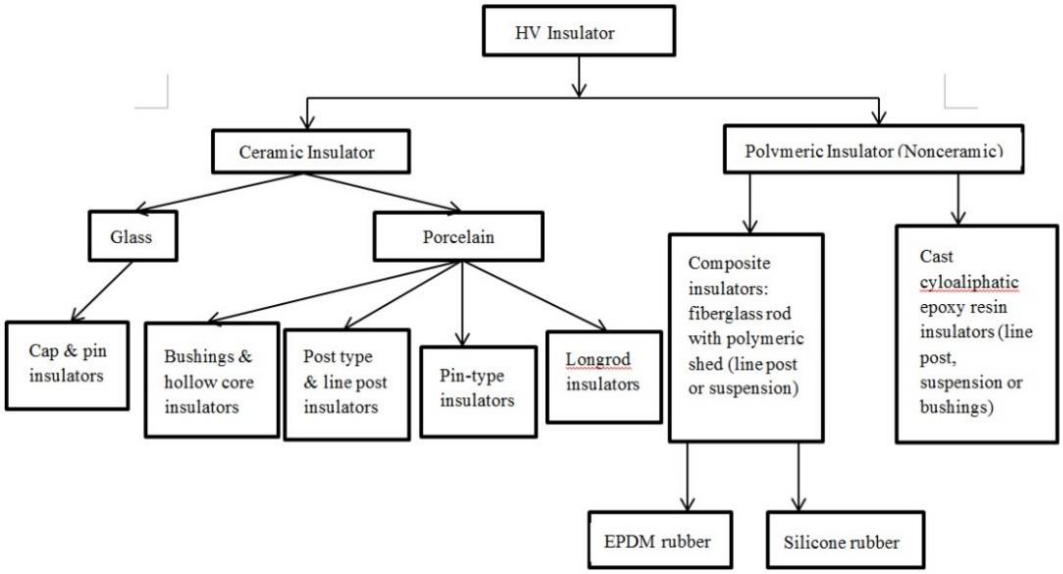

Figure 1-6 Classification of commonly used HVAC and HVDC insulators according to insulation material[1.8-1.10].

The structure of cap-pin insulator can be seen in Figure 1-7 (a) [1.10]. The cap-pin insulators are made of galvanized malleable iron pins and caps with Portland cement mortar and can be divided into two groups, non-stacking and stacking units. The non-stacking insulators contain one piece of shed between one pair of electrodes, while the stacking units have multi-piece sheds between one pair of electrodes. Compared with the cap-pin insulators, the rod insulators have better insulation performance on the surface flashover, as shown in Figure 1-7 (b). Owing to the increased leakage distance, the rod insulators can withstand serious pollution, especially in the wet environment.

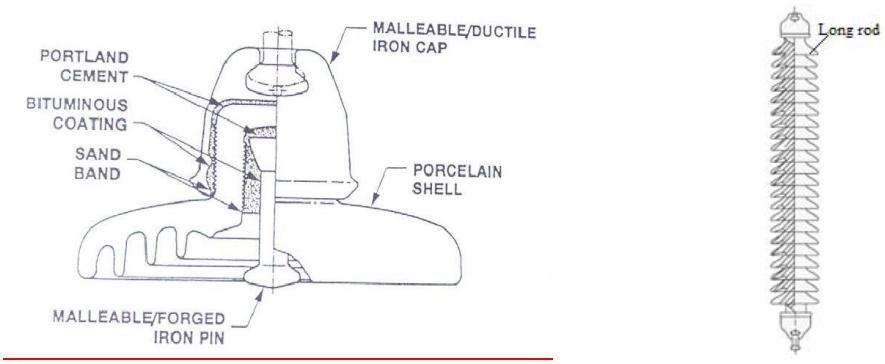

(a) *(b)*

Figure 1-7 (a) The schematic structure of cap-pin insulators and (b) is the structure of long rod suspension insulator [1.10].

HVDC wall bushing is a special type of insulator which provides electrical insulation to a central conductor at high voltage from the earthed middle section of the bushing barrel where contact with wall is needed. A typical SF_6 filled wall bushing manufactured by ABB [1.11] is shown in Figure 1-8. It can be horizontally or vertically installed or installed at any intermediate angles. The weight can be up to 1250 kg and 10 meters in total length.

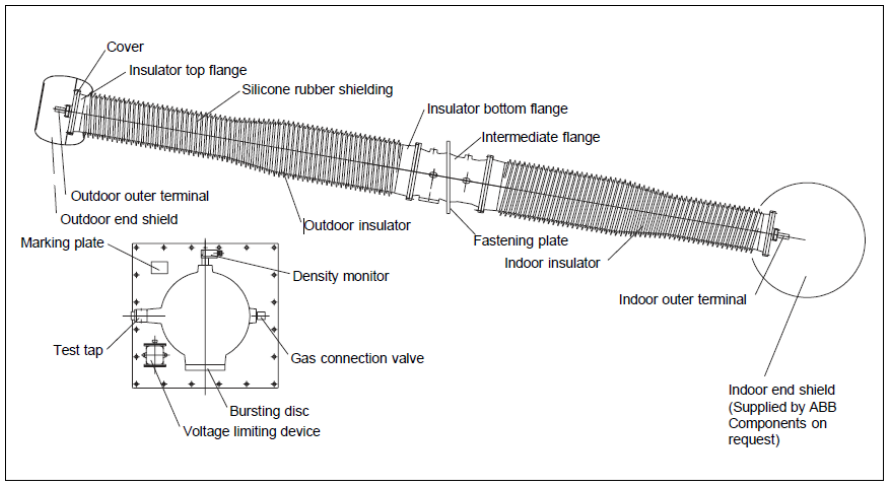

Figure 1-8 External profile of an ABB 400 kV/ 3.12 kA gas filled DC wall bushing [1.11].

The schematic diagram of a Pinggao 1100 kV HVDC bushing insulator is given in Figure 1-9. The bushing has an overall length of 27.93 m (including the two terminal rings). The gas tight bushing structure is filled with SF_6 at 6 bar (absolute) to provide insulation between the central conductor and the bushing walls. The inner diameter of the middle barrel of the bushing (where the intermediate flange is), which is metallic and to be fitted into the wall, is 1.35 m. The maximum potential difference is between the live central conductor and the earthed metallic wall of the barrel. The supporting rod insulator, also called the spacer as marked in Figure 1-9 (b), has to provide sufficient mechanical strength to hold the central conductor firmly in its intended position and at the same time provide adequate insulation between the live conductor and the earthed wall, as shown in Figure 1-9 (a). On each side, there is an insulator consisting of the central conductor, field shielding arrangement, and an insulation tube made of glass fiber reinforced epoxy with silicone rubber shielding. The electric design will need to ensure that local electric field enhancement is minimized to achieve the smallest possible overall dimensions for a given voltage and current rating. This can only be achieved through a clear understanding of the dielectric behavior of the insulation system under practical conditions, which is the object of the present work. The work in this project focuses on the calculation of electric and thermal field distribution inside the bushing structure, taking into account of surface charge accumulation, to support the design of HVDC wall bushings at Pinggao Group Co. Ltd.

(a) *(b)*

Figure 1-9 Schematic diagram of an HVDC bushing insulator (a) and part of its internal structure (b). A rod insulator (the spacer) is used to provide mechanical support to the central conductor.

1.3 Challenges in HVDC Technology

Although HVDC power system has been in use for over 100 years, there are still huge challenges in its application and operation. The first challenge is the efficient conversion between AC and DC to reduce the size and cost of the converter station. The second challenge is the long-term reliability of the power electronics devices continuously operating at high current and switching frequency. The third challenge, which is the focus of the present work, is the long-term dielectric behaviour of the insulators under strong electric field with fixed direction.

There have been many studies on the insulation performance of insulators under HVDC stress, which will be reviewed in Chapter 2. For example, the experimental work in [1.12-1.18] suggests that, for outdoor and external insulators, contaminants can accumulate on the insulator surface as a result of the strong electrical field which is 1.2-1.5 times that on AC insulators under the same operational conditions. In the presence of a local arc, since the DC arc without zero crossing lasts longer than the AC arc, it can potentially bridge the sheds of the insulators and subsequently reduce the flashover voltage of DC insulator strings. In the absence of a complete flashover, a localised DC arc is able to cause the effective leakage distance of the insulators to become less than the geometrical leakage distance. Under polluting and moist weather conditions, the flashover voltage can be 20%-30% lower than that under AC condition.

For internal insulators, the majority of the research attributes the long-term dielectric behaviour change of the insulators to space charge transport and accumulation [1.10,1.12]. The accumulation of space charge results in the distortion of the electrical field and accelerates the aging process. For example, in the case of GIS, it was found that a larger amount of charge was accumulated under DC stress rather than AC stress. The higher quantity of charges accumulated and transport in the dielectrics, the more reduction and rapidly in the surface flashover of approximate DC stress 23% and AC stress 10.2% [1.13, 1.18-1.20]. The insulator surface, which is considered as being the “weakest link” in combined insulation, must have higher breakdown voltage compared with a pure gas gap.

A gas filled HVDC wall bushing has a metallic conductor at its center with high voltage.

The conductor is surrounded by gas and supported by a spacer. A typical example of surface charge distribution is given in Figure 1-10 with the typical geometry with two electrodes embedded into the insulator body used in the investigation. Under long-term DC voltage, charges are always present, following a negative symmetrical distribution to the middle point of the surface length, and the positively charge electrode attract negative charge in the vicinity of the electrode, vice versa. The number density of the charges can be up to 3×10^{-4} C/m^2 with the voltage of 200 kV for 4 hours [1.14,1.21]. Possible causes of surface charge are always considered as follows, for instance, micro discharge or field emission from surface projections, motion of dust particles and neutral ionization of SF_6 gas in prolonged time range. Although there are many research works studied in the surface charge accumulation, however, there are many unanswered questions arising from the practical use of DC insulator within the increase of the voltage level and long-term use.

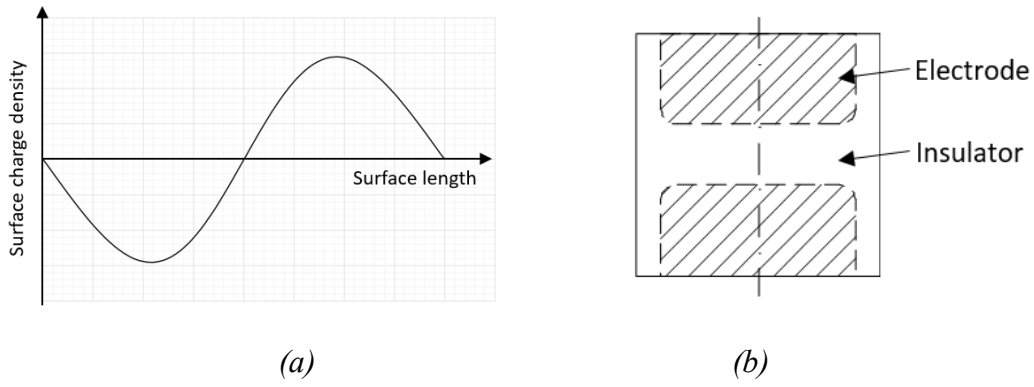

Figure 1-10 (a) Typical surface charge pattern of spacer model and (b) cross-sectional view of the spacer configuration.

1.4 Research Objectives and Major Contributions

As stated above, the long-term performance of insulators under HVDC stress is related to the charge accumulation over the insulator surface which distorts the local electric field and adversely affects the surface flashover field or voltage. This is a practically important subject yet not understood well. Present research is to gain more

understanding and experience of the physical mechanisms and develop a model as a tool to further study the phenomenon and gain verified knowledge. Specifically, the research is aimed at:

1) Researching and understanding the mechanisms responsible for charge transport and accumulation on HVDC insulators and gaining experience of the practical issues that relate to the insulation performance of HVDC insulators.
2) Developing, implementing and verifying a steady state charge transport model for the calculation of electric field around DC insulators. All-important mechanisms must be taken into account. The process of charge transport and accumulation will be taken into account.
3) Investigating the influence of surface layer and its potential use for optimum design of HVDC insulators.
4) The establishment of optimum design principles for HVDC wall bushings based on material property conditioning and geometric dimension optimization.
5) Performing experiment on HVDC insulator under DC stress in different gaseous environment. This is mainly concerned with the measurement of electrostatic potential near the insulator surface under different applied voltages.

The work is financially supported by Pinggao Group Co Ltd, part of State Grid Corporation of China (SGCC), has led to the following achievements:

1) A two-dimensional axisymmetric model has been developed including the charge transport and surface charge accumulation that is able to predict the insulation performance and electric field distribution of the spacer in the wall bushing system. The model is verified using published test and simulation results.
2) The convergence of the solution scheme based on the finite element method (FEM) is studied and the influence of mesh system assessed. It has been found that with strong ion drift flux and weak diffusion, mesh system with extremely small mesh size (typical size of 0.05 mm) is needed for convergence, resulting in huge memory usage and prohibitively long computing time. Divergence often starts at the triple junction where the electric field experiences abrupt

change in space. Three measures have to be taken to ensure computational convergence with acceptable computing time, i.e. 1) optimized mesh system for minimum total mesh number; 2) appropriate artificial diffusion; and 3) physically correct boundary and interface conditions.

3) The mathematical model has been applied successfully to study and predict the charge accumulation behavior of an epoxy space that is used in Pinggao's 1100 kV and 800 kV wall bushing.
4) An experimental characterization of the effect of surface charge accumulation on epoxy insulator under non-ideal conditions has been achieved.
5) Guidance on optimum design of the spacer and electrodes inside a HVDC wall bushing has been established based on the numerical investigation of electric field distribution with different shape of contact. And it has been found that the shielding around the high potential electrode can uniform the electric field distribution in the vicinity region.

1.5 Organization of Thesis

This thesis contains seven chapters. An introduction to the basics of a typical HVDC transmission system, the application areas of HVDC and challenges in HVDC insulation is given in Chapter 1 with the objectives and major achievements of the present work briefly described. Chapter 2 presents a literature review on subjects relevant to the present study, especially the experimental and modelling work on HVDC insulators in relation to charge accumulation and breakdown. Chapter 3 demonstrates the mathematical model considering the charge transport and accumulation process. The ionization, recombination, drift and diffusion influences are reviewed and analyzed. Chapter 4 focuses on the computation accuracy and model implementation. Factors that can influence the accuracy and computational process are analyzed and tested. The computational study of the insulation behavior of epoxy insulator is investigated in Chapter 5 which includes the following aspects: the 3D modelling work, the 2D asymmetric modelling work in the wall bushing. Chapter 6 is the experimental investigation. The work is summarized in Chapter 7, which also includes a proposal for future work.

1.6 Reference

[1.1] K. R. Padiyar, *HVDC Power Transmission Systems: Technology and System Interactions*, New Age International, Inc., India, 1990, Chapter 2.

[1.2] L. Cheng, H. Feng, and J. He, "*HVDC Development and its reliability in China*," in *IEEE Power and Energy Society General Meeting (PES)*, Vancouver, Canada, pp. 1-5, 2013.

[1.3] F. Dijkhuizen, "Recent advances and challenges of power electronics for transmission applications," in 8th Exhibition on Ecological Vehicles and Renewable Energies (EVER) of conf., Monte Carlo, Monaco, 2013, pp. 123-130.

[1.4] H. Huang, M. Uder, R. Barthelmeß, and J. Dorn, "Application of nigh power thyristors in HVDC and FACTS systems," in *17th Electric Power Supply Industry (CEPSI) of conf.*, Macau, 2008. No page information was provided online.

[1.5] R. Rudervall, J.P. Charpentier and R. Sharma, "High voltage direct current (HVDC) transmission system technology review paper," in Energy Week of Conf., Wasington, USA, 2000, pp.1-17.

[1.6] T. Hasegawa, K. Yamaji, H. Irokawa, H. Shirahama, C. Tanaka and K. Akabane, "Development of a thyristor valve for next generation 500 kV HVDC transmission systems," *IEEE Trans. Power Del.,* vol.11, Oct 1996.

[1.7] High Voltage Direct Current Electricity – *Technical Information*. Available: http://www.nationalgrid.com.

[1.8] M.P. Bahrman and B.K. Johnson, "The ABCs of HVDC transmission technologies," *IEEE Power Energy Mag*., vol.5, pp.32-44, 2007.

[1.9] A. Kalair, N. Abas and N. Khan, "Comparative study of HVAC and HVDC transmission systems," *Renewable and Sustainable Energy Reviews*, vol.59, pp.1653-1675, 2016.

[1.10] J. He, "Electric potential and field calculation of HVDC composite insulators by charge simulation method," M.S. thesis, Dept. Elect. Eng., Arizona state Univ., Arizona, USA, 2013.

[1.11] *Gas-insulated wall bushings, type GGFL*. Available: https://library.e.abb.com/public/d715199e8ddc1191c1257b130057ebda/2770%20501-6%20en%20Rev%203.pdf.

[1.12] W. Lampe, T. Höglund, C. Nellis, P. Renner, and R. Stearns, "Longterm tests of HVDC insulators under natural pollution conditions at the big eddy test center," *IEEE Trans. Power Del.,* vol. 4, no. 1, pp.248–259, Jan. 1989.

[1.13] M. Fazelian, C. Y. Wu, T. C. Cheng, H. I. Nour, and L. J. Wang, "A study on the profile of HVDC insulators—DC flashover performance," *IEEE Trans. Elect. Insul.,* vol. 24, no. 6, pp. 119–125, Feb. 1989.

[1.14] K. Naito and H. M. Schneider, "Round-robin artificial contamination test on high voltage DC insulators," *IEEE Trans. Power Del*., vol. 10, no. 3, pp. 1438–1442, Jul. 1995.

[1.15] L. Qisheng, W. Lai, S. Zhiyi, L.Yansheng, K. Morita, R. Matsuoka, and S. Ito, "Natural contamination test results of various insulators under DC voltage in an inland area in China," in *Proc. Int. Conf. Properties and Application of Dielectric Materials*, Tokyo, Japan, 1991, vol. 1, pp.350–353.

[1.16] K. Takasu, T. Shindo, and N. Arai, "Natural contamination test of insulators with DC voltage energization at inland areas," *IEEE Trans. Power Del.*, vol. 3, no. 4, pp. 1847–1853, Oct. 1988.

[1.17] Y. Suzuki, S. Ito, M. Akizuki, and T. Irie, "Artificial contamination test method on accumulated contamination conditions," in *Proc. Int. Symp. High Voltage Engineering*, London, U.K., 1999, vol. 4, pp. 192–195

[1.18] T.C. Cheng and C.T. Wu, "Performance of HVDC insulators under contaminated conditions," *IEEE Trans. Elect. Insul*., vol. 3, pp.270-286, 1980.

[1.19] K. Nakanishi, A. Yoshioka, "Surface charging on epoxy spacer at dc stress in compressed SF_6 gas", *IEEE Trans. Power Appar. Syst*., vol. PAS-102, no. 12, pp. 3919-3927, 1983.

[1.20] O. A. Lasabi, A.G. Swanson, and I.E. Davidson, "Surface charge accumulation on DC insulators: an overview," in *25th South African Universities Power Engineering*

of Conf., Stellenbosch, South Africa, 2017, vol.1, pp. 38-43.

[1.21] H. Fujinami, T. Takuma, M. Yashima and T. Kawamoto, "Mechanism and effect of DC charge accumulation on SF_6 gas insulated spacers," *IEEE Trans. Power Del*., vol. 4, no. 3, pp. 1765-1772, 1989.

CHAPTER 2 THEORETICAL BACKGROUND AND LITERATURE REVIEW

This chapter aims at providing the theoretical basis that governs the DC electric field distribution, surface flashover characteristics and surface charge accumulation process of HVDC insulators or spacers. A spacer is an insulator that is used inside a gas filled insulation environment to provide both mechanical support and electrical insulation to a conductor at high voltage.

This chapter consists of three sections. Section 2.1 introduces the overall physical background, the surface charging mechanisms, and the development of the relevant theories. Section 2.2 reviews the mathematical modelling work and the corresponding governing equations, boundary conditions, and typical results. Section 2.3 presents the typical experimental cases that were reported in the past 30 years together with the experimental setup and typical results. These experiments are important because they provide baseline data for the assessment and verification of the proposed model.

2.1 Surface Charging Mechanisms

2.1.1 General Features of the HVDC Voltage in Power System

Electrostatic field, or static electric field, refers to the electric field when there is no macroscopic charge motion in the system. When the potential distribution in a region depends on the local charge distribution, the field is called Poisson field. When the space charge density is zero in the region of interest, it is called the Laplace field. When the electrostatic field is determined by the dielectric permittivity of the involved materials, it is called capacitive field.

DC field refers to the situation where the field does not change its polarity. When the DC voltage stays constant, there is no dielectric loss due to polarization and the field is only determined by the conductivity of the dielectric material and is called resistive field.

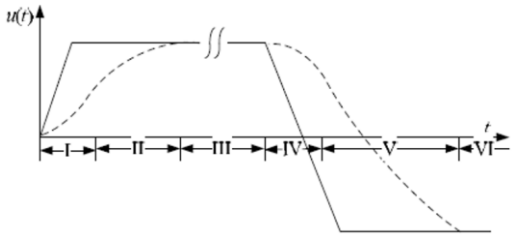

Figure 2-1 Example of capacitive and resistive electric fields under DC stress with polarity reversal [2.1].

As shown in Figure 2-1, the dotted line represents the growth and decay of surface charge of an insulator. Stage I: when the applied voltage on an insulator increases after the power source is switched on, the electric field is dominated by capacitive effect. Stage II: the applied voltage reaches its stable value and the transition from capacitive field to resistive field occurs. Stage III: a pure resistive field is presented. Stage IV: as a result of polarity reversal, a capacitive field is formed in the opposite direction of the previous field. Stage V: the surface charge changes its polarity and a new resistive field is formed.

In gas-insulated equipment, the weakest point in the system is often at the interface between the gas and the solid spacer which is used to support the conductors. Over a long operation time, considerable space charge accumulation occurs on the interface. The initiation of surface flashover is usually through the emission of electrons from the triple junction or localised ionization near the insulator surface where the electric field is much enhanced.

2.1.2 Dielectric Breakdown and Surface Flashover

In developing breakdown theories, the fundamental breakdown processes can be classified into three types, the electric breakdown, the thermal breakdown and the mechanical breakdown. The first breakdown theory of solid dielectric was the thermal breakdown in 1922 [2.1]. In this theory, the dielectric breakdown was attributed to the Joule heating due to the conduction current and its dissipation. When at low

temperature, the electric breakdown plays a more important role rather than the thermal breakdown. The investigation [2.1-2.3] suggested that when the temperature is low, dielectric breakdown of solid is due to the electronic process such as the current multiplication due to the collision ionization of high speed electrons. For instance, the interactions between electrons which are accelerated by the high applied electric field, the collision ionization of electrons with the space charge effect [2.4], the conduction charges and electrons trapped in the impurity and etc. In general, the dielectric breakdown is always accompanying by the destruction of the molecule structure. When it happens, the current multiplication occurs rapidly and greatly influence the whole process.

In operation, the critical breakdown voltage of SF_6 gas is affected by various factors, especially the local enhancement of the electric field. In the case of the uniform field, the critical breakdown voltage is directly proportional to the product of the pressure and the distance between the two electrodes, the anode electrode and cathode electrode, as illustrated in Figure 2-2(a). In the non-uniform field, however, the critical breakdown voltage highly depends on the configuration of the associated electrodes. For instance, Figure 2-2(b) illustrates the breakdown voltage of a common needle-to-plane gap [2.1]. The critical breakdown voltage increases nonlinearly with the increase of the gap between the needle and the plane. From Figure 2-2(b), it can be also found that the critical breakdown voltage of SF_6 gas is considerably larger than that of the air.

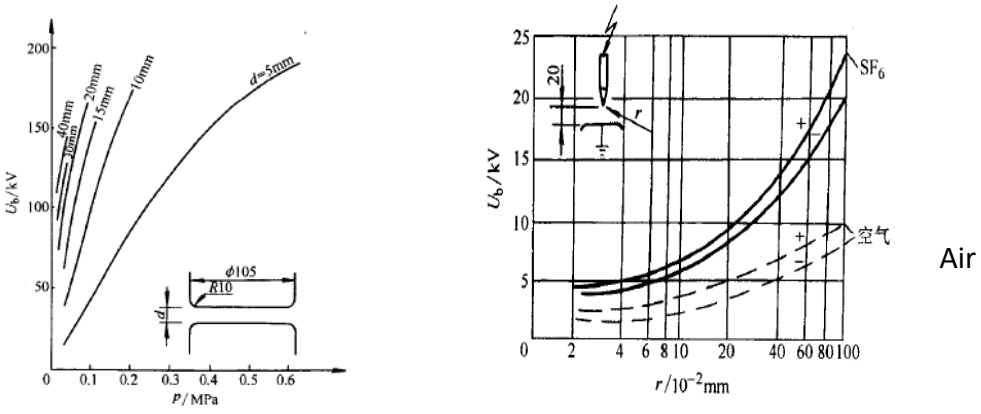

(a)uniform electric field *(b) non-uniform electric field*

Figure 2-2 Critical breakdown voltage of SF_6 [2.1].

In practice, the flashover voltage of supporting insulators is determined by a number of factors [2.5-2.12], such as the shape and structure of the spacer [2.5], contamination of surface increasing the local electric field or increasing surface conductivity [2.11], defects or protrusions on their surface [2.5-2.7], and the attachment of metallic particles on the surface [2.8]. There was also work showing that material impurity and electrode profile can be purely responsible for the accumulation of surface charge while the type of gas and insulation material yet plays a less important role in the charge accumulation process [2.6]. Therefore, at present the long-term insulation behaviour of insulators under HVDC stress is indeed an extremely complicated problem that is not well understood.

The reduction in dielectric strength of an insulator is often attributed to the effect of surface charges, or to ionization at high-field regions (such as the triple junction). The accumulation of surface charges on the insulator surface results in localized field enhancement leading to an increased failure probability during operation, especially during the polarity reversal process. Surface charge in sufficient quantities, in the range of 10^4 C/m^2, will lead to a significant reduction in the breakdown strength of the spacer [2.5]. Moreover, the charges can also result in a small conduction current that flows between the electrodes and spacer body and through the gas region (such as SF_6) [2.13]. A clear understanding of the process of surface charge accumulation and its effect is essential to the prediction, optimization and control of the performance of insulators.

2.1.3 Generation of Charged Particles in Gas

Charged particles can be generated in the insulation gas through many ways, for instance, the cosmic and earth radiation, the electron emission in the electrodes, the partial discharge in the protrusions, etc. In GIS equipment, the later are much more important. Preliminary investigations suggested that electron emission always takes place in the metallic cathode, due to thermionic or field emission, so as “charge injection”. The natural ionization current between two electrodes can saturate at a rather low electric field value, <1 V/mm [2.3,2.13-2.15]. When the electric field increases to a higher value (more than ~1 MV/mm), then the electron emission grows

exponentially with the increasing applied field. Moreover, it was suggested that [2.3] in the presence of contaminants, gas dielectric and imperfect electrode surfaces, emission phenomena could occur at much lower field stress. In a practical system, emission appears to occur at dielectric inclusions or on the conductor surface [2.3]. Halbritter [2.14] suggested that enhanced field emission is encountered at fields of the order of 0.01 MV/mm and further escalated by electrons and in dielectric (dust) particles in dielectric.

SF_6 gas is an excellent insulation gas and used in many gas filled high voltage insulation equipment. It is used in the present work as the insulation gas. Since SF_6 has strong electron affinity, in the region of a great deal of free electrons, stable SF_5^- is formed by attachment of an electron to an SF_6 molecule, forming heavy ions, or an ion pair (IP). This process is referred to as natural ionization and characterized by a production rate between 20 and 50 IP/(s·cm^3), depending on geographic location and gas pressure. To reflect the fact that volume ion production conserves charge neutrality, in the modelling work an equal natural production rate of positive and negative ions applies.

2.1.4 Surface Charge Accumulation

Early in 1978, Mangelsdorf and Cook [2.16-2.18] suggested the importance of surface charge accumulation. Their work indicated that the charging characteristics on the insulator surface were influenced in two ways, first came from the rapidly changed electric field by the source region, and second came from particles emission from the insulating surface layer. In their work, they measured the charge number density on a cast-epoxy axially symmetric post insulator with metal inserts at each end at high DC voltage up to 600 KV. It was found that the characteristic time to change from the initial capacitive field distribution to a resistive field distribution is of the order of 10 hours. Localized distortions in electric stress such as caused by conducting particles greatly change the accumulated charge. Charge carriers in the gas were found to be dense and of a polarity opposite to that of the middle part of the insulator surface. Moreover, due to inhomogeneity of the insulator body, charges can accumulate in the bulk material, which can be explained by,

$$\rho = -\frac{\varepsilon}{\sigma} \cdot E \cdot \nabla\sigma \tag{2.1}$$

where ε and σ are the permittivity and conductivity of the bulk material, respectively. Equation (2.1) shows that when there is variation of the electrical conductivity in the direction of the applied electric field inside an insulation material, space charge will be accumulated to influence the electric field to ensure current continuity in the direction of the applied field.

Over the period of 1980-1990, research was carried out by numerous research groups across the globe to study the charging mechanisms associated with HVDC insulators. In 1983, Nakanishi et.al [2.5,2.19] suggested in the experiment that charging is mainly controlled by partial discharge, gas conduction and field emission, and the flashover voltage along the spacer surface can be reduced by the existence of charges. In their experiments, they used dust figure techniques to locate the charge pattern. From experimental results, they found that surface charging can take place without any partial discharge, but there will be a large amount of charges accumulated on the insulator surface when partial discharge occurs in its vicinity. Opposite charges on the insulator surface were collected in the vicinity of the metal inserts at the end of the insulator since charge carriers in the gas are driven by the radial electric field towards the inserts. The radial field component (under static field) *En* is not symmetrically distributed along the surface, however, the charge distribution doesn't correspond to the distribution of *En*, has a rather symmetrical distribution.

Sato and Knecht [2.20] experimentally investigated the influence of surface charge and discussed its possible origin and accumulation mechanisms in 1987. The charges deposited and trapped at the spacer surface were experimentally shown to come from the gas driven by the force of the electric field. The surface charging process can be greatly influenced by the triple junction because the tangential field component along the surface is quite high at the upper triple junction and electrons can be released in the junction region.

In 1988, Boggs [2.21-2.23] showed that under DC stress charged particles are easily generated in the defect regions on the insulator surface. Along with the long-term operation, the particles can cause a small partial discharge. When it approached the

electrodes, it would have rapid partial discharge thus cause a very sudden (ns) change in the potential distribution. When the particles deposited onto a spacer surface, they are likely to be held on the spacer surface. Corona discharge formed at the particles tip may cause decomposition of SF_6 into highly corrosive species, which can attack the spacer surface and cause eventual failure. Epoxy spacers filled with SiO_2 are much more prone to degradation by SF_6 decomposition byproducts than those filled with alumina, especially when there are cavities in the insulator body. Cavities represent a key issue relating to the reliability of solid dielectric spacers in the GIS which can be generated during the casting process when air leaks into the mold due to control errors during the production. Within the existences of cavities, the breakdown voltage can be greatly affected.

In 1989 Fujinami et.al [2.15] used four cylindrical spacer samples to experimentally study surface charge accumulation in compressed SF_6. It was shown that accumulation of surface charge is much more rapid than the decay which has a characteristic time of 30 to 200 hours). The charge distribution has a close relationship with the normal component of the electrostatic field (on the gas side of the surface). Possible causes of surface charges were micro-discharge or field emission from the surface projections. In their work, they developed a spacer profile with no normal component on its surface, and the results showed that there is little or no surface charge accumulation on the surface.

At the beginning of 1990s, Farish [2.24,2.25] experimentally investigated the influence of charge deposition on the surface flashover in SF_6 under impulse voltages. He suggested that with large defects (>1mm in dimension) at the cathode triple junction the flashover onset level of the field was considerably reduced and charges can be deposited over most region of the spacer surface. When there is a large number of surface charges accumulated on the spacer surface, the field strength can be reduced by 50% of the gas only value, even at a pressure of 1 bar. The inserts of the electrodes can provide effective shielding of the triple junction. However, they introduced a normal field component which can easily attract charges to the surface.

Nitta [2.26] suggested in 1991 that the mechanisms of surface charge accumulation are likely to have three conduction paths, bulk conduction in solid insulation material,

surface conduction and gas conduction. For electrodes with a practical surface finished of industrial quality, the mechanism of gas conduction seems to be dominant, charge accumulation due to bulk conduction and surface conduction are maintained by a large amount of charge supplied by gas conduction. Charge carriers were attracted along the electric field in the gas from the conductor to the surface of the spacer until the field is sufficiently reduced by the accumulation of charges and continuity of current is realised.

2.2 A Review of Existing Modelling Work

The design of reliable HVDC insulation equipment requires trustworthy information concerning electric field distribution, flashover characterises and surface charge accumulation pattern. As discussed previously, the DC field calculation is more complicated than AC field. Calculation of the HVDC electric field dated back to the 1980s. Owing to lack of computing power and suitable software, it started with the analytic solution of simple governing equations to address very simple geometries. When it stepped into 2000s, computational modelling became common practice.

Apart from the mechanisms reviewed in Section 2.1, Cook et al. [2.16-2.18] proposed in 1982, a simple mathematical model for an epoxy insulator taking into account the influence of ion drift and diffusion. The voltage level used was up to 600 kV. The authors considered that the electric field can moderate the drift path of the charges towards the insulating surface, however, electric field is usually a minor factor in influencing the diffusion movement and thermal effect plays a key role in shaping the diffusive path. They used a ratio to represent the relevant importance of drift and diffusion effects. The numerical solution was obtained by manual calculation. They concluded that in the absence of large charge density gradient, the radial expansion of electric field was determined by the space charge effects. It was also shown that when the artificially generated charge source (corona discharge) was placed closer to the insulator, the surface charge density will be enhanced because of increased charge flux.

Sato and Knecht [2.7] modelled the surface charge accumulation in 1987 based on the assumption that space charge is mainly determined by an external field, not by current

conduction on the insulator surface. Their mathermatical model geometry as shown in Figure 2-3, was based on the current continuity equations, and both the upper and grounded electrode were not considered in the calculation. The Dirichlet boundary condition was applied at the electrode surface and Neumann bounday was applied at the solid insulator surface. They introduced an electric field analysis method named SSM (Surface-charge Simulated Method) allowed the space charge density to be obtained directly from 3D insulator systems. The SSM divided all surface of the system into small elements and allocated corresponding surface charge to them. Each charge density on each element of the dielectric boundary was calculated by Tchebycheff Polynomials of up to the fourth order.

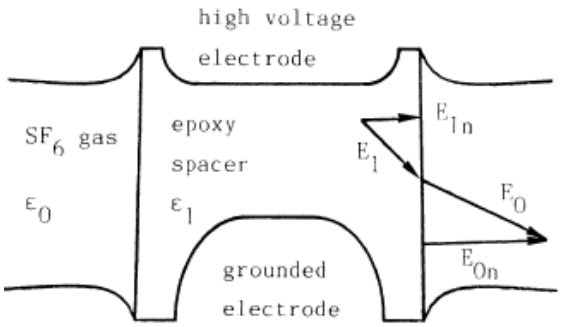

Figure 2-3 The axi-symmetric spacer model in [2.7]. The spacer and surrounding gas have permittivity of ε_1 and ε_0 respectively.

From their results, as shown in Figure 2-4, they predicated that electrons emitted by the source, such as from the tip of a protrusion on the electrode through field emission, move along the trajectory of the electric flux line and become trapped and attached on the dielectric surface due to the force by the dipole image charges. Their calculation showed that the typical accumulated charge density was approximately 10^{-4} C/m^2, and the tangential component of the electric field is dominant in the charge accumulation process.

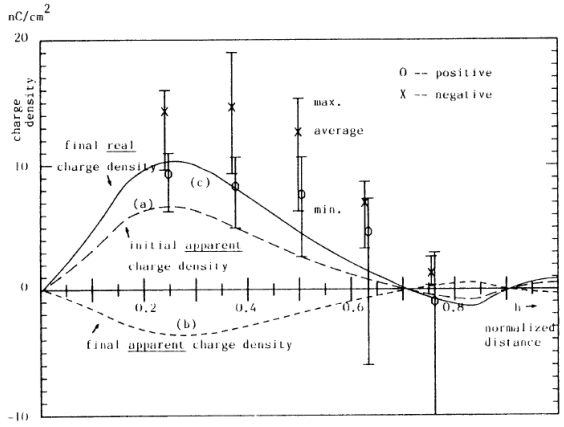

Figure 2-4 Charge density distributions along the dielectric boundary. The horizontal scale is the normalized distance along the boundary form bottom to top of the spacer. Curve (a) is for no space charge accumulation, Curve (b) is the final charging stage and Curve (c) is obtained by subtracting Curve (b) from Curve (a).

Another Japan research team leaded by Fujinami, used four cylindrical spacer samples as shown in Figure 2-5 (a), experimentally and computationally studied the surface charge accumulation in the compressed SF_6 in 1989 [2.15]. In their model, they proposed that the surface charge has an opposite polarity to the normal component of electric field, and it was decreased with the charging process. They estimated the maximum charge density based on the condition of *En* equalled to zero. From their results (Figure 2-5 (b)) can obtain that their estimated values were all bigger than the measured values, and this was probably due to a relatively short application time of the DC power.

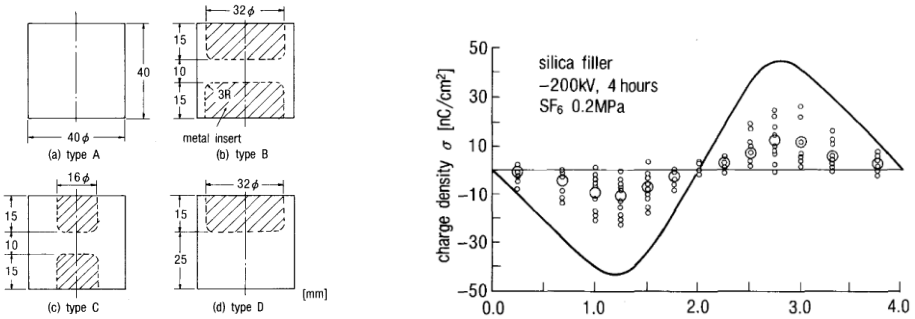

(a) *(b)*

Figure 2-5 (a) sectional view of model spacers, (b) is surface charge distribution of type B with 4 hours, and black curve is the estimated value from the model.

A few years later in 2001, Messerer and Boeck [2.27] calculated the electric field distribution around a standard 145 kV epoxy insulator that was used in an HVDC GIS, as shown in Figure 2-6. In their work, they focused much attention on the simulation of boundaries, because they considered that the electric field distribution on or near the electrode and insulator boundaries were of practical significance, and had close relationship with the boundary accumulated charges. Moreover, the charge distribution on these boundary elements was determined by the appropriate boundary conditions. So, based on this, they used an integral method that was used for numerical field calculation on boundary solution, named BEM (Boundary Element Method). And a complete user-friendly, interactive software named Xtwin [2.27] was employed to do the simulation.

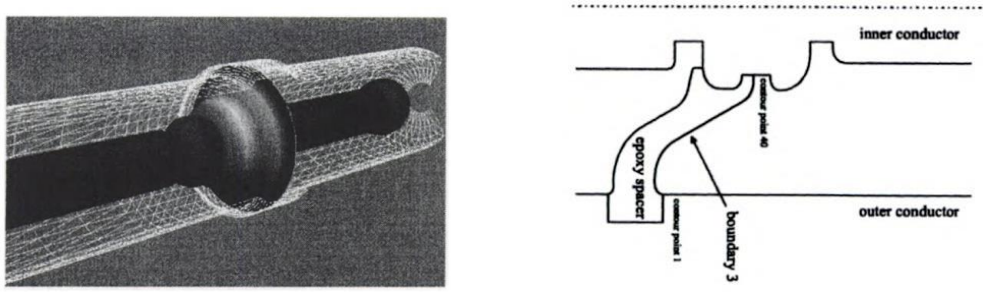

(a) *(b)*

Figure 2-6 (a) 3D modelling work, included the inner conductor, the spacer and the outer conductor of such a system. (b) 2D modelling of the spacer.

Their calculation indicated that the electric field was lower at the grounded side of the spacer and enhanced at the high voltage side. For an uncoated spacer, a high tangential field may lead to surface flashover. A uniform coating with a resistance of about 10^{11} Ω improved the electric field distribution, moreover, a non-uniform coating with a decreasing resistance due to increasing voltage can greatly enhance the field strength, which was not an optimum solution for HVDC GIS systems.

One of the principal questions in the charge transport and accumulation under DC stress is how do the conduction current and surface charge formation and transport in

the gas-solid interface. Volpov [2.28] in 2003, proposed a transient HVDC electric field model and time domain-calculating algorithm. In his modelling work, he formulated the boundary-value problem describing time-varying capacitive-resistive potential field in an interface layer as shown in Figure 2-7, and the surface conductivity was specified as a non-linear or arbitrary function, which took great steps forward in charge transport modelling.

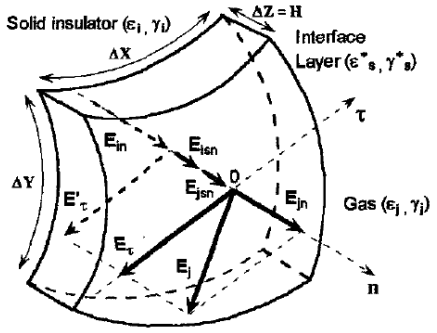

Figure 2-7 A unit element on the interface. Subscript i indicates parameters in the solid insulator. Subscript j indicates parameters in the gas region. Subscript n indicates the normal direction, and t the tangential direction.

The work in [2.28] was based on the assumption and simplification that there was a layer of non-zero thickness between the two bounding dielectrics, however, it is much thinner than the typical dimensions of the insulating system. The transverse drop in potential across the surface is taken to be equal to zero in terms of the negligible thickness of the layer. The field-matching conditions for insulating interfaces were adopted in the form of continuity equations for electric flux and electric current density. They accounted for the bulk and surface (layer with non-zero thickness) parameters of insulation. In this way, that surface reduction of the layer parameters allows avoiding the problems of calculation, which are related to the proximity of interface between sub-domains representing dielectric media.

For the solution, he employed Numerical Algorithm conjugates two calculating procedures, firstly, direct integration procedure over time applied to the continuity

equation, used a stepwise linear approximation of the integrand at the integration step. Secondly, calculating the electrostatic field at each of the above steps, involving an integral equation method (BEM). The electrostatic field approximation obtained is described by the standard Laplacel's boundary-value problem of equations. Effective simulations and simple modelling were obtained in his work.

In previous work, the solution for modelling work always depend on the iterative solution and numerical algorithm. In 2012, Winter and Kindersberger [2.29,2.30] implemented a gas model in the FEM-program COMSOL, shown in Figure 2-8. In their work, they solved the field equations numerically and pointed out the influence of the relevant physical parameters. In the drift-convection problem, there are always oscillations, especially for time-dependent calculation. In their work, they applied a discontinuities Galerkin-method (DGFEM) to support convergence of calculation.

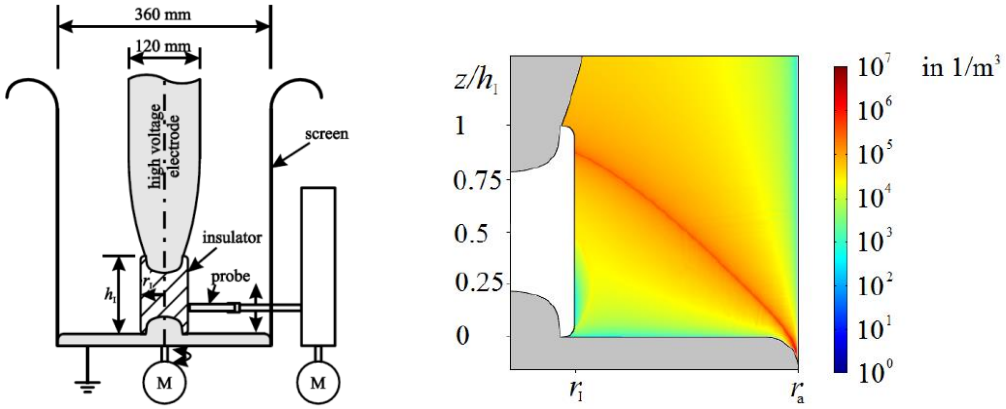

(a) *(b)*

Figure 2-8 (a) electrode arrangement with cylindrical insulator and probe for the measurement of the surface potential in [2.29,2.30]. (b) simulated negative charge density in the gas volume.

It is known that the electric field distribution in the insulator surface layer can be significantly influenced by the surface conductivity. According to the previous review on the surface conductivity influence, there exist many controversial conclusions. Latterly, Okabe experimentally and analytically investigated the insulation

characteristics for DC voltage where an area of non-uniform resistivity is present in the insulator surface layer [2.31]. Figure 2-9 (a) presented the model configuration in the work, the test model is cylindrical in shape, 40 mm in diameter and 50 mm high and placed between stainless-steel electrodes. The embedded electrodes are 21 mm high and the gap length between them is 8 mm.

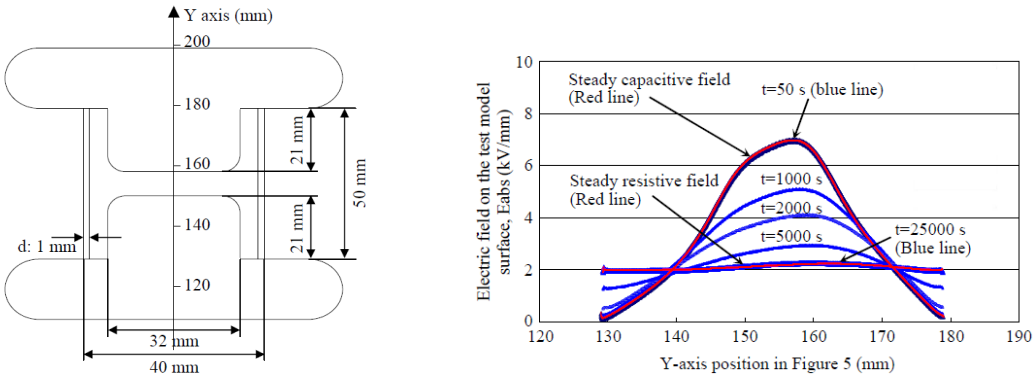

(a) *(b)*

Figure 2-9 (a)Electric field analysis model with uniform volume resistivity in the surface layer and (b) is the electric field distribution over time on the surface with uniform resistivity in the layer [2.31].

As can be seen in the Figure 2-9 (b), the electric field changed from the initial capacitive field to resistive field over time and decreased from 8 kV/mm to 2 kV/mm. This is considered because, with uniform resistivity on the surface layer, the leakage current mostly flowed through the bulk material instead of the surface layer. Furthermore, from the investigations, that can also obtain that with a non-uniform resistivity present in the insulating spacer surface layer, breakdown occurred several minutes to several hours after DC voltage application. However, without the non-uniform resistivity in the surface layer of the spacer, the electric field distribution was the same as that in the steady capacitive field analytical results immediately after the DC voltage application and almost equivalent to that in the steady resistive field analytical results after considerable time has elapsed. Moreover, based on the results of the breakdown test and electric field analysis of the test insulating spacer model, the

creepage breakdown electric field was estimated to be 40 kV/mm, or equivalent to 90% of the estimated breakdown electric field in the SF_6.

2.3 A Review of Experiment

The phenomena of charge transport and accumulation in practical high voltage equipment are affected by many factors that cannot all be correctly and completely considered in mathematical model. In fact, some of the factors in real situation can never be quantitatively characterised. Experiments under controlled conditions are therefore required to obtain reliable results that can help the advance of the modelling work. This review mainly focuses on the experimental investigation of rod type insulator.

In 1982, Knecht [2.32] tested the electrical behaviour of cylindrically shaped epoxy resin spacers between two parallel-plate electrodes with various shapes of the metallic insert. SF_6 and N_2 were used with a DC voltage up to 500 kV. The different test samples are shown in Figure 2-10.

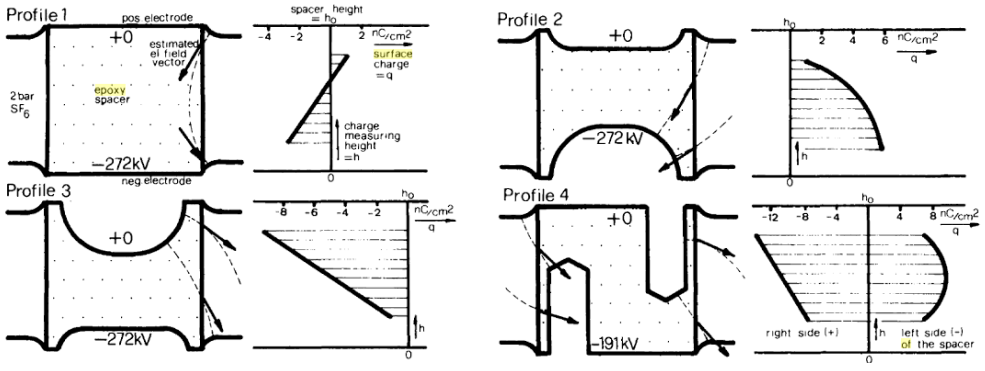

(a) *(b)*

Figure 2-10 measured charge distribution as a function of height for different electrode surface profiles. Four epoxy materials, the bisphenolic, cycloaliphatic, pure and with Al_2O_3-filler. Experiment was performed at a temperature of 20° C.

Despite the absence of some important details in [2.21], it can be obtained that the surface charge accumulated on epoxy resin spacers was mainly determined by the electric field distribution and material impurities from their experiments. Temperature increase in electrodes, such as grounded electrode up to 100° C and HV electrode up to 50° C didn't show a significant influence on the accumulated charges. The charge accumulation and relative reduction in breakdown strength depends on the electrode profile and voltage level. Higher DC conductivity of the bulk dielectric material or the surface material would lead to more homogeneous charges accumulation.

At the same time, Nakanishi et.al experimentally investigated the influence of surface charge on post and conical epoxy spacer under HVDC stress using the dust figure technique [2.19,2.33]. The insulation gas was SF_6 and the experimental arrangement is shown in Figure 2-11.

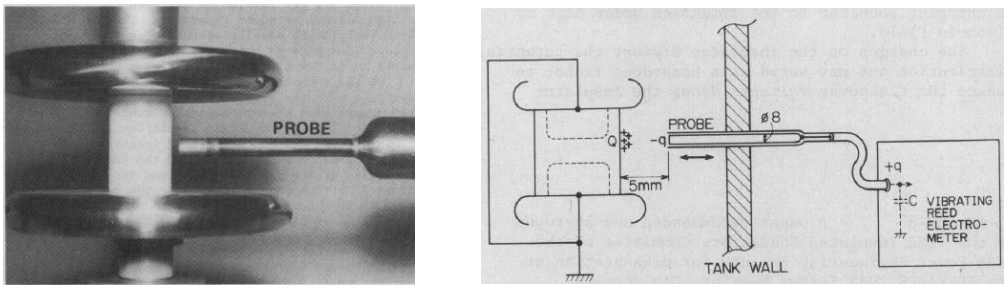

(a) *(b)*

Figure 2-11 (a) Electrostatic probe placed in the gas vessel. (b) Diagram showing the measuring system for surface charge.

In the sample configuration, the cylindrical insulator of cast epoxy resin has a metal insert at each end. Two types of spacer samples were used in the test, one was without any treatment on the surface layer and the other one was with horning treatment on the order of 10-20 μm (horned particle). The accumulated charges were measured by an electrostatic probe placed in the test vessel. The dust figure technique was utilized to observe the pattern of the accumulated charges at atmospheric pressure.

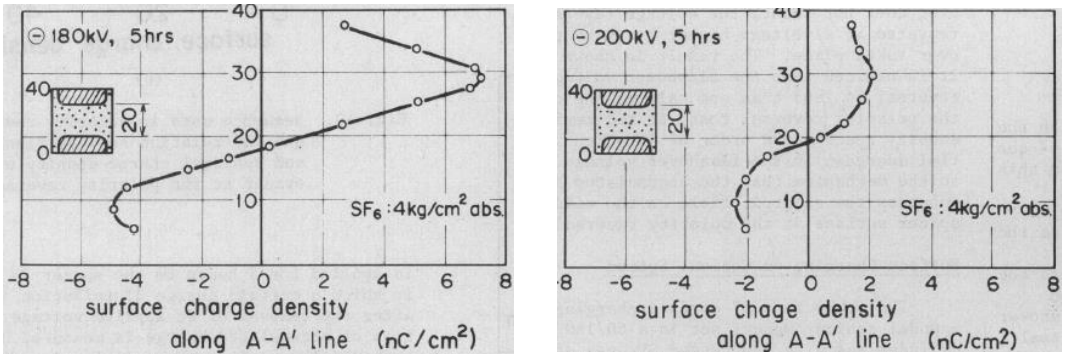

(a) *(b)*

Figure 2-12 (a) Surface charge density with untreated spacer, energized with a DC voltage of 180 kV for 5 hours. (b) Surface charge density on the horned spacer with a DC voltage of 200 kV for 5 hours.

Charges in the surface layer exhibit a near-symmetrical distribution in the longitudinal direction, as shown in Figure 2-12. Figure 2-12 (a) shows a typical hetero-charge distribution in which the charge of opposite polarity distribution in the vicinity of each electrode. The charge density on the horned spacer is much lower than that on the untreated spacer, and the hetero-charge is deposited uniformly around the circumference of the spacer surface. The local charge accumulation is considered to occur at locally highly conductive areas.

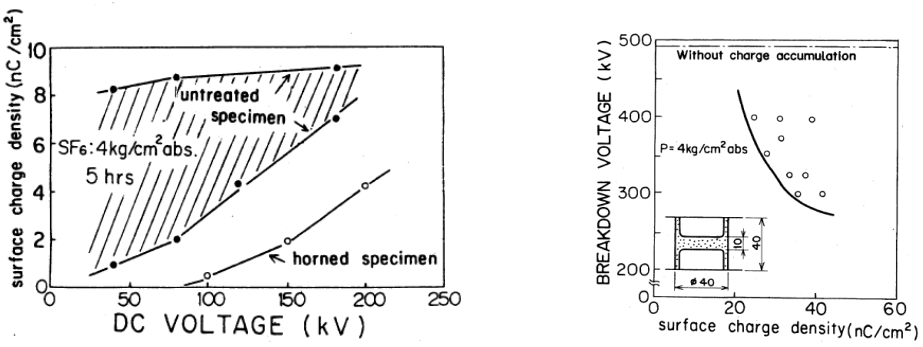

(a) *(b)*

Figure 2-13 (a) the relationship between the charge density and applied volatge for two groups of specimens : the untreated spacers and the horned spacers. (b) the relation between flashover volatge and residual charge density of model spacer at the polarity.

Figure 2-13 (a) presents the relation between the charge density and applied voltage for two groups of specimens. There seems to be a charge onset-voltage below which charge does not build up. The charge onset-voltage is about two times higher on the horned spacer than on the untreated spacer. The accumulated charge increases with the duration and magnitude of the applied DC voltage. The DC flashover voltage is found to be not decreased from the value although a large amount of hetero-charge is deposited. This is probably because the hetero-charge accumulation made the electric field along the surface more unifrom. Sato and Knecht [2.7] investigated the influence of surface charge and discussed the origin and accumulation mechansims by experiment in 1987. The arrangement is shown in Figure 2-14.

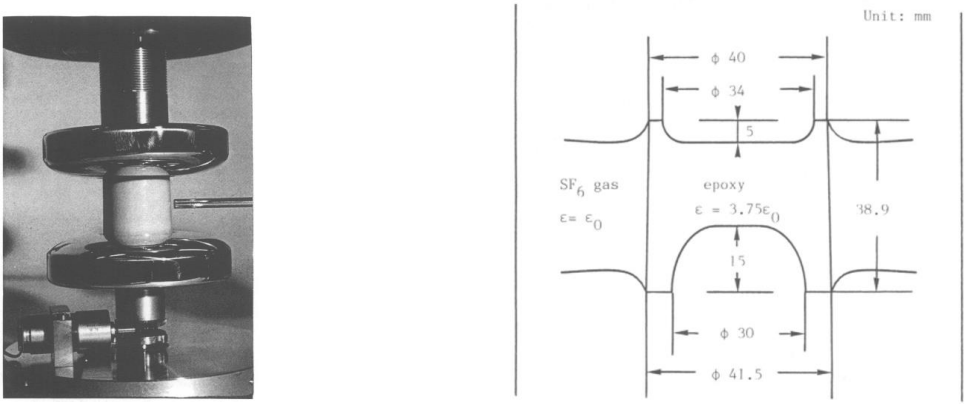

(a) *(b)*

Figure 2-14 (a) photograph of the epoxy spacer system and field mill probe in the testing chamber (b) schematic diagram of the spacer sample with the dimensions in mm.

In their experimental configurations, two electrode inserts were made to have different lengths to study the polarity effects. During the voltage application, the field probe was removed for protection purposes. The probe was grounded during the measurements when it was used to measure the perpendicular component of the electrical field with its pickup electrode at a distance of 1mm from the surface. The DC voltage applied was up to 310 kV.

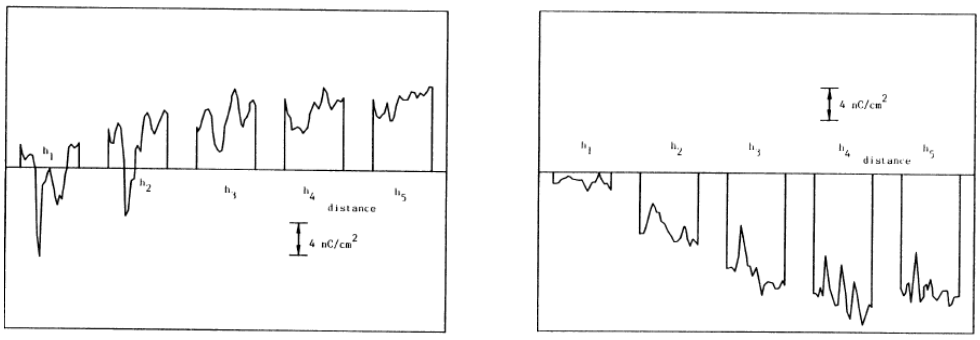

(a) Positive applied voltage *(b) Negative applied voltage*

Figure 2-15 Measured charge density distribution. Measurments are done at five different positions, (h1-h5), along the axial direction of the spacer. Circumferential distributions are figured out at each point. h1-h5 (h1=9.5mm, h2=14.5mm,h3=19.5mm, h4=24.5 mm and h5= 29.5mm are the distances from the grounded electrode.

The results of a measurment which is displayed in Figure 2-15 seem non-uniform in the circumferential direction, suggesting the occurrence of a microscopic surface discharge or the existence of electrical inhomogeneity of the spacer material. It was obtained in the experiments that for long-term voltage application, charges on the surface of the insulator (surface charges) were accumulated and stayed fixed for a very long time, if the gas pressure within the vessel remained constant and hence the intrinsic breakdown strength of the gas were not reduced significantly. The final charge density is predominantly determined by the initial external field distribution and not by the bulk or surface conductivity in regions where the tangential component of the field is dominant and the spacer accumulates less charge. A decay of charge density of less than 1% per hour was typical. During the measument, the surface charge deposited at the rear side would contribute to the reading, increases the measured values.The uncertainy, about 20% about the measured values in the experiment was analysed, such as the probe couldn't pinpoint the charge density at the exact position, the inaccurate calibration of the proble and etc. So the optimization and improvement can be relized in the further work.

After that, another Japanese research team lead by Fujinami used four cylindrical spacer samples to experimentally study the charging mechanism and effect of the DC charge accumulation on the surface of a solid spacer in compressed SF_6 in 1989 [2.15].

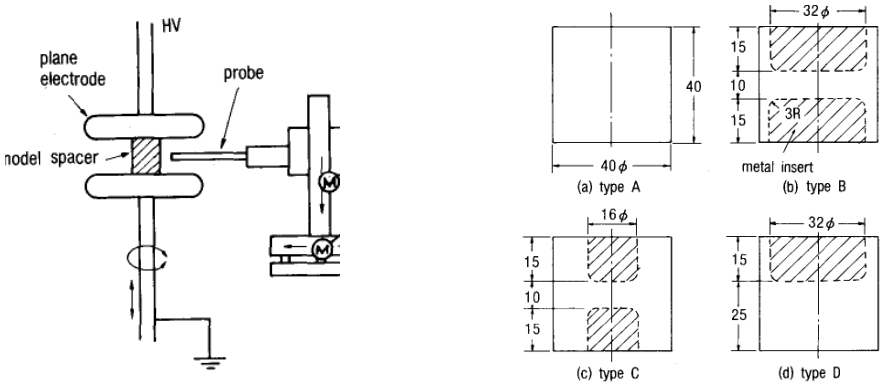

(a) *(b)*

Figure 2-16 (a) the experimental setup in the testing vessel. (b) sectional view of the model spacer samples. The applied voltage from DC 200 to 300 kV.

A spacer was set between parallel plane electrodes 20cm in diameter in a steel vessel, as shown in Figure 2-16 (a), the experimental arrangement with an electrostatic probe used for measuring surface charge density distributions during the test. Four types of spacers were used in the test, and made of epoxy resin containing alumina (Al_2O_3) or silica (SiO_2) as filler. The insulators have a short length of 4 cm and diameter of 4 cm, the length of inserted electrodes was different and the pressure of SF_6 is between 2-3 bar. The charge measurement was performed vertically along the Z-direction from Z=0 (grounded plane electrode) to Z= 4cm (upper electrode) at intervals of 30 degrees of the circumferential angle.

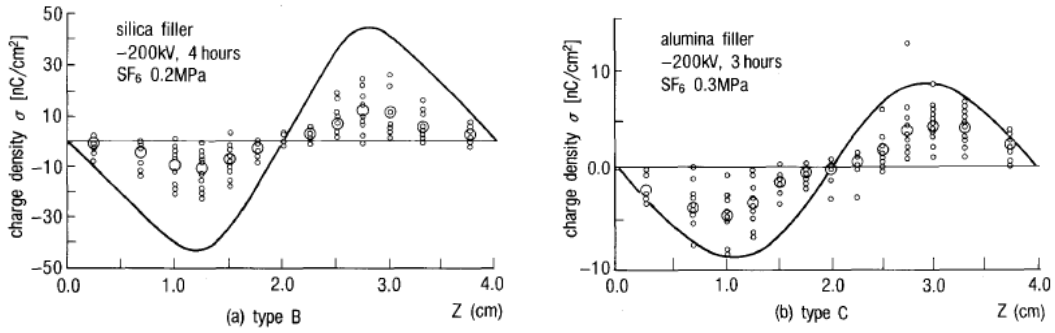

(a) *(b)*

Figure 2-17 Measured surface charge density. Small circles – measured surface charge density; large circles – average value in the azimuthal direction of measured charge density; solid curves – from simple model in the paper.

As can be seen from the results in Figure 2-17, the magnitude of the surface charge distributions are nearly symmetric to the middle point Z=2 cm, but with opposite polarity. When the metal inserts of the electrodes have larger radius, the charge density is much higher. In terms of these features, the possible charging mechanism can be concluded as follows, the surface charge distribution on a spacer has a close relationship with the normal component (gas side) E_n of the electric field on the surface and is also influenced by the surface roughness. Possible causes of the surface charge are micro-discharge or field emission from surface projection, motion of dust particles and natural ionization of SF_6 gas in a prolonged time range. Charge carriers drift through the gas along electric lines of forces up to the maximum charge density of the spacer surface given by the condition of E_n=0.

In 1991, Nitta firstly experimentally investigated the charge accumulation on post type spacer combined with cone type spacer in one experimental equipment with the influence of conducting particles in SF_6 gas-insulated HVDC switchgear, as shown in Figure 2-18 [2.26].

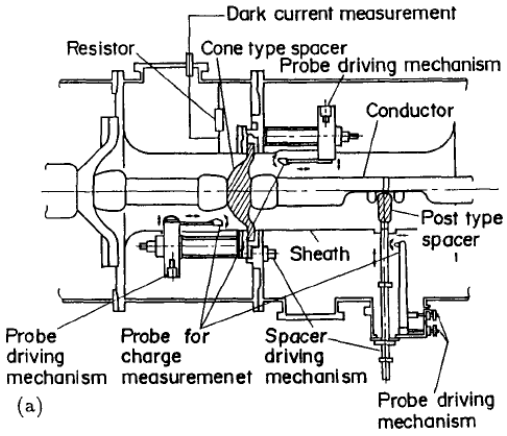

Figure 2-18 Cross sectional view of the test tank in which experiments on surface charging were performed in [2.26]. A model cone-type spacer and a post-type spacer are mounted between coaxial cylinders in the test tank. The system is filled with SF_6 at 0.4 Mpa. The sample spacers were energized with positive and negative DC voltages up to 900 kV.

During application of the voltage, the probe was placed in a recessed location as shown in Figure 2-18, so that the presence of the probe does not disturb the potential distribution in the system. The measurement was conducted by extending the probe to a position, say 20 mm away from the spacer surface, after the removal of the voltage. The results showed that saturation occurred in the first 30 minutes.

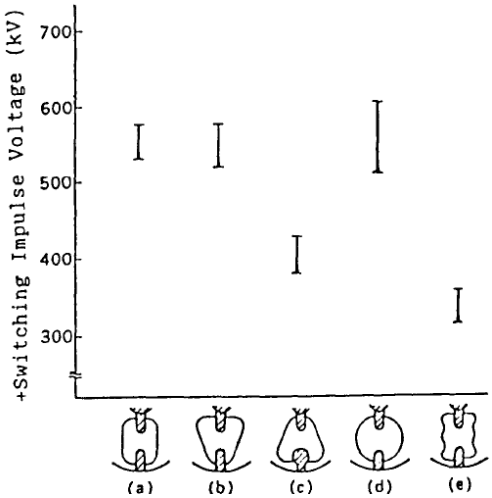

Figure 2-19 breakdown properties of positive switching impulses of five types of post spacers pre-stressed at -300 kV dc.

In their published results, most of the work was done on the conical type spacers, little results were found about the post type spacer. From the limited amount of results on the post spacers as shown in Figure 2-19, we can observe that the spacer shape can greatly influence the breakdown voltage, shapes like a, b and d can withstand higher voltage level, so the shape of a, b and d were preference in the insulator design. The measurement errors were caused by the following factors, distance between the spacer and the metallic substrates, thickness of the spacer, area of surface charging, distance between probe and spacer, surface charging on both sides of the spacer. Therefore, in order to get more accurate and reliable charge distribution on the spacer from the probe measurement, more efforts can be devoted in these aspects.

Special geometries of electrodes were designed to determine the dominant mechanism of surface charge accumulation in 1993 by Jing Tao et.al. In the experiment [2.6], the author designed several different electrode and spacer arrangements in order to generate different electric field distribution to studying their influence on the surface charge distribution, as shown in Figure 2-20.

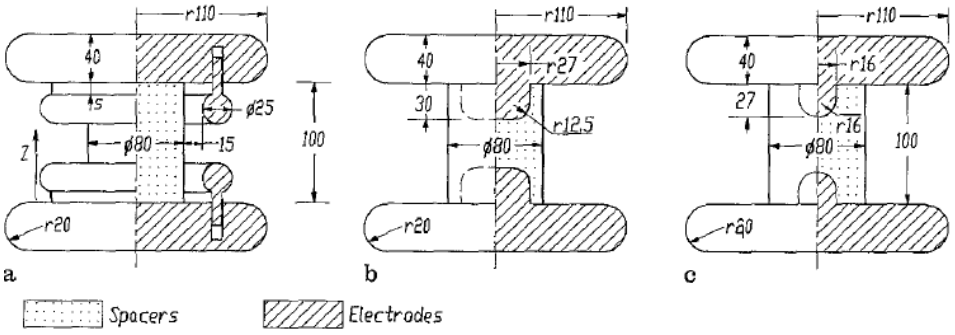

Figure 2-20: Geometric designs of the electrode arrangements used in the experiment, a with toroids, b with inserts r=27 mm and c with inserts r=16mm. Cylindrical epoxy spacers were used which are 100 mm high and 80 mm in diameter. The epoxy is filled with silica possessing 90% silicon dioxide and has a permittivity of 4.2.

In this experiment, the key step and different point from others work is the electric field design. This was studied by terms of the field components at the surface. In their

plan, they wanted to design an electric field that, the normal component of the field along two spacers under test are equal in amplitude and opposite in direction, whereas the tangential components are similar. The tangential components of field along two spacers are identical, but the normal components are opposite in direction. Those field distributions were achieved by a pair of disc electrodes in combination with toroid or inserts. The separation of the toroid from the disc electrodes was varied in order to change the profile of the field.

The tests were performed in a tank of one-meter diameter, filled with 1 bar SF_6. The disc electrodes and the toroid are made of brass with a surface roughness of 0.5 μm. After a spacer had been stressed for a certain period, the voltage was removed and an in-situ surface charge measurement was performed using a capacitive probe which was calibrated on the account of all the capacitive parameters. In their results, they indicated that, charge transport in the gas space is the dominant mechanism for charge accumulation, the normal component of the field played an important role. Bulk conduction in the spacer body is not responsible for charge accumulation and surface conduction has little effect on the charge accumulation, the emission behaviour at the electrodes is the most important factor that affects charge distribution and accumulation.

Hasegawa and Fujiwara investigated the surface charge density distribution with different surface treatment conditions of spacers, including low permittivity material coating, an anti-charging material coating, a metal-sputtering coating and non-coating. The tested sample and conditions can be seen in Figure 2-21. The pre-stressed DC breakdown voltage and lightning impulse breakdown voltage of an epoxy insulator were measured to understand the charging process and accumulation mechanisms [2.34, 2.35].

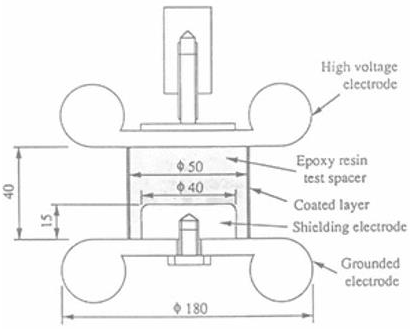

Table 1. Test conditions and results

Set No.	Spacer coating material	Electrode coating material	Surface resistivity (Ω)	Thickness of coating (μm)	DC Breakdown voltage (BDV)
1	Without	Without	10^{16} - 10^{17}	–	-200kV, withstood
2	Epoxy resin (low permittivity)	Without	10^{14} - 10^{15}	300 - 800	-200kV, withstood
3	Anti - charging material	Without	10^{11} - 10^{12}	20 - 50	-150 - 180kV
4	Metal sputtering coating	Without	10^{11} - 10^{13}	0.03 - 0.08	-200kV, withstood
5	Without	Epoxy resin		80 - 150	-200kV, withstood

(a) *(b)*

Figure 2-21 (a) The testing sample. (b) surface treatment conditions used on the spacer.

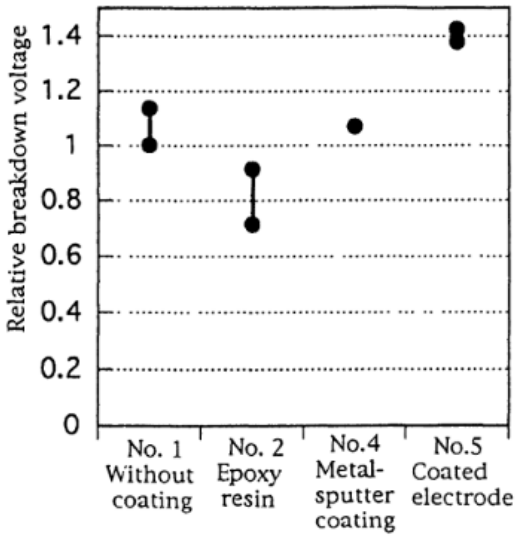

Figure 2-22 Relative breakdown voltage of four cases withstood the DC 200 kV.

From Figure 2-22, we can obtain that the coated electrode (No.5) had the highest breakdown voltage. They considered that this was probably because of the following reasons, there was no effect from accumulated charge under this circumstance, because there was no triple junction and no boarder surface between the epoxy resin spacer and coated layer. Moreover, field emission from the high voltage electrode was avoided under this situation. For No.1 and No.5, as can be seen in Figure 2-23, few charges (shaded regions) were observed, some spot charges (several nC /cm^2) remained for No.1. This was one of the reason that No.1 breakdown voltage was lower than that of

No.5. There were many negative polarity charges accumulated at the surface near the top of the inside shielding electrode. It was assumed that these charges were supplied through the coated layer. Therefore, it was important that the resistance of coated layer wasn't reduced (thickness was as thin as possible) and the surface resistivity of the coated layer was reduced.

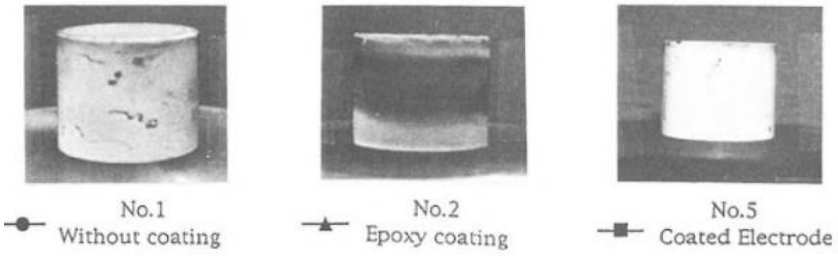

Figure 2-23 Examples of accumulated charge distribution with different coating materials. The shaded area was the accumulated charge region.

From their measurements, a thick coating layer of low resistivity material on the spacer surface was not recommended considering that the breakdown voltage can be decreased. An uncoated spacer with coated electrodes has the best insulating performance regarding breakdown characteristics during polarity reversal.

In 2012, Winter and Kindersberger [2.29, 2.30] experimentally investigated the electrical field distribution under the influence of surface charge along epoxy resin insulator surface in air. It has to be noted that in their experiment, they focused much attention on the investigations of the electrostatic probe measuring system, as shown in Figure 2-24, because they considered that the calibration of the probe can greatly affect the accuracy of the results. Therefore, the influence of the probe is simulated by implementing the probe's geometry in a 3D model of the electrode arrangement.

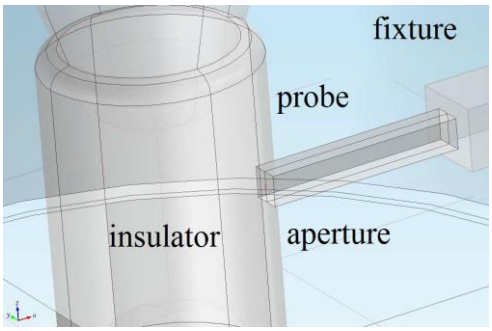

Figure 2-24 Transparent illustration of the 3D model of the electrode arrangement insulator and probe's fixture and the aperture on the tip of the probe.

2.4 Summary

The theoretical basis relating to HVDC insulation and charge accumulation was introduced in this chapter. In particular the transition from capacitive field to resistive field is explained, which is important in the analysis of the energisation stage or the polarity reversal stage of an HVDC transmission system.

A review of the modelling work was then carried out, which helps in-depth understanding of the relevant physical processes and its mathematical representation. It is shown that to explain the charge transport process, coupling of different processes is required, which could not be done in the 1980 because solution to the individual governing equations was based on an iterative method and computer code was not readily available. It was the availability of high performance computer in the 1990s that made accurate solution to the coupled governing equations possible.

The development and verification of charge transport model requires reliable and repeatable experimental results, which have not been available in abundance. Therefore, there is a need to identify experimental cases that can be used for the verification of my model. Subsequently, a review on relevant experimental work was conducted and several cases with clearly defined experimental conditions, carried out in different gases and at different voltage levels, were discussed in this chapter. The review also indicated that the non-uniform distribution of surface charges in the azimuthal direction on the surface in practical conditions. The variation can be large, typically 50% of the maximum value. The experimental results also show the variation

in experiments can be large, depending on the experimental conditions, the surface charge number density can be 5×10^{-5} C/m^2 at 200 kV [2.15] and 1×10^{-5} C/m^2 at 15 kV in [2.30].

2.5 Reference

[2.1] K. W. Wagner, "The physical nature of the electrical breakdown of solid dielectrics," *Journal of the American Institute of Electrical Engineers*, vol.41, No.12, pp. 1034-1044, 1922.

[2.2] C. Zener, "A theory of the electrical breakdown of solid dielectrics," *Proceedings of the Royal Society of London*, vol. 855, pp. 523-529, 1934.

[2.3] R.V. Latham, "The origin of pre-breakdown electronic emission from vacuum-insulated high voltage electrodes," *Vacuum*, vol.32, pp. 137-140, 1982.

[2.4] Y. Inuishi, K. Onishi, Y. Tada and T. Suita, "Secondary factors in dielectric breakdown of solids," *J. Inst. Elect. Engrs. of Japan*, vol.76, pp. 913-918, 1956.

[2.5] K. Nakanishi, A. Yoshioka, Y. Arahata and Y. Shibuya, "Surface charging on epoxy spacer at DC stress in compressed SF_6 gas," *IEEE Trans. Power App. Syst*., vol. PAS-102, No. 12, pp. 3919-3927, 1983.

[2.6] T. Jing, P. H. F. Morshuis and F. H. Kreuger, "Mechanisms of surface charge accumulation in SF_6," *Archiv fur Elektrotechnik*, vol. 77, No. 2, pp. 151-155, 1994.

[2.7] S. Sato, W. S. Zaengl and A. Knecht, "A numerical analysis of accumulated surface charge on DC epoxy resin spacer," *IEEE Trans. Electr. Insul*., vol. EI-22, No. 3, pp. 333-340, 1987.

[2.8] T. Hasegawa, T. Fujiwara, H. Ooi, S. Yanabu, H. Aoyagi and Y. Kanno, "The influence of charging of GIS epoxy insulator on DC/Impulse superposed breakdown characteristics," *Gaseous Dielectrics VII*, pp. 511-518, 1994.

[2.9] A. Winter and J. Kindersberger, "Transient field distribution in gas-solid insulation systems under DC voltages," *IEEE Trans. Dielectr. Electr. Insul*., vol. 21, No.1, pp. 116-128, 2014.

[2.10] F. Wang, Y. Qiu, W. Pfeiffer and E. Kuffel, "Insulator surface charge accumulation under impulse voltage," *IEEE Trans. Dielectr. Electr. Insul*., vol. 11 No. 5, pp. 847-54, 2004.

[2.11] R. Sundararajan, "Effect of insulator profiles on dc flashover voltage under polluted conditions, a study using a dynamic arc model," *IEEE Trans. Dielectr. Electr. Insul.*, vol.1, pp. 124-32, February 1994.

[2.12] B. Lutz and J. Kindersberger, "Surface charge accumulation on cylindrical polymeric model insulators in air: simulation and measurement," *IEEE Trans. Dielectr. Electr. Insul.*, vol. 18, No. 6, pp. 2040-2048, 2011.

[2.13] N. Fujimoto, "Conduction currents in gas-insulated switchgear for low level DC stress," in *Gaseous Dielectrics V*, L. G. Christophorou, Don W. Bouldin. Tennessee, U.S.A: Pergamon Press, 1987, pp. 129-153.

[2.14] J. Halbritter, "Enhanced electron emission and its reduction by electron and ion impact," *IEEE Trans. Dielectr. Electr. Insul.*, vol.3, pp. 253-261,1983.

[2.15] H. Fujinami, T. Takuma, M. Yashima and T. Kawamoto, "Mechanism and effect of DC charge accumulation on SF_6 gas insulated spacers", *IEEE Trans. Power Del.*, Vol. 4, No. 3, pp. 1765-72, 1989.

[2.16] C. W. Mangelsdorf and C. M. Cooke, "Static charge accumulated by epoxy post insulation stressed at high DC voltages," in *Electrical Insulation & Dielectric Phenomena Conf.*, Pocono Manor, USA, 1978, pp. 220-226.

[2.17] C. W. Mangelsdorf and C. M. Cooke, "Bulk charging of epoxy insulation under DC stress," in *Electrical Insulation Conf.,* Boston, USA, 1980, pp. 146-149.

[2.18] C.M. Cooke, "Charging of insulator surfaces by ionization and transport in gases", *IEEE Trans. Electr. Insul.,* vol. EI-17, pp. 172-178, 1982.

[2.19] K. Nakanishi, H. Ootera; Y. Shibuya; Y. ArahataT. Nitta, "Charge accumulation on conical spacer in compressed SF_6 gas at DC stress," in *Electrical Insulation & Dielectric Phenomena of Conf*., Buck Hill Falls, USA, 1983, pp. 87-94.

[2.20] S. Sato, W. Zaengl and A. Knecht, "A numerical analysis of accumulated

surface charge on DC epoxy resin spacers," *IEEE Trans. Dielectr. Electr. Insul.,* vol.3, pp.333-340,1987.

[2.21] S.A Boggs, "Sulphur hexafluoride- A complex dielectric," *IEEE Electr. Insul. Mag.,* vol. 5, pp. 16-21,1989.

[2.22] S.A. Boggs, "Partial discharge. III. Cavity-induced PD in solid dielectrics," *IEEE Electr. Insul. Mag.,* vol. 6, pp. 11-16,1990.

[2.23] S.A. Boggs, "Partial discharge: overview and signal generation, *IEEE Electr. Insul. Mag.,* vol. 6, pp. 33-39,1990.

[2.24] I. D. Chalmers, C. X. Wang, and O. Farish, "Dielectric surface charge phenomena in a space environment," In *Pulsed Power Conf.,* Monterey, USA, 1989, pp. 804-808.

[2.25] O. Farish, "Charge deposition and insulator flashover in SF_6 under impulse voltages," In *IEE Colloquium on Charging and Tracking of Insulators in Gaseous and Vacuum Environments Conf.,* London, UK, 1990, pp. 1-5.

[2.26] T. Nitta and K. Nakanishi, "Charge accumulation on insulating spacers for HVDC GIS," *IEEE Trans. Dielectr. Electr. Insul.,* vol. 26, pp.418-427, 1991.

[2.27] F. Messerer, W. Boeck, H. Steinbigler, "Enhanced field calculation for HVDC GIS," in *Gaseous Dielectrics IX*, London, UK: Springer US, 2001, pp. 473-483.

[2.28] E. Volpov, "Electric field modelling and field formation mechanism in HVDC SF_6 gas insulated systems," *IEEE Trans. Dielectr. Electr. Insul.,* vol. 10, pp. 204-215. April 2003.

[2.29] A. Winter and J. Kindersberger, "Transient field distribution in gas-solid insulation systems under DC voltages," *IEEE Trans. Dielectr. Electr. Insul.,* vol. 21, pp. 116-128, 2014.

[2.30] A. Winter and J. Kindersberger, "Stationary resistive field distribution along epoxy resin insulators in air under DC voltage," *IEEE Trans. Dielectr. Electr. Insul.,* vol. 19, pp.1732-1739, 2012.

[2.31] O. Shigemitsu, U. Genyo, “Insulation characteristics of GIS epoxy insulators with non-uniform surface resistance under DC Voltage,” *IEEE Trans. Dielectr. Electr. Insul.,* vol.22, pp. 516-525, 2015.

[2.32] A. Knecht, “Development of surface charges on epoxy resin spacers stressed with direct applied voltages,” in *Gaseous Dielectrics III*, London, UK: Springer US, 1982, pp. 473-483.

[2.33] K. Nakanishi, A. Yoshioka, Y. Arahata and Y. Shibuya, “Surface charging on epoxy spacer at DC stress in compressed SF_6 gas,” *IEEE Trans. Power App. Syst.,* vol. PAS-102, No. 12, 1983.

[2.34] T. Hasegawa, T. Fujiwara, H. Ooi, F. Endo, T. Rokunohe and T. Yamagiwa, “Charging and breakdown characteristics of various surface treatment spacers under DC voltage in SF_6,” In *Gaseous Dielectrics VII.,* Loucas G. Christophorou and D.R. James, New York, *US:* Springer, 1994, pp.503-509.

[2.35] T. Hasegawa, K. Yamaji, M. Hatano, H. Aoyagi, Y. Taniguchi and A. Kobayashi, “DC dielectric characteristics and conception of insulation design for DC GIS,” *IEEE Trans. Power Del.,* vol. 11, pp.1776-1782, 1996.

CHAPTER 3 A MATHEMATIC MODEL FOR CHARGE TRANSPORT AND ACCUMULATION INSIDE AND AROUND A SPACER UNDER HVDC STRESS

As discussed in Chapter 2, one of the biggest challenges in enclosed HVDC insulation systems such as wall bushing is the insulation performance of spacers under long-term DC stress. This is a consequence of the action of constant electric field direction and charge flow. Different from that in AC applications, under a steady state there is no displacement current in the insulation materials. Although the current density is extremely low as a result of the high volumetric resistivity of the insulation materials, the electric field inside and around the solid insulator is controlled by the flow of charged particles (conduction current) in the insulation media (solid and gas) and by charges accumulated at the interface where there exists a clear discontinuity of electrical conductivity.

Electric permittivity, which is a reflection of the polarization of polar molecules, can play an important role in shaping the electric field when the applied DC voltage varies, such as in the Stage 1 depicted in Figure 2-1. But the significance of this influence depends on the relative largeness of the permittivity with respect to the electrical conductivity. Although charge transport models exist in literatures, such as those reviewed in Chapter 2, there is insufficient experimental verification of the models, especially for commercial scale insulators. In addition, the boundary conditions and interface conditions are not clearly and comprehensively discussed and described, limiting their applicability. In this chapter, a charge transport model complete with discussion of the charge transport mechanisms, interface conditions, boundary conditions and material properties has been given. This model will be implemented in Chapter 4 and used in Chapter 5 for the modelling and prediction the field distribution of an HVDC bushing spacer.

3.1 Existing Limitations and Problems

The insulation optimization of spacer under HVDC is more challenging compared with under HVAC in the gas filled system, due to following factors,

- The electrical field distribution under AC voltage depending on the permittivity of the involved dielectrics, which so called capacitive field distribution. However, under DC voltage, due to it is governed by the conduction process, moreover, during polarity reversal, the electrical field distribution would pass through several stages, this make the problem much more complicated.
- There is limited data on number density of surface charge measurement, the general way is to measurement the surface electric potential, then calculate it into the charge density. However, under practical conditions, the current pass through the insulator body is tiny, and the voltage application time is quite long, and the humidity in the surrounding can influence the charge decay time greatly etc. All the factors can largely influence the accuracy of the experiment, sometime, can lead to contradictive results. Moreover, most of experiments were carried out with the short-term time scale and lab-scale equipment. The situation in lab-scale can greatly different from that in practical scale. So, reliable design optimization should be based on the practical scale equipment.
- In the mathematical modelling aspect, there are limited reliable measurements data on the parameters and coefficients which are important in the simulation, for instance, charge pair generation rate, number density, the origins, the recombination and loss terms, the drift and diffusion coefficient. The simulated physical process can be greatly influenced by these parameters. Moreover, the boundary conditions and interface conditions play a decisive role in the simulation. How to implement a reasonable and appropriate boundary condition are the key steps in the computation.

3.2 Current Conduction in Solid

Strictly speaking, an ideal dielectric (insulator) is a material with no free electrons in

its lattice structure. All the electrons associated with an ideal dielectric are strongly bound to its constituent molecules. These electrons experience very strong internal restraining forces that oppose their random movements. Therefore, when an electric field is maintained within a dielectric by an external source of energy, there is no current. So, an ideal dielectric is a material in which positive and negative charge are so sternly bound that they are inseparable. It has zero conductivity. However, no real substance is an ideal dielectric. When the material subjected to electric fields of less than a certain intensity, these materials permit only negligible current to flow. For all practical purposes, these materials can be regarded as ideal (perfect) dielectrics.

When the dielectric interacts with external forces, such as electric fields, magnetic fields, mechanical stress or temperature changing, resulting in the occurrence of the dielectric phenomena. For instance, under the influence of an electric force, the molecules of a dielectric material experience distortion in the sense that the center of a positive charge of a molecule no longer coincides with the center of a negative charge, electric charges don't flow through the material as they do in the conductor, but slightly shift from their average equilibrium positions causing dielectric polarization. And polarization of a dielectric material results in bound charge distributions. These bound charge distributions are not like free charges, they are created by separating the charge pairs as mentioned before. If a dielectric region contains the free charge density in addition to the bound charge density, the contribution due to the free charge density must be considered to determine the electric field E in the dielectric region. That is

$$\boldsymbol{\nabla} \cdot (\varepsilon_0 \varepsilon_\infty \boldsymbol{E} + \boldsymbol{P}) = \rho_v \tag{3.1}$$

Under steady state conditions with a constant applied voltage, electrical current is caused by the flow of charges. Polarization does not contribute to the conservation of charged particles, i.e. it does not affect current continuity because the charges are bound. However, it does contribute to the space charge distribution, therefore influence the electric field distribution inside a dielectric medium. The electrical conductivity determines the ability of a material to conduct current while the electrical permittivity contributes to the strength of the electrostatic field. It is well known that the permittivity of a strongly polarizable material is large, which leads to a weak electric field inside. Therefore, the space charge density in a solid material is determined by

both the electrical conductivity and the permittivity:

$$\rho = \varepsilon_0(\nabla\varepsilon_r - \frac{\varepsilon_r}{\sigma}\nabla\sigma)\cdot \boldsymbol{E} \tag{3.2}$$

where ρ is the space charge density, ε_r the relative permittivity of the material, ε_0 the permittivity of free space, σ the volumetric electrical conductivity and $\boldsymbol{E} = -\nabla\varphi$ defines the relationship between the electric field vector and the electrostatic potential. It is obvious that a positive gradient of the relative permittivity in the direction of the electric field results in positive bound space charges due to the formation of aligned polarization. On the other hand, a positive electrical conductivity gradient in the direction of the electric field requires the presence of negative space charge to ensure the continuity of the conduction current.

The current density in solid insulation material such as epoxy or epoxy composition under the action of an applied electric field consists of two components, the first component is the conduction current, which is $\boldsymbol{J}_{con}$. The second component is the displacement current depending on time space that is $\boldsymbol{J}_{dis}$. The total current passing the insulator body is

$$\boldsymbol{J}_{total} = \boldsymbol{J}_{con} + \boldsymbol{J}_{dis} \tag{3.3}$$

Where the displacement current is

$$\boldsymbol{J}_{dis} = \frac{\partial \boldsymbol{D}}{\partial t} \tag{3.4}$$

the first term which represents the fast-capacitive displacement current. The second term $\boldsymbol{P}== \varepsilon_0\varepsilon_\infty\boldsymbol{E} + \boldsymbol{P}$ accounts for all "slow" polarization process, such as dipole reorientations, interface polarization or inter-phase polarization. The dipole moment $\boldsymbol{P}$ in a dielectric medium can be induced by an external electric field $\boldsymbol{E}$. The material is said to be linear if the dipole moment and, thereby, the polarization vector are proportional to $\boldsymbol{E}$**.** If the electrical properties of the dielectric are independent of the direction, that means the medium is isotropic. A dielectric material is said to be homogeneous if all portions of the material are identical.

From the conduction theory, conduction current is

$$\boldsymbol{J}_{con} = Ne\mu\boldsymbol{E} \tag{3.5}$$

Where N is the density of the charge carrier, e is its electric charge, μ is the mobility of the charge carrier.

The definition of the conduction current is complicated since the number of charge carriers depend on the electric field, temperature and external effects such as chemical species introduced in the insulator during manufacturing time. And the mobility can be influenced by many factors, the gas pressure, the temperature, the surrounding humidity and etc. But it can use a simple equation to describe as,

$$\boldsymbol{J}_{con} = \sigma_s \boldsymbol{E} \tag{3.6}$$

This is a useful pragmatic representation which helps to easily understand conduction process. However, the conductivity can be influenced by many factors, so it needs to take more attention when choosing the conductivity of the insulator material in the simulation. Different formulations for the functionality of the conductivity can be found in the literature review.

Based on the current continuity definition, that any change of charge in a region must be accompanied by a flow of charge across the surface bounding the region, the charge can be neither created nor destroyed, but merely transported. So, current continuity takes the form of

$$\nabla \cdot \boldsymbol{J} + \frac{\partial \rho_v}{\partial t} = 0 \tag{3.7}$$

Under steady state (DC), there can be no points of changing charge density. So, in this case, the equation can be reduced to

$$\nabla \cdot \boldsymbol{J} = 0 \tag{3.8}$$

$$\nabla \cdot (\sigma_{VS} \nabla \varphi_s) = 0 \tag{3.9}$$

where $\boldsymbol{E} = -\nabla \varphi_s$ defines the relationship between the electric field and the electric potential.

3.3 Charge Transport and Current Density in Gas

The knowledge of charge transport in gases is primordial and indispensable for the

understanding of the operational characteristics of different gas dielectrics insulation behaviors and for any attempt to improve their electrical and chemical performances. To study the charge transport and motion in the gas medium, let's take a control volume to demonstrate the gas transport. The net transport of any scalar, specific quantity ϕ is the balance of the influx of ϕ across the boundaries into the domain, outflux of ϕ across the boundaries from the domain, the accumulation of ϕ in the domain, the generation of ϕ within the boundaries of the domain, and the loss of ϕ within the boundaries of the domain, which are illustrated in Figure 3-1. So, the general conservation equation is,

$$\Phi_{net} = \Phi_{in} - \Phi_{out} + \Phi_{gen} - \Phi_{loss} \tag{3.10}$$

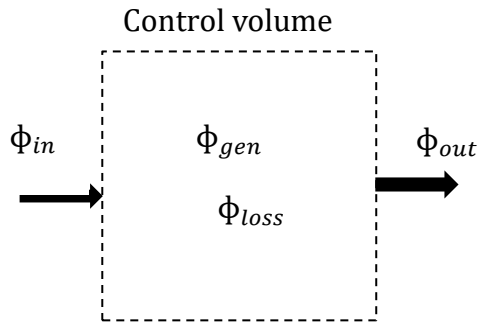

Figure 3-1 Basic control volume for the charge transport in the gas medium.

When an electric field applied to a gas dielectric, the charged particles in this region will experience a acceleration and movement. The movement caused by the external force, for instance, the electric field, etc. called drift movement. The movement caused by the number density gradient called diffusion movement. Electric current is formed in a gaseous medium when a directed flow of charged particles occurs.

In addition to drift of charged particles in electric field, diffusion due to temperature and density gradients [3.1,3.2] also contributes to electric current. When charges drift is much stronger than the diffusive effect, which is to say the applied electric field is strong and there is negligible charge density gradient, it is satisfactory to use the concept of electrical conductivity to directly relate the current density to electric field:

$$\mathbf{J}_G = \sigma_G \boldsymbol{E} \tag{3.11}$$

where σ_G is the gas electrical conductivity that is a function of charge density, composition and temperature. For open air, its value can be significantly affected by weather conditions and environmental factors such as pollution, humidity, pressure etc. It is expected that in most regions of the gas domain sufficiently away from the insulator and electrodes surface, it is valid to use an electrical conductivity to calculate the current density. Near the surface of the insulator, net space charge can be accumulated and the polarity of the charge depends on the direction of the normal electric field component. Charges can diffuse into the gas if the gradient of the charged particle number density is significant. Therefore, diffusion of charged particles near the insulator surface may need to be considered.

There are numerous of published work on drift properties of electrons and ions in the literature [3.3-3.5]. In recent years, drift properties have been investigated largely in the aspect of gas mixtures used for insulation. The classical kinetic theory of gases can be used to describe drift properties of electrons and charged particles approximately. In the absence of external forces, electrons in a gas region at temperature T move around with a Maxwellian energy distribution with a most probable value KT. Under the action of an electric field E a net motion in the direction of the field with drift velocity W, as can be seen in Figure 3-2,

$$\mathrm{W} = \frac{eE}{m}\left(\frac{l}{V}\right) = \frac{eE}{m}\tau \tag{3.12}$$

Where *V* and *l* are the velocity and the mean free path of the electron, and τ the average collision time. Since the mean free path *l* is inversely proportional to the gas pressure *P*, and the electron energy is a function of the reduced field *E/P*, the drift velocity is also a function of *E/P*.

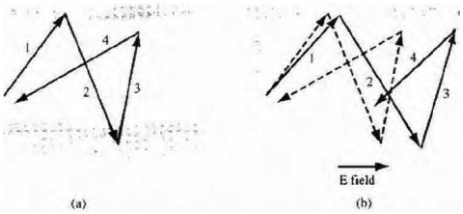

Figure 3-2 Typical random behavior of a charged particle in a gas region (a) without an electric field and (b) with an electric field.

The drift current can be governed by,

$$J_{drift} = J_{postive} + J_{negative} = q(\mu_n n + \mu_p p)\boldsymbol{E} \tag{3.13}$$

Diffusion is a mass transfer phenomenon that causes distribution of a species to become more uniform in space. If the concentration of a specie is initially not uniform, such as the concertation of one specie is much higher than the others in one region, then, as time passes, diffusion would cause a mass transfer in order to achieve a more uniform concertation distribution. The driving force of diffusion is the thermal motion of molecules. At temperature above zero, molecules never stop moving. The kinetic energy tells us that molecules are always in motion, and when molecules collide with others, the direction of the motion becomes random.

Diffusion of one species in a mixture of two species is controlled by the diffusion coefficient and gradient of number density of one of the species with a constant total pressure. Assuming a mixture consists of two species with number densities of n_1 and n_2 respectively at a temperature of T, the total pressure can be expressed by the following equation based on the ideal gas law:

$$\mathrm{P} = (n_1 + n_2)kT = nkT \tag{3.14}$$

If n_1 and n_2 are not constant over the space under consideration, there will be a flux of a species from a point to other points where the density of that specie is lower. The net flux $\varphi_i = n_i v_i$ of particles of type i is

$$\varphi_i \approx -\frac{1}{2} v_i \lambda_i \nabla n_i = -D_i \nabla n_i \tag{3.15}$$

where λ_i is the mean free path, v_i the average thermal speed and D_i the diffusion coefficient. In an equilibrium system, D_i of the charged particles is related to their mobility through:

$$D^{+/-} = \mu^{+/-} \cdot \frac{kT}{e} \tag{3.16}$$

where D is the diffusion coefficient for positive (+) or negative (-) ions, k the Boltzmann constant and e the electronic charge. The diffusion coefficient has a unit of m^2/s and the mobility has a unit of $m^2/(V.s)$.

The number density of charged particles in equilibrium is determined by the balance

of generation and loss sources. Carriers generation and recombination occur when electrons transits from the valence band to conduction band, as a result of interaction with electrons, holes or the crystal lattice in the dielectric. This process obeys the conservation rules of quantized energy and momentum. At low temperature (<1000 K) thermal ionization is negligible. Cosmic rays are the main source for seed electrons in a gas. Partial discharge and electron emission on electrode surface also lead to the presence of charged particles near an insulator. Depending on the strength of the applied electric field, ionization by electron impact can take place and produce free electrons. In electronegative gases such as air and SF_6 the small number of electrons are rapidly attached to molecules to form negative ions.

Recombination is the attachment of particles in the course of an encounter (collision) between a positive ion and an electron or between a positive ion and a negative ion. There are several kinds of recombination, such as the radiative recombination (RR), dielectronic recombination (DR), three body recombination (TBR) and etc. The electric field influence the recombination process greatly, not only because that the number density of charged particles can be enhanced by the field stress but also some externally imposed electric force and magnetic force can confine and shape the charged particles.

In the gas dielectric, such as SF_6 and air, the effect of conductivity is complicated. The ability of gas to conduct current depends on the number density of charged particles and collision frequency with other particles. Under a weak electric field, the number density of charged particles is controlled by their local generation and loss rate due to ionization and recombination and the drift of charged particles in electric field does not influence the number density remarkably. Thus, the concept of electrical conductivity is valid. However, like SF_6 at pressured-reduced gradients, $E/P \in (10\text{-}20)$ *MV/(m Mpa),* the concept of conductivity is meaningless due to the ion pair have a large negative value under this conditions [3.6]. Under strong electric field, the influence of charge drift becomes significant and the number density of charged particles varies remarkably in space. The electrical conductivity of the gas can no longer be treated as a material property. Thus, it is necessary to consider the transport processes of the charged particles.

Because of the high electronegativity of SF_6, low-energy electrons are attached to molecules by resonance capture (within 1 ps) and form a metastable association complex (SF6)-*. This also applies to air. It is commonly accepted that the number density of charged particles is controlled by the following governing equations

$$\frac{\partial n^+}{\partial t} = \frac{\partial n_{IP}}{\partial t} - K_r \cdot n^+ \cdot n^- + \nabla \cdot (D^+ \cdot \nabla n^+) - \nabla \cdot (n^+ \cdot b^+ \cdot E) \tag{3.17}$$

$$\frac{\partial n^-}{\partial t} = \frac{\partial n_{IP}}{\partial t} - K_r \cdot n^+ \cdot n^- + \nabla \cdot (D^- \cdot \nabla n^-) + \nabla \cdot (n^- \cdot b^- \cdot E) \tag{3.18}$$

where K_r is the recombination coefficient, $b^+ and\ b^-$ the mobility of positive/negative ions, and $D^+ and\ D^-$ the diffusion coefficient for positive/negative ions.

Once a solution of Equations (3.17) and (3.18) are obtained, the current density at any point in the gas domain can be derived, which is

$$\boldsymbol{J}_G = \boldsymbol{J}_D + \boldsymbol{J}_C = \frac{\partial \boldsymbol{D}}{\partial t} + e \cdot \boldsymbol{E} \cdot (n^+ \cdot b^+ - n^- \cdot b^-) - e \cdot \nabla (D^+ \cdot n^+ - D^- \cdot n^-) \tag{3.19}$$

The electric field in the gas is determined by Poisson's equation:

$$\nabla^2 \varphi_g = -\frac{e \cdot (n^+ - n^-)}{\varepsilon_r \varepsilon_0} \tag{3.20}$$

where e is the elementary electronic charge, 1.6×10^{-19} C.

3.4 Conduction and Charge Accumulation in the Surface Layer

A "surface layer" is used in a number of models [3.1-3.6] to deal with the situation where electric current conduction in a very thin layer below the surface of an insulator behaves differently from the bulk of the conductor as a result of differing electrical conductivity due to a special coating or surface contamination. The layer always has a thickness of the order of <100 um. The use of a surface layer in a model allows the effect of modified surface conditions to be taken into account when the electric field is calculated. An illustration of the surface layer is given in Figure 3-3.

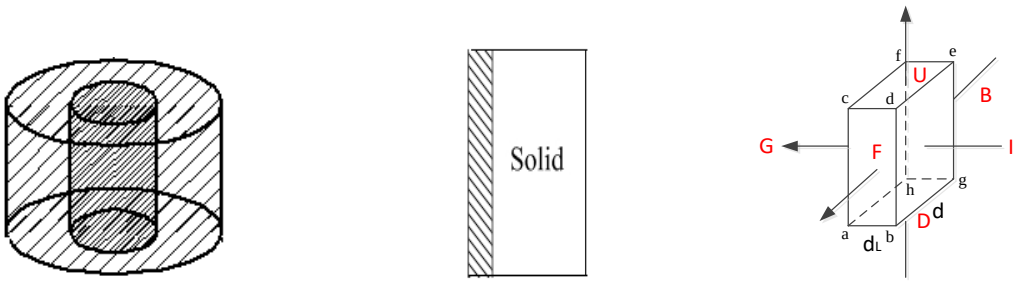

(a) (b) (c)

Figure 3-3 (a) Diagram showing the existence of a surface layer on an insulator (b) and (c) are the illustrative control volume in the surface layer. The 6 facets are denoted by capital letters showing its surface normal U (upwards), D (downwards), F (forward, positive x direction), B (backwards), G (gas side) and I (insulator side). The vertices are labeled as a, b, c, d, e, f, g, and h.

In an element as shown in Figure 3-3 (c), discontinuity of electrical conductivity and permittivity can appear across *facets G* and *I* when the type of insulation material changes. Ampere's Law in its integral form needs to be applied to each of the 6 facets. For a facet with peripheral c and surface s, the following equation holds:

$$\oint_c \boldsymbol{H} \cdot d\boldsymbol{l} = \int_s \boldsymbol{J} \cdot d\boldsymbol{s} \tag{3.21}$$

where $\boldsymbol{H}$ is the magnetic field intensity and $\boldsymbol{J}$ the current density across the facet. Summing the equations for all 6 facets makes the sum of the integrated magnetic flux density zero since integration is carried out twice on each side line with opposite unit vectors indicating the direction of integration. This gives the following equation:

$$\oiint [\boldsymbol{J}_G \cdot d\boldsymbol{s}_G + \boldsymbol{J}_I \cdot d\boldsymbol{s}_I + \sum_{i=1}^{4} \boldsymbol{J}_i \cdot d\boldsymbol{s}_i] = 0 \tag{3.22}$$

Because the thickness of the layer is so small, the area of facet G and facet I is virtually equal and Equation (3.22) can be rewritten as

$$J_{In} - J_{Gn} - \nabla \cdot (\sigma_{Vs} E) = 0 \tag{3.23}$$

where σ_{VS} is the volumetric electrical conductivity in the surface layer. The divergence operator in Equation (3.23) now only operates in the tangential direction of the surface layer. Equation (3.23) provides a link between the bulk of the insulator and the surrounding gas through the principle of current continuity.

The numerical treatment of the surface layer is an issue to be discussed. If the layer is compressed to a "zero" thickness, then interfacing conditions need to be defined on the interface between solid and gas domains after transforming Equation (3.23) into an appropriate form. Equation (3.23) means that the electrical current density coming out from the solid surface is different from that into the gas domain and the difference is controlled by the potentials (or E) distribution on the interface (the third term in Equation (8)). The advantage of this approach is the avoidance of extremely small mesh size that needs to be used to spatially resolve the surface layer. However, this can create additional difficulties in implementing the interface conditions in some software packages, depending on the user interface provided for setting up boundary conditions.

An alternative approach is to define a dedicated surface layer with a reasonable thickness such as 50 μm between the gas domain and the bulk of the insulator. In this case Equation (3.23) recovers to Equation (3.24) below,

$$\nabla \cdot (\sigma_{VSI} \nabla \varphi) = 0 \tag{3.24}$$

The accumulated charge on both faces of the surface layer can be derived using Equation (3.22) in a way similar to that for Equation (3.19) when φ and E are known from Equation (3.20). The volumetric electrical resistivity of solid dielectrics and the surface resistivity of solid dielectrics are summarised in next section.

3.5 Properties of the Insulating Material

There are three categories of material in the electrical engineering aspect, that is conductors, semiconductors and insulators. When a conductor is placed in the electric field, such as metal, that have a large number of free electrons. However, under steady state (equilibrium) conditions, the charge density inside of the conductor is always

zero. However, when a dielectric is placed in the electric field, the situation become different. Strictly speaking, an ideal dielectric (insulator) do not exist, because there is no zero-conductivity material exists, but there are materials with a conductivity smaller than 10^{-20} times. When subject to electric fields, these materials permit a negligible current to pass through and under the molecules would experience distortion at the same time. All the situations and influences need to be taken into account when discussing the dielectric properties.

3.5.1 Bulk Material Properties

Epoxy and epoxy-based composites are widely used as insulation materials in electrical apparatus, such as bushings, GIS and transformers etc. due to its excellent insulation performance and chemical stability. The fillers are always added to the material to increase its mechanical and insulation performance. The dielectric properties vary significantly depending on the filler type, size, operational conditions, etc.

When an electric field is applied on the object, the electrons will naturally move inside the object. The conduction electric current density is formed and (a measure of the flow of electrons) varies directly with the strength of the electric field. The conductivity provides a measure of how fast an electron can flow through a material. It is defined as in microcosmic,

$$\sigma_s = Neu_e \tag{3.25}$$

$$u_e = \frac{e\tau}{m_e} \tag{3.26}$$

Where N is electrons per unit volume, e is elementary charge, u_e is the mobility, m_e is the mass, τ is the mean time per collision.

Considering the other situation, when the dielectric is placed in a alternating field (AC) or when it is subject in the DC field considering the situation of polarity reversal, so for the Maxwell's equation, we have that

$$\nabla \times \mathbf{H} = J_i + \sigma_s \boldsymbol{E} + j\omega(\varepsilon' - j\varepsilon'')\boldsymbol{E} \tag{3.27}$$

So, we can define an effective conductivity

$$\sigma_{effective} = \sigma_s + \sigma_a \tag{3.28}$$

The first term σ_s is the static conductivity, the σ_a due to an alternating field.

It was reported in [3.6] that the bulk conductivity of epoxy material varies with the applied electric field

$$\sigma_{Vs} = \sigma_0 \cdot e^{\alpha \cdot E} \tag{3.29}$$

where σ_0 and α are both empirical coefficients relating to the resin material and casting technology, E is the applied electrical field strength. However, both coefficients can take values over a wide range of $10^{-19} - 10^{-12}\ S/m$ for σ_0 and $0.015 - 0.1\ m/MV$ for α. We have obtained that the selection of conductivity can be greatly influenced by the many factors, so assumption and approximation are needed when consider this kind of problem.

The same authors measured the conductivity of GIS-utilized epoxy resins with alumina and silica fillers as shown in Figure 3-4 below, and their results show that the conductivity varies insignificantly over 0 to 6 kV/mm at an average value of 2×10^{-14} S/m for fillers of Al_2O_3 and SiO_2. For field strength, larger than 11 kV/mm an average value of 8×10^{-13} S/m was obtained. There is no knowledge on the selection of these two coefficients for different commercial grade materials. It seems that the DC conductivity could be affected by partial discharge, polarization and space charge effects, electron injection from the cathode, etc.

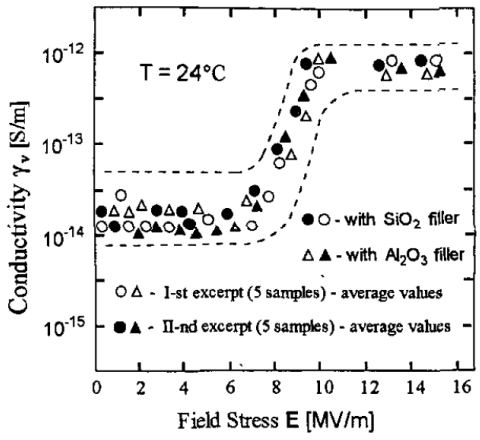

Figure 3-4 Field- dependent bulk conductivity of cast epoxy resin [3.6].

Other experimental evidence in [3.7] shows that the bulk conductivity remains constant at 10^{-14} S/m for untreated epoxy specimen when the applied field lies in the range of 1kV/mm to 5 kV/mm, as shown in Figure 3-5. The surface conductivity is higher with the horned specimen.

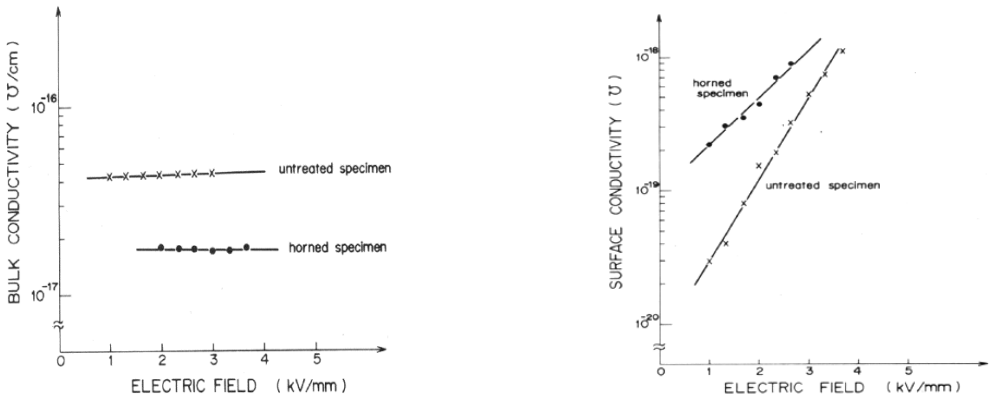

(a) *(b)*

Figure 3-5 (a) Experimental results for the bulk electrical conductivity of epoxy as a function of the applied electric field. (b) Experimental results for the surface conductivity of epoxy specimen as a function of the applied electric field.

In more recent modelling work [3.8,3.9], a value of 3.33×10^{-18} S/m was chosen to obtain results that agree well with the measurements. Given the large difference in literature, the bulk conductivity of epoxy insulator with or without fillers should be obtained by measurement if reliable prediction based on charge transport model is to be obtained. For the work in next chapter, a value of 1.6×10^{-16} S/m is provided by the manufacturer and used in the further modelling and verification.

When an external electric field is applied, the dipoles in the dielectric would align with field, this action causes a term to be added to the electric flux density that has the same vector direction as the applied field. This relationship can be mathematically described as

$$\boldsymbol{D} = \varepsilon_0 \boldsymbol{E} + \varepsilon_0 x_e \boldsymbol{E} \tag{3.30}$$

The term x_e is known as the electric susceptibility and serves as a proportionality constant between the electric field and the portion of the electric flux density caused by the presence of the dielectric, one can rewrite the equation as

$$\vec{D} = \varepsilon_0 \varepsilon_r \vec{E} \tag{3.31}$$

Where ε_r is known as the relative permittivity of the medium.

Electric permittivity determines the charge storage capacity of a dielectric material as well as influences the electric field distribution in a composite insulation system. Considering an AC field applied to a dipole, when the field first strikes the dipole, the dipoles rotates to align itself with the field. As time passes, the electric field reverses its direction, and the dipole must rotate again to remain aligned with the correct polarity. As it rotates, energy is lost through the generation of heat (friction) as well as the acceleration and deceleration of the rotational motion of the dipole. The degree to which the dipole is out of phase with the incident electric field and the losses that ensure determine how large the imaginary part of the permittivity is as a function of material and frequency.

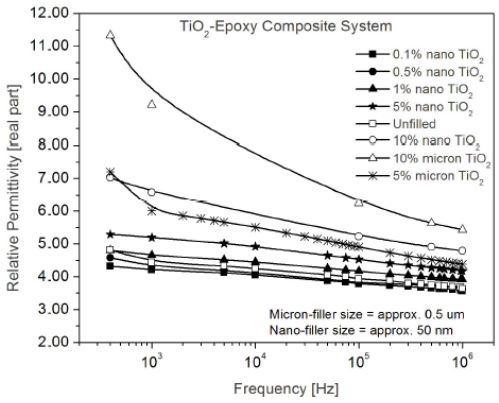

Figure 3-6 Variations of permittivity with respect to frequency in epoxy-TiO2 composites (lines connect the experimental data points).

The permittivity influence factors can be found in [3.10], Singha presented that, the

effective permittivity in nanocomposites material is determined by dielectric polarization and relaxation mechanisms in the bulk of the composite material. As can be seen in Figure 3-6, the effective permittivity of unfilled epoxy and epoxy composites increase with decreasing frequency, and in the typical range of 4-11. Permittivity is a frequency dependent parameter in polymer systems and is governed by the number of orientable dipoles present in the system and their ability to orient under an applied electric field. Usually, the molecular groups which are attached perpendicular to the longitudinal polymer chain contribute to the dielectric relaxation mechanisms. At lower frequencies of applied voltage, all the free dipolar functional groups in the epoxy chain can orient themselves resulting in a higher permittivity value at these frequencies.

Another research from Qi Wang's measurements in [3.11], suggested that the composite with micro-size filler seems to have a higher permittivity than the nanocomposites, and this is probably due to immobility of epoxy chain in nanocomposites due to a strong interaction at the interface as shown in Figure 3-7. At the same time, they observed that a large amount of homo-charges is accumulated adjacent to both electrodes for unfilled epoxy. As the duration of the applied voltage increases, the amount of charge in the specimen increase as well. In the computation, considering the relevant reference [3.6-3.9,3.12] the relative permittivity of epoxy always can be chosen in the range of 2.5-5.

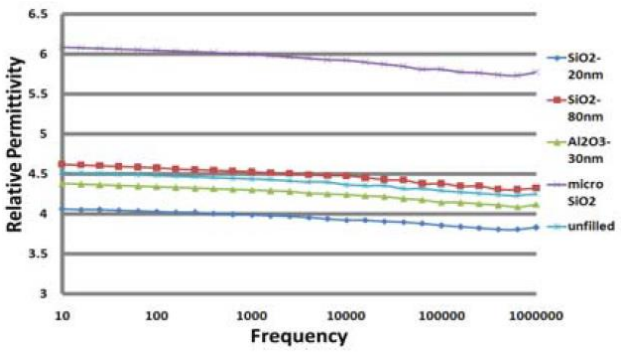

Figure 3-7 Variations of permittivity with respect to filler size [3.11].

3.5.2 Drift and Diffusion

In the presence of an electric field in the gas dielectric, the charged particles are experience a force results in them to drift with a velocity that varies directly with the field and inversely with the density of the gas through which it moves. The drift velocity component in the field direction of unit strength is defined as the mobility

$$\mu = \frac{w}{E}(m^2/V) \tag{3.32}$$

Where W is the average drift velocity in field direction and E is the electric field strength. The mobility is mainly a characteristic of the gas through which the ion moves and is independent of E/P over a wide range of E/P so long as the velocity gained by the ion from the field is considerably less than the average thermal velocity of the gas through which the ion moves.

There has been a considerable amount of work on the measurement of the mobility of negative ions in SF_6 [3.13-3.20]. However, the gas pressure used in almost all the measurements was at most a few hundred mbar, much low than the pressure used in GIS or wall bushings. At low pressure, the mobility of negative SF_6 ions is around 5×10^{-5} $m^2/V/s$. Schmidt and Jungblut [3.19] were the first authors to obtain the mobility of SF_6 ions at high pressure from 0.25 bar to 21 bar. They obtained a value of 9×10^{-6} $m^2/V/s$ for both positive and negative SF_6 ions. The mobility remains constant for electric field strength below 10^5 V/m at 0.25 bar and below 6×10^5 V/m at 21 bar. A value of 3.6×10^{-5} $m^2/V/s$ for negative SF_6 ions at 1 bar was obtained by Kindersberger [3.8,3.9]. Since the results in [3.19] were obtained under conditions close to the real application, the value of 9×10^{-6} $m^2/V/s$ is therefore used in the present work.

Diffusion is a mass transfer phenomenon that causes distribution of a species to become more uniform in space. The diffusion flux is governed by Fick's Law related to the concentration under assumption of steady state. It is indicated that the flux goes from regions of high concentration to regions of low concentration across a concentration gradient. In more dimensions, we have

$$\mathbf{J} = -D\nabla\varphi \tag{3.33}$$

J is the diffusion flux, D is the diffusion coefficient, φ is the concentration. The diffusion coefficient has units of area per time (m^2/s).

The diffusion coefficient can be predicted from the values for the mean free path and average velocity for the mean free path and average velocity for molecules in an ideal gas from the Maxwell- Boltzmann distribution, as shown below, diffusion is faster with higher temperature.

$$\mathrm{D} \propto \frac{T^{\frac{3}{2}}}{p} \tag{3.34}$$

Under the other situation where there are particles or large molecules in a viscous fluid, the Stokes- Einstein equation can be employed:

$$D = \frac{kT}{6\pi\mu r} \tag{3.35}$$

Where k is the Boltzmann constant, μ is the viscosity, r is the radius of the diffusing particle. This equation is derived on the assumption that the particles obey Stroke's Law for drag, such that the drag exerted on diffusing molecules, by the solvent molecules, can be computed. Note that solvent viscosity itself strongly depends on temperature, so this equation doesn't apply to linear relation of solution-phase diffusion coefficient with temperature. Rather, the diffusion coefficient normally obeys a relation close to an exponential Arrhenius relation:

$$D = D_0 \exp(\frac{E_{diff}}{RT}) \tag{3.36}$$

Here, E_{diff} is an activation energy of diffusion, the exponential form of this relation means that diffusion coefficients in the solution phase can grow quickly with temperature.

There is very little work on the measurements of diffusion coefficient of SF_6 ions in their parent background gas. A value of 7×10^{-8} m^2/s is derived from the results given by Nakamura [3.21] by extrapolating his results to an E/N value corresponding to the case under study (6 bar and 300 K for SF_6). A value of 2.4 for the energy factor, defined as $39.6D/\mu$ where D is diffusion coefficient of negative ions in SF_6 and μ their mobility, was obtained by Naidu and Prasad [3.18]. Using the mobility value of 9×10^{-6} $m^2/V/s$

given by Schmidt and Jungblut [3.19], a diffusion coefficient of 5.45×10^{-7} m^2/s was obtained. Using Einstein's relationship and the mobility of Schmidt and Jungblut, we can also obtain a value of 2.3×10^{-7} m^2/s. The closest experiment conditions to the real application were used by Kindersberger et al [3.8, 3.9] at 1 bar and room temperature and a much smaller value of 2.84×10^{-9} m^2/s was obtained. It will be shown in further section that diffusion plays an unimportant role in the charge accumulation process. The value of 2.84×10^{-9} m^2/s will be used in the present model.

3.5.3 Ionization and Recombination

The number density of charged particles in a stationary, weakly ionized plasma in equilibrium is determined by the balance of generation and loss sources. The electrical conductivity depends not only on the mobility, but also on the number density. There have to be charged particles in a gaseous medium for it to conduct electricity. At low temperature (<1000 K) thermal ionization is negligible. Cosmic rays are the main source for seed electrons in a gas. Partial discharge and electron emission on electrode surface also lead to the presence of charged particles near an insulator. Depending on the strength of the applied electric field, ionization by electron impact can take place and produce free electrons. In electronegative gases such as air and SF_6 the small number of electrons are rapidly attached to molecules to form negative ions. Recombination is the attachment of particles in the course of an encounter (Collison) between a positive ion and an electron or between a positive ion and a negative ion. When describing this phenomenon, instead of using the concept of effective recombination cross section, the recombination coefficient is often applied. At low temperature, the number density of charged species is low, hence the low electrical conductivity. However, it is this small number of charged particles that contribute to the leakage current under DC conditions and accumulation of charges on insulator surface.

It is commonly accepted that in electronegative gases free electrons are rapidly attached to molecules to form negative ions, thus in air or SF_6 charged particles take the form of positive and negative ion pairs. Their number density can vary at different

geometrical locations on the globe or even in different floors of a building [3.22]. Near sea level, the interaction of cosmic radiation with the atmosphere gives rise to a penetrating component (80%, mainly pmesons) and a soft component (20%, mainly electrons and photons). The intensity of cosmic radiation at sea level tends to be highly stable. The total ionization rate of cosmic radiation in atmospheric air is about 2 ion pairs (IP)/cm^3 /s at sea level [3.22]. Interaction of the cosmic rays with the GIS enclosure can also lead to the multiplication of ionization. Figure 3-8 from [3.22] show measured ionization rate in N_2 and SF_6 in cylindrical vessels at different pressures. The ion pair generation rate increases from 10 to 30 IP/cm^3/s when the gas pressure increases from 1 bar to 5 bar.

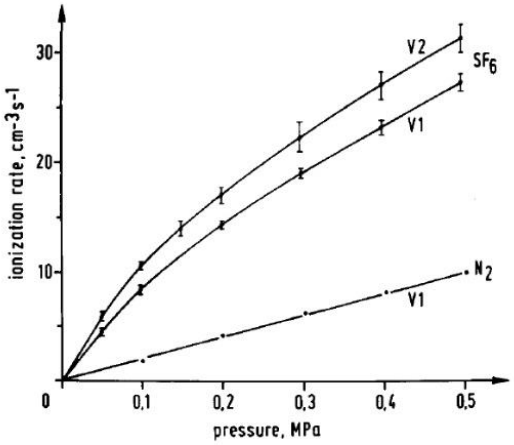

Figure 3-8 Ionization rates in N_2 and SF_6 in cylindrical test vessels of differing outer diameters (Vl: 52 cm: V2 27.8 cm diameter) at the same physical location. Bars mark lowest and highest measured values [3.22].

Positive and negative ions tend to re-combine into neutral molecules within a short time, as shown in Figure 3-9 and Figure 3-10. There are different mechanisms responsible for ion-ion recombination such as mutual neutralization, three-body recombination and tidal recombination [3.23]. A recombination coefficient is normally used to account for this effect. In SF_6 its value was mainly obtained by experiment. It changes with pressure and the applied electric field. A value of 2.27×10^{-13} m^3/s was used in [3.12]. Its value obtained by experiment is 7×10^{-13} m^3/s at E/N of 40-80 Td in

[3.24] and 1.2×10^{-12} m^3/s in the pressure range of 300-700 torr in [3.25]. For air, results given in [3.26] and [3.27] show that the recombination coefficient is approximately a constant with a value of $K_r = 1.4 \times 10^{-6}\ cm^3/s$ for air at 1 bar and 293 K.

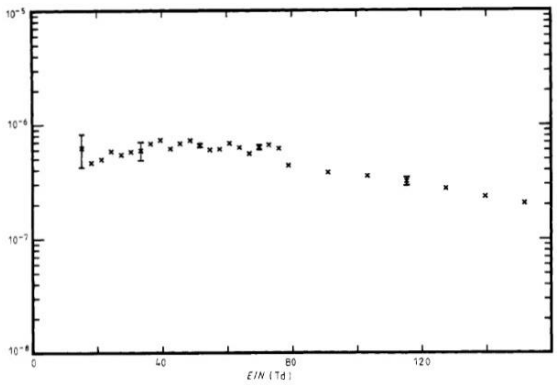

Figure 3-9 Ion-ion recombination rates in pure sulphur hexafluoride as a function of the reduced electric field strength [3.28]. The unit of recombination coefficient (the vertical axis) is cm^3/s.

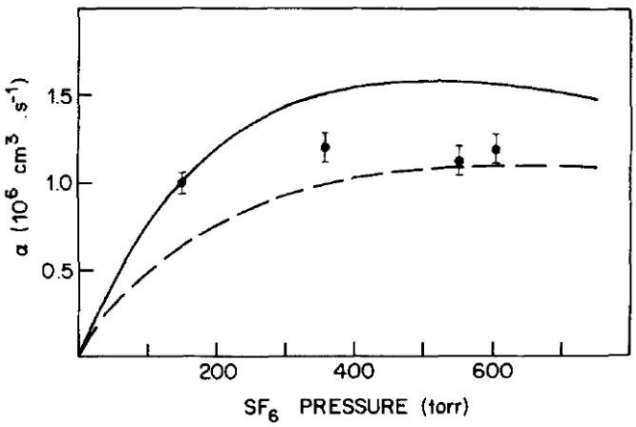

Figure 3-10 Pressure dependence of the homogeneous ion combination coefficient in SF_6 at 298 K. solid circles are the experimental results, solid line is the calculated three-body coefficient for $SF_6^+ + SF_6^- + SFs$; dashed line is the calculated three-body coefficient for $SF_6(SF_6) + SF_6(SF_6) + SF_6$.

The other work was done by Kindersberger et al [3.29] who obtained values from 2.6

$\times 10^7$ /m^3/s in ground floor of buildings to 5.5 $\times 10^7$ /m^3/s outdoor at 4 bar. Their results were extrapolated to 6 bar based on the measured values at different pressures, giving a value of 3.3×10^7 /m^3/s, which is used in the present work. The recombination coefficient of positive and negative SF_6 ions was also measured by Kindersberger [3.29] at 1 bar with a value of 1.7×10^{-12} m^3/s. Since the recombination coefficient at higher pressure is approximately inversely proportional to pressure, therefore in the present case of 6 bar, the recombination coefficient is estimated as 2.8×10^{-13} m^3/s for use in further section.

3.6 Summary

A mathematical model for charge transport in HVDC bushing space has been developed and established in this chapter including generation, recombination, drift and diffusion movement of negative and positive ions. Considering this type of DC bushing has a considerable length, in order to study the charge transport and accumulation process, some approximations have been applied to the geometry of the support spacer. The electrical properties of solid and gaseous insulation media are functions of a range of environmental and physical parameters. Their values differ substantially in different publications. This chapter summarizes the values and provides a data base as reference for the choice of the relevant parameters. The negative/positive ions properties in the surrounding region are assumed to be uniform and represented by relevant coefficients. The model is able to include a thin surface layer which is coupled to the solid insulation material domain and the gas domain. The thickness of surface layer is required as the interface conditions between the gas and solid dielectrics.

3.7 Reference

[3.1] W.F. Schmidtand and H. Jungblut, “Ion mobility and recombination in compressed sulphur hexafluoride,” *Journal of Physics D: Applied Physics*, vol. 12, pp. L67-L69, 1979.

[3.2] E.A. Mason and E. W. McDaniel, “Kinetic theory of mobility and diffusion,” in Transport properties of ions in gases. Germany: Wiley VCH, 1988, pp.126-178.

[3.3] J. Hirschfelde, C. Curtiss, R. Byron Bird, *Molecular Theory of Gases and Liquids*. New York, Wiley, 1954.

[3.4] R. S. Devoto, “Transport properties of ionized monatomic gases,” *Physics of Fluids*, vol.9, pp.1230–1240, 1966.

[3.5] R.E. Robson, *Introductory Transport Theory for Charged Particles in Gases*, UK: World Scientific, 2006.

[3.6] E. Volpov, “Electric field modelling and field formation mechanism in HVDC SF6 gas insulated systems,” *IEEE Trans. Dielectr. Electr. Insul.,* vol. 10, pp. 204-215. April 2003.

[3.7] K. Nakanishi, A. Yoshioka, Y. Arahata and Y. Shibuya, “Surface charging on epoxy spacer at DC stress in compressed SF_6 gas,” *IEEE Trans. Power App. Syst.,* vol. PAS-102, No. 12, 1983.

[3.8] A. Winter and J. Kindersberger, “Transient field distribution in gas-solid insulation systems under DC voltages,” *IEEE Trans. Dielectr. Electr. Insul*., vol. 21, pp. 116-128, 2014.

[3.9] A. Winter and J. Kindersberger, “Stationary resistive field distribution along epoxy resin insulators in air under DC voltage,” *IEEE Trans. Dielectr. Electr. Insul.*, vol. 19, pp.1732-1739, 2012.

[3.10] S. Singha and M. J. Thomas, “Dielectric properties of epoxy nanocomposites,” *IEEE Trans. Dielectr. Electr. Insul*., vol. 15, pp.12-23, 2008.

[3.11] Q. Wang, G. Chen and S. Alghamdi, “Influence of nanofillers on electrical characteristics of epoxy resins insulation,” In *Solid Dielectric of Conf*., Germany., 2010, pp. 1-4.

[3.12] U. Straumann, M. Schuller and C. M. Franck, “Theoretical investigation of HVDC disc spacer charging in SF6 gas insulated systems”, *IEEE Trans. Dielectr. Electr. Insul.*, vol. 19, No. 6, pp. 2196-2205, 2012.

[3.13] L. G. Christophorou and R. J. Van Brunt, "SF_6/N_2 mixtures: basic and HV insulation properties", *IEEE Trans. Dielectr. Electr. Insul.,* vol. 2, no. 5, pp. 952-1003, 1995.

[3.14] I. A. Fleming and J. A. Rees, "The drift velocities of ions in sulphur hexafluoride", *Journal of Physics B: Atomic and Molecular Physics*. vol. 2, no. 7, pp. 777-779, 1969.

[3.15] D. T. Blair, B. H. Crichton, F. J. Al-Kindi and T. L. Sharma, "Drift velocities of positive ions and negative ions in cylinder SF_6", *Journal of Physics D: Applied Physics.* vol. 22, no. 6, pp. 755-758, 1989.

[3.16] F. Li Aravena and M. Saporoschenko, "Mobilities of positive ions in sulfur hexafluoride gas", *The Journal of Chemical Physics,* vol. 98, no. 11, pp. 8888-8891, 1993.

[3.17] P. L. Patterson, "Mobilities of negative ions in SF_6", *The Journal of Chemical Physics*, vol. 53, no. 2, pp. 696-704, 1970.

[3.18] M. S. Naidu and A. N. Prasad, "Mobility and diffusion of negative ions in sulphur hexafluoride", *Journal of Physics D: Applied Physics*, vol. 3, no. 6, pp. 951-956, 1970.

[3.19] W. F. Schmidt and H. Jungblut, "Ion mobility and recombination in compressed sulphur hexafluoride", *Journal of Physics D: Applied Physics*. vol. 12, no. 6, pp. L67-L70, 1979.

[3.20] J. Winkelmann, "Diffusion of sulfur hexafluoride", in *Gases in Gases, Liquids and their Mixtures*, Springer, Berlin Heidelberg: 2007, pp. 121-124.

[3.21] Y. Nakamura, "Transport coefficients of electrons and negative ions in SF_6", *Journal of Physics D: Applied Physics*, vol. 21, no. 1, pp. 67-72, 1988.

[3.22] N. Wiegart, L. Niemeyer, F. Pinnekamp, W. Boeck, J. Kindersberger, R. Morrow, W. Zaengl, M. Zwicky, I. Gallimberti and S.A. Boggs, "Inhomogeneous field breakdown in GIS - The prediction of breakdown probabilities and voltages: Part ii: ion density and statistical time lag", *IEEE Trans. Power Del.,* vol. 3, pp. 931-938, 1988.

[3.23] M. R. Flannery, "Electron-ion and ion-ion recombination", *Advances in Atomic,*

Molecular, and Optical Physics, vol.32, pp. 117-147, Dec. 1996.

[3.24] M.C. Cornell and I.M. Littlewood, "Ion-ion recombination in mixtures of methane and sulphur hexafluoride", J. Phys. D: Appl. Phys., vol. 20, pp. 616-621, 1987.

[3.25] D.E. Wilson, W. J. Quiring and D.A. Armstrong, "Homogeneous ion combination coefficients in sulphur hexafluoride", *Journal of Applied Physics*, vol. 47, pp. 1194-1195, 1976.

[3.26] H. A. Erikson, "On the nature of the ions in air and in carbon dioxide", *Physical Review*, vol. 24, pp. 502-509, 1924.

[3.27] S. McGowan, "Ion-ion recombination in laboratory air", *Phys. in Med. and Bio.,* vol. 10, pp. 25-40, 1965.

[3.28] M.C. Cornell and I.M. Littlewood, "Ion-ion recombination in mixtures of methane and sulphur hexafluoride", *J. Phys. D: Appl. Phys.*, vol. 20, pp. 616-621, 1987.

[3.29] J. Kindersberger, N. Wiegart and S. A. Boggs, "Ion production rates in SF_6 and the relevance of gas-insulated switchgear", in *Electrical Insulation & Dielectric Phenomena of Conf.*, 1985, pp. 123-129.

CHAPTER 4 MODEL IMPLEMENTATION AND VERIFICATION

The charge transport model developed and established in Chapter 3 is implemented in COMSOL Multiphysics. COMSOL is a powerful Partial Differential Equation (PDE) solver based on the Finite Element Method (FEM). It is known that the FEM is most suitable for diffusive PDEs such as the Poisson's equation for the calculation of electrostatic field. However, it is not effective in solving PDEs with strong convection such as the charge transport equations in gas. COMSOL is used in the present work because it is a powerful and user-friendly software package to couple electrical, charge transport and heat transfer processes, which is needed in the PhD project.

By implementation which means the set-up of the governing equations, material properties and boundary and initial conditions in the format specified by the software. It is also important to obtain converged solution. It has been shown in existing work that special measures have to be taken to obtain convergence of solution for convection dominated situations. In the present work, strong drift of charged particles occurs at very high electric field, corresponding to high applied DC voltage.

Section 1 in this chapter introduces the basic features of the finite element method and modelling considerations. Section 2 uses a typical geometry of the computational domain to demonstrate the pre-processing procedures and considerations such as mesh generation and refinement, division of domain into sub-domains with different requirement, and the important details of the model implementation. Section 3 presents a study into the influence of mesh size and optimization of mesh system. Section 4 is devoted to the control and convergence using typical examples. The verification of the model using reliable experimental results is given in Section 5. Finally, a summary of the work is provided in Section 6.

4.1 Modelling Considerations and Pre-processing

It is always use mathematics to understand and quantify the physical phenomena comprehensively in engineering aspect. There are many methods to solve the mathematical problems as shown in Figure 4-1. The description of the laws of physics for space and time-dependent problems are usually expressed in terms of partial differential equations (PDEs). For the vast majority of geometries and problems, these PDEs cannot be solve by the traditional analytical methods, instead of, they need to be solved using the numerical methods. The finite element method is a numerical method for solving problems which are described by partial differential equations [4.1-4.3].

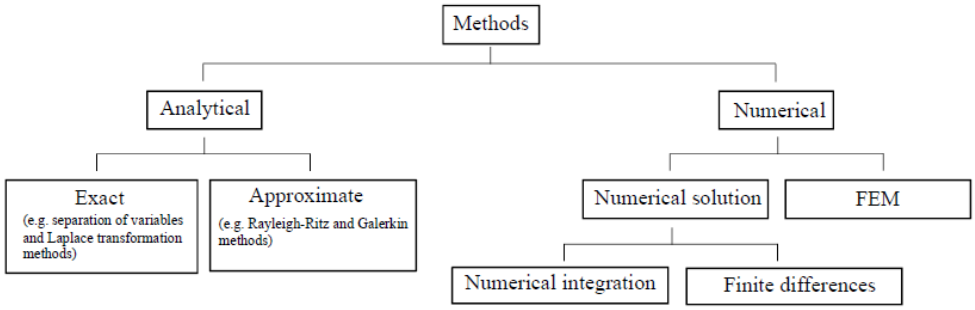

Figure 4-1 The classification of general methods in the calculation.

Starting from the history, in 1909 Ritz developed an effective method [4.4] for the approximate solution of problems in the mechanics of deformable solids. It includes an approximation of energy functional by the known functions with unknown coefficients. In 1943 Courant considerably increased possibilities of the Ritz method by introduction of the special linear functions defined over triangular regions and applied the method for the solution of torsion problems [4.5]. As unknowns, the values of functions in the node points of triangular regions were chosen. Thus, the main restriction of the Ritz functions – a satisfaction to the boundary conditions was eliminated. The Ritz method together with the Courant modification is similar with FEM proposed independently by Clough many years later introducing for the first time in 1960 the term “finite element” in the paper “The finite element method in plane

stress analysis" [4.6]. The reason of wide spreading of FEM in 1960s is due to the high speed of processing and better storage capability of computers. Until now, this method has been successfully applied for the solution of several other types of engineering problems like heat conduction, fluid dynamics, electric and magnetic fields, and others as well.

Discretization of the domain into finite elements is the first step in the finite element method. This is equivalent to replacing the domain having an infinite number of degrees of freedom by a system having finite number of degrees of freedom. An establishment of a model obeys the following processes, preprocessing, solution and postprocessing. Preprocessing is the first step, and it is based on the understanding of the physical problem including a qualitative knowledge of the structural response to be predicted, knowledge of the basic principles of mechanics, and it includes the geometry draw, element types, properties and constraints definitions. Solution is the second step and it is related to the FEM to compute the unknow values. And the last is postprocessing containing sophisticated routines used for sorting, printing, and plotting selected results from a finite element solution.

4.2 Typical Structure and Geometry

This section introduces the typical structure of the spacer in the wall bushing, and its 3D geometry in the COMSOL. Based on the reasonable approximations, the 2D asymmetric case is introduced.

4.2.1 The Schematic Product and 3D Geometry

DC wall bushings operating at 500kV and above are normally designed with a gas-filled structure. This type of DC bushing has a considerable length and its central conductor has to be mechanically supported by one or more spacers which are subject to severe electric stress. For the study of the charge transport and accumulation process, it is necessary to introduce approximations to the geometry of the support spacer in the HVDC bushing which contains the insulator (spacer). The inclusion of the whole

structure of the bushing in computation is impossible because of the limitations in computing time and computer memory. To obtain reasonable computational results the meshes have to be sufficiently dense in regions where the electric field is strong or their existing large gradient of charged particle number density. We therefore need to focus our effort in regions that are influential to the accumulation of charges and subsequently the occurrence of breakdown along the insulator surface.

The schematic diagram of a Pinggao 1100 kV HVDC bushing with insulator is given in Figure 4-2. The bushing structure has an overall length of 27.93 m (including the two terminal rings). The gas tight bushing structure is filled with SF_6 at 6 bar (absolute) to provide insulation between the central conductor and the bushing outer walls. The inner diameter of the middle barrel of the bushing (where the intermediate flange is), which is metallic and to be fitted into the wall, is 1.35 m. The maximum potential difference is between the live central conductor and the earthed metallic wall of the barrel. The supporting rod insulator, also called the spacer as shown in Figure 4-2(b), has to provide sufficient mechanical strength to hold the central conductor firmly in its intended position and at the same time provide adequate insulation between the live conductor and the earthed wall. On each side, there is an insulator consisting of the central conductor, field shielding arrangement, and an insulation tube made of glass fiber reinforced epoxy with silicone rubber shielding. The electric design will need to ensure that local electric field enhancement is minimized to achieve the smallest possible overall dimensions for a given voltage and current rating. This can only be achieved through a clear understanding of the dielectric behavior of the insulation system under practical conditions.

(a) *(b)*

Figure 4-2 Schematics of an HVDC bushing insulator (a) and part of its internal structure (b). A rod insulator (the spacer) is used to provide mechanical support to the central conductor.

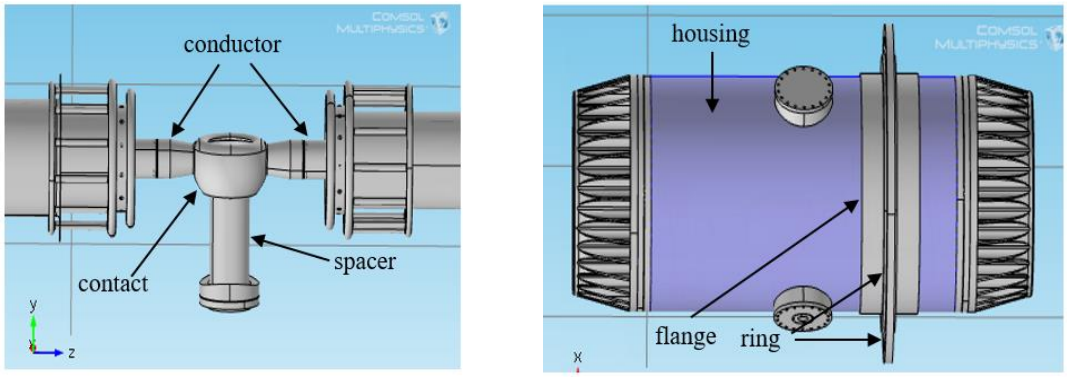

(a) *(b)*

Figure 4-3 (a) 3D structure of internal view of the central part of the bushing (b) External view of the central part of the bushing.

As shown in Figure 4-3 (a), two conductors are connected by a bowl-shaped contact, and the spacer is located below the contact to mechanically support the heavy conductors. The metallic barrel housing of the bushing, as shown in Figure 4-3(b), is grounded and fitted in the wall. In the longitudinal direction, the spacer is neighbored by two copper rings circling the central conductor. The cross-sectional view of the bushing is shown in Figure 4-4. The spacer is made by epoxy resin composition material and surrounded by gaseous dielectric of SF_6 and Air. Both the upper and lower

electrodes are made by copper. The material properties are discussed in the Chapter 3.

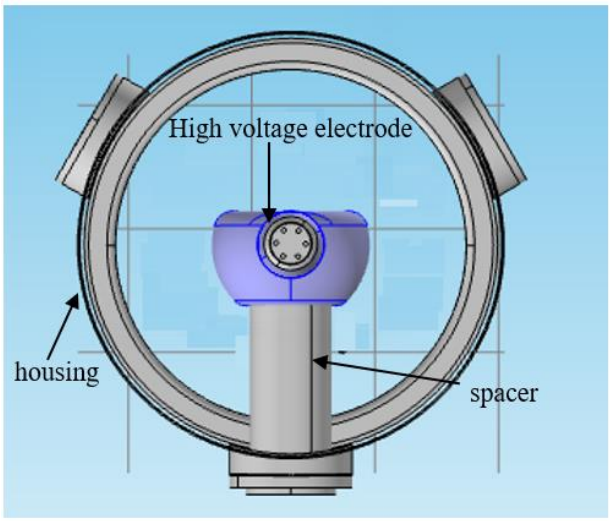

Figure 4-4 Cross-sectional view of the bushing

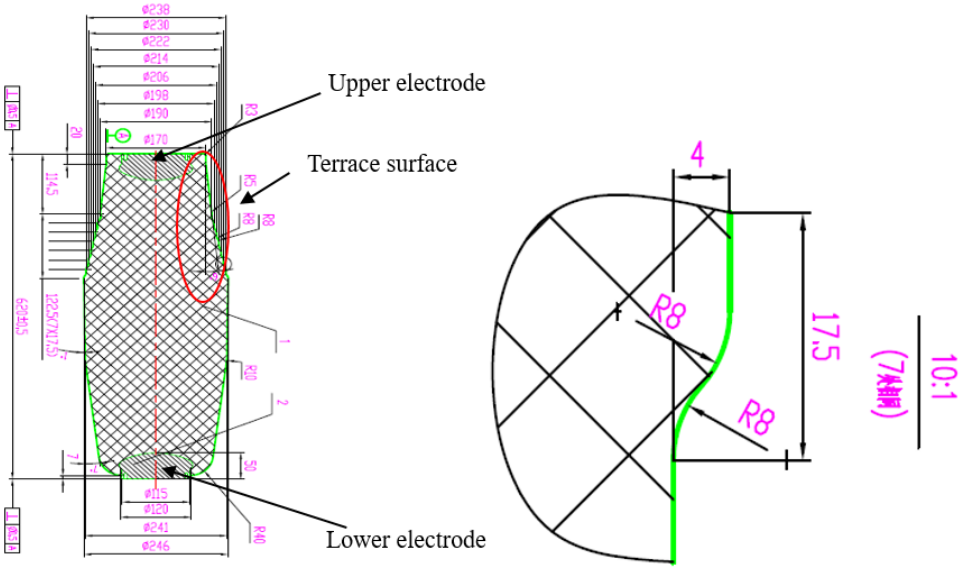

(a) Profile of the spacer *(b) Enlarged view of the terrace surface*

Figure 4-5 Configuration and measurements of the spacer (support insulator).

As shown in Figure 4-5 (a), the spacer itself is axis-symmetric and two electrodes are embedded into it; the upper electrode is designed to connect the housing with ground

potential, whereas the lower electrode is designed to connect the conductors with system voltage. The spacer is measured in millimeters, and the maximum width and height are 246mm and 620mm, respectively. In order to increase the creepage distance along the surface and hence to enhance its withstand voltage, a part of the surface of spacer is designed to be terrace in shape, as indicated in Figure 4-5(a). The enlarged view of the terrace surface is shown in Figure 4-5(b). The three-dimensional simplified geometry of the central part of the bushing is shown in Figure 4-6 and Figure 4-7.

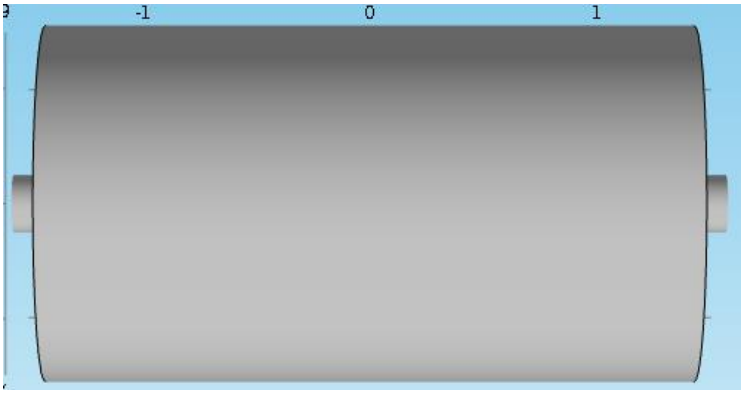

(a) External view of the central part of the bushing

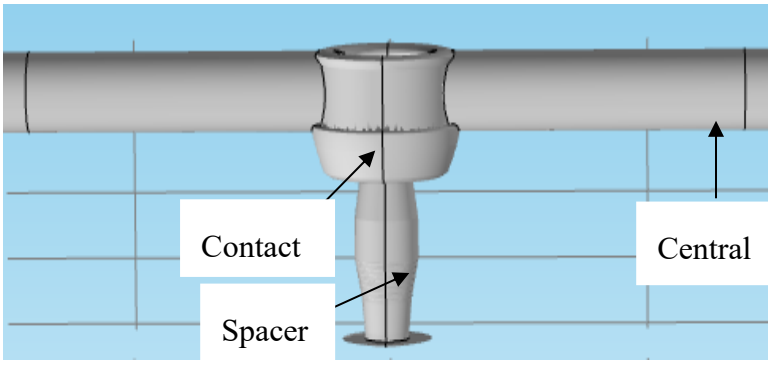

(b) Internal view of the central part of the bushing

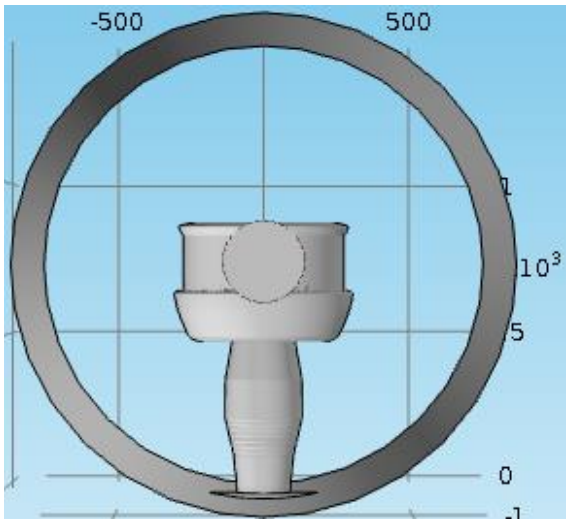

(c) Cross sectional view of the bushing

Figure 4-6 Three-dimensional model including spacer in the bushing system

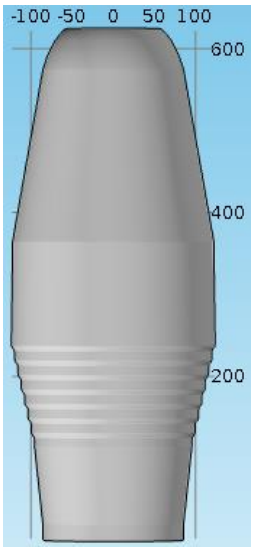

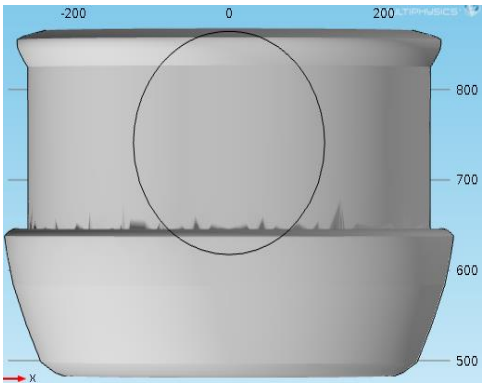

(a) Profile of the spacer *(b) Profile of the contact*

Figure 4-7 The separate parts of the support insulator and the cap on the top.

4.2.2 The Axisymmetric 2D Geometry

To simplify the study yet without missing the most important features in relation to charge accumulation, a computational domain of axis-symmetry is chosen with a

dimension comparable to that of the Pinggao bushing in the radial direction. The main central conductor is represented by a cap connected to the top electrode and is assigned the applied voltage. The strongest assumption in this work would be the domain boundary in the axial direction. As can be seen from Figure 4-8, the domain has a spherical shape. This means that we impose an earthed and curved metallic wall in the axial direction of the domain and force the charge number density to zero on the wall surface (details can be seen in the description of the boundary condition section). Given that there is a real earthed wall of the barrel at the middle section of the bushing, this assumption is not going to change the most important features of the spacer in relation to charge accumulation on its surface and ion number density distribution in the gas domain.

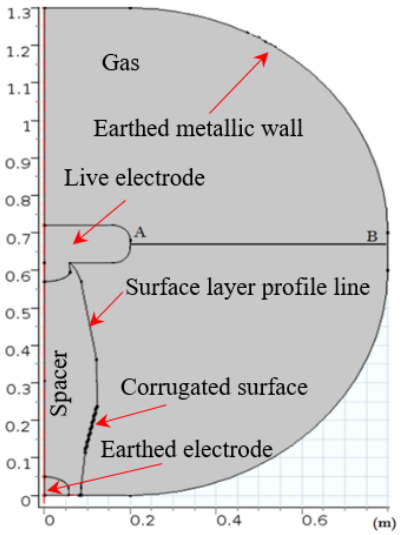

Figure 4-8 Cross-sectional view of an axisymmetric computational domain approximating the discharge environment around the spacer in the real bushing. Line AB will be used later to plot the distribution of physical quantities.

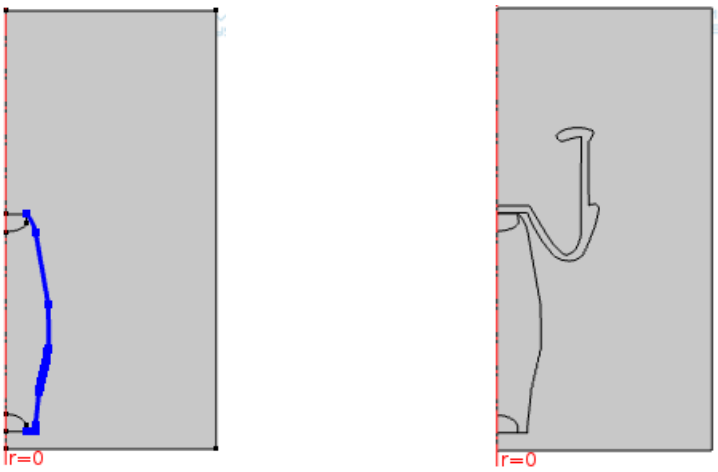

(a) (b)

Figure 4-9 Two different GEOs used in the computation. (a) is the original shape, without the central HV electrode. (b) is with the large contact as part of the central electrode.

The actual shape and dimension of the spacer in the Pinggao bushing is used in the present work. This spacer has a length of 0.6 m and a maximum radius of 0.12 m. The surface of the lower part of the spacer is corrugated with ridges and grooves to increase the creepage distance, as shown in Figure 4-9. The two electrodes protrude into the spacer to fix the spacer in its position and to minimize the field strength at the triple junction. Some different geometries are employed to investigate the shape influence in order to optimize the spacer design.

4.3 Mesh Refinement and Sensitivity Study

4.3.1 Mesh Refinement in COMSOL

The accuracy obtained from the mathematical model is closely related to the finite element mesh which used in the simulation [4.7]. The finite element mesh subdivides the geometry into many smaller elements, over which a set of equations describing the physical problem. As the finite element (mesh) getting smaller and smaller, so as the mesh is refined, the computational solution would approach to the true solution. This process plays a key role in simulation in order to improve the accuracy of the results.

During the simulation process, first starting from a mesh that is as coarse as possible, called preliminary mesh, that require less computational resources and it may give a inaccurate solution, but it can be used as a rough verification and as a quick check on the applied conditions. It also provides overall features of the results, which can help user to determine where are the critical regions. After computing the case on the coarse mesh, the process of mesh refinement begins. Mesh refinement is the process that resolving the mathematical model with successively finer and finer meshes, comparing and analyzing the results between these different meshes. During this process, the results are analyzed on some interest points and important domains and boundary's then to judge the convergence of the obtained solution is accepted or not.

There are two techniques that are widely used in the mesh refinements, first is reducing the element size, and second is increasing the element order. Reducing the element size is the primary and easiest refinement technique, that is to decrease the element size through the overall domain. However, because there is no preferential element size in a model, so it is hard to find where to start. So, it need a rough quick check of the modelling first. Increasing the element order is based on the same element size, only increasing the element orders. This can increase the accuracy of the computation, however, it would highly time consuming and easily bring the disturbance to the convergence. So, it is highly recommended to combine these two techniques together to do the refinements. Doing calculation, considering the limited computational resources and time, we can only get an approximation of the real solution. Minimizing the difference "error" between the exact solution and approximated solution, and to ensure that the error is below the accepted tolerance level is the ultimate goal. There are four different types of elements that can be used to mesh geometry in COMSOL for the 3D models, as shown in Figure 4-10 [4.7]. The grey circles represent the nodes of the elements. For 2D modelling, triangular and quadrilateral elements are preferred.

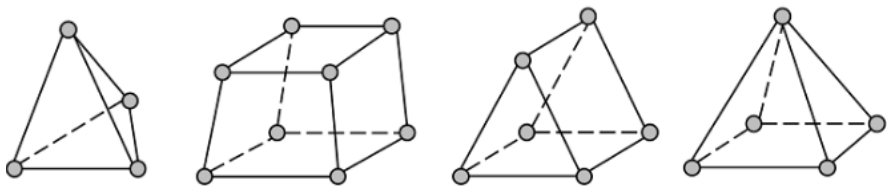

(a) *Tetrahedra* *(b) hexahedra* *(c) triangular prismatic* *(d) pyramid*

Figure 4-10 Four classic types of elements used in mesh system.

4.3.2 Mesh Sensitivity Study

In this section, only the electric field equations are solved in the selective domain to do the mesh refinement study and investigate the computational accuracy, as shown in Figure 4-11.

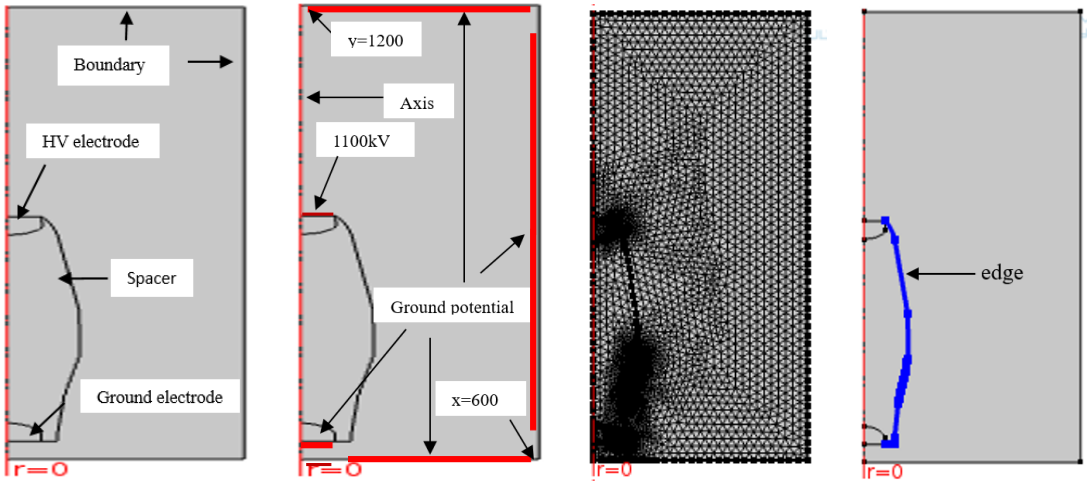

(a) *(b)* *(c)* *(d)*

Figure 4-11 (a) Two-dimensional model of the spacer, (b) boundary condition settings of the model, (c) configuration of the primary mesh used in the electric field calculation, (d) edge line of the spacer.

As shown above in Figure 4-11, (a) is the basic spacer geometry used in the study, which is a part of the wall bushing system. b) indicates the boundary conditions involve the computational domain, the applied voltage, etc. The computational domain is indicated by the red lines. The radial coordinate, indicated by x, is 600mm, and the axial coordinate, indicated by y, is 1200mm. In terms of the applied voltage, both the surface of the lower electrode and the boundary of the computational domain are grounded, and an 1100kV voltage (dc) is applied to the upper electrode. It can be found that the mesh element size near the area of the interface is relatively smaller than that

of the other areas because of the curvature. c) is the mesh size used in the calculation. d) is the interest interface which we focus on.

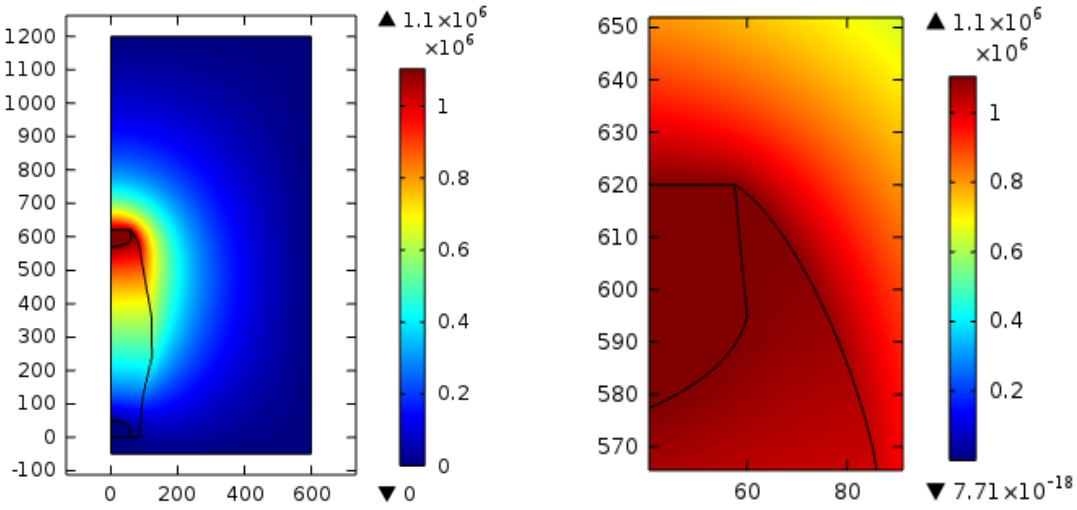

(a) *(b)*

Figure 4-12 Potential distribution of the spacer, a) overview of the potential distribution, b) enlarged view of the triple junction region about the potential distribution.

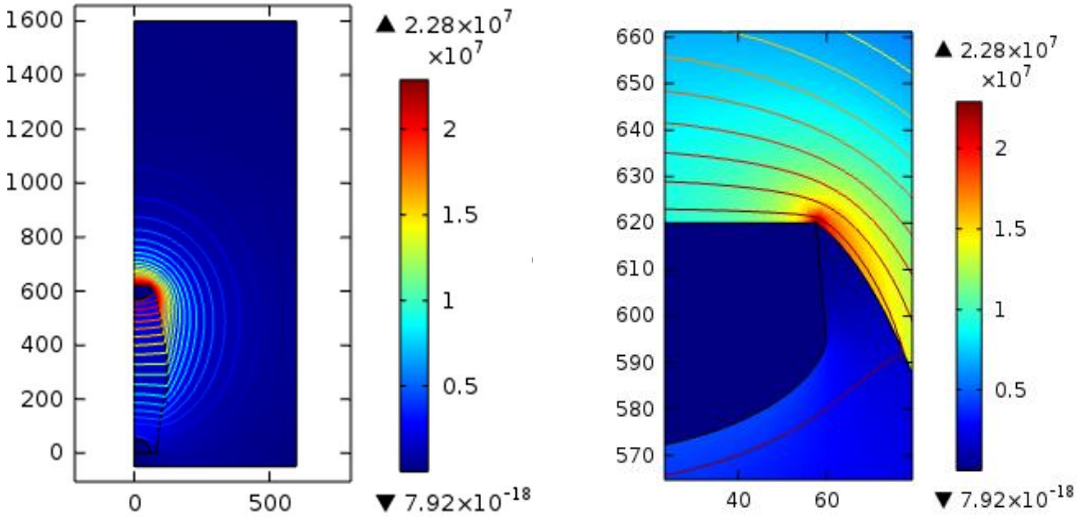

(a) *(b)*

Figure 4-13 Electric field distribution of the spacer a) Overview of the electric field distribution, b) Enlarged view of the electric field distribution

The results from the above case are given above as the electric field and electric potential distribution on the spacer body. Because the high voltage is applied to the upper electrode, the electric potential of the surrounding area is very high, as depicted in Figure 4-12. The potential decreases gradually until zero while approaching the lower electrode and the boundary of the computational domain. By contrast, the distribution of the electric field is completely different from that of the potential. Since the gradient of the potential near the upper electrode is significantly higher than other areas, the maximum electric field intensity near the interface of the upper electrode and the spacer reaches 2.29×10^7V/m. Similarly, the area near the lower electrode also suffers from severe electric field intensity. The electric field intensity of the central part of the spacer, however, is relatively small. As the electric strength along the surface of the spacer is rather lower and it is therefore vulnerable to flashover. The electric field of the edge along the spacer, as indicated in Figure 4-14, should be especially concerned.

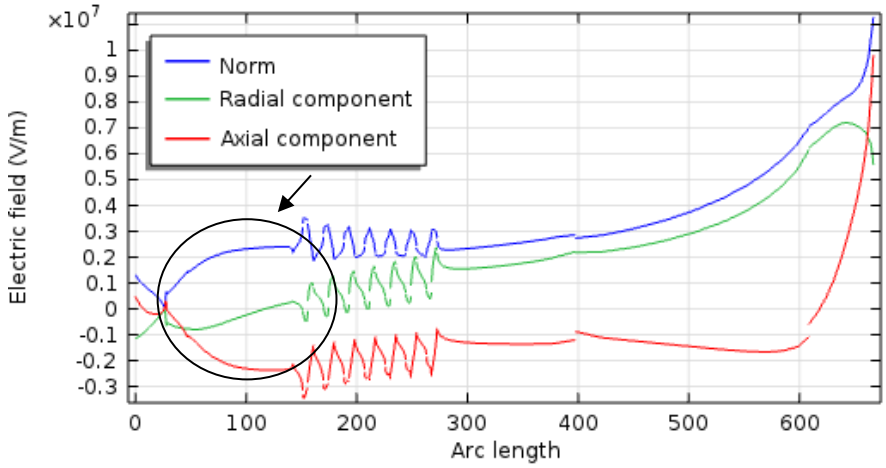

Figure 4-14 Electric field distribution along the edge of the spacer

It can be seen that the electric field intensity along the edge varies drastically. For the upper electrode nearby, the electric field intensity is extremely high, reaching 1.12×10^7 V/m, whereas that of the central part is relatively small, less than 4×10^6 V/m. The area near the lower electrode also suffers from severe electric field intensity, with values

between that of the upper electrode and the central part, as marked in the black circle in Figure 4-14. In order to reduce the maximum electric field intensity along the edge and to make the electric field distribution to be more uniform, the optimization of the structure of the upper electrode as well as the interface between the upper electrode and the spacer requires comprehensive consideration in the design stage. The spacer is operated under dc voltage. As a consequence, the space charges, probably produced by the harmful discharge in the bushing, would be forced to move in the axial direction of the electric field, and thus hugely change the total electric field distribution of the spacer. The calculation of the axial component of the electric field is meaningful and the result is also shown in Figure 4-14. The distribution of axial component, as indicated by the red line, is similar to that of the total electric field, as indicated by the blue line. The maximum value of the axial component is about 9.6×10^{6}V/m, slightly smaller than that of the total electric field. For the area near the lower electrode, however, the axial component is in the inverse direction with the total electric field.

After got overall features of the electric field distribution, we can find that the electric field changes rapidly when it is close to the triple junction region and terrace profiled surface. It can be found that the mesh element size near the area of the interface is relatively smaller than that of the other areas. The influence of the mesh element size is discussed in next section, as shown in Figure 4-15. There are four typical mesh sizes used in the calculation with different parameters.

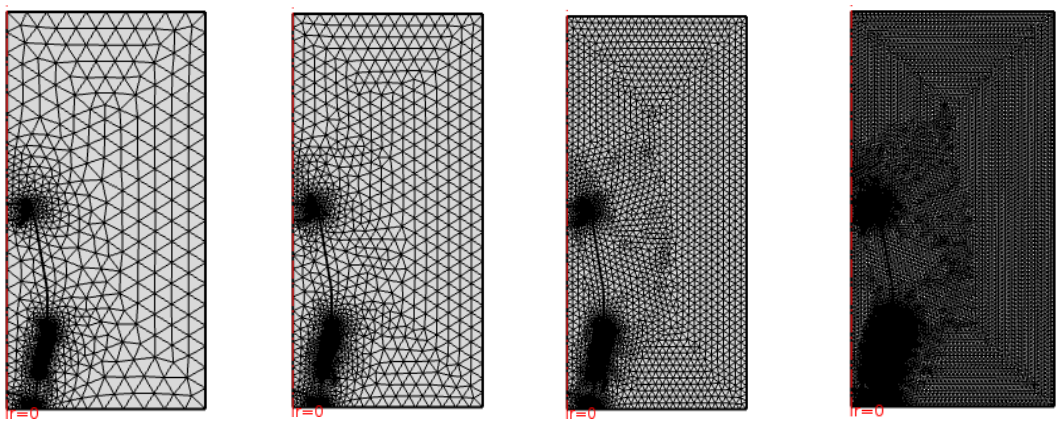

(a) *(b)* *(c)* *(d)*

Figure 4-15 Mesh refinement on the spacer geometry with four mesh densities.

The COMSOL Multiphysics contains nine built-in size parameter sets when meshing, ranging from extremely fine to extremely coarse. Four sets of size parameters, including fine, finer, extra fine and extremely finer, are used here for the comparative study. The parameters of the mesh element are listed in Table 4-1.

Table 4-1 Parameters of the four mesh elements

Case	Maximum element size (mm)	Minimum element size (mm)	Maximum element growth rate	Curvature factor	Resolution of narrow regions
a	63.6	0.36	1.3	0.3	1
b	44.4	0.15	1.25	0.25	1
c	24	0.09	1.2	0.25	1
d	12	0.024	1.1	0.2	1

The definition and function of the parameters are listed as following:

- Maximum element size: To limit the allowed element size.
- Minimum element size: To specify the minimum allowed element size. It can be used to prevent the generation of many elements around small curved parts of the geometry.
- Maximum element growth rate: To determine the maximum rate at which the element size can grow from a region with small elements to a region with larger elements.
- Curvature factor: To determine the size of boundary elements compared to the curvature of the geometric boundary. The curvature radius multiplied by the curvature factor, which must be a positive scalar, gives the maximum allowed element size along the boundary. A smaller curvature factor gives a finer mesh along curved boundaries.

- Resolution of narrow regions: To control the number of layers of elements that are created in narrow regions (approximately). A higher value gives a finer mesh in narrow regions. If the value of this parameter is less than one, the mesh generator might create elements that are anisotropic in size in narrow regions.

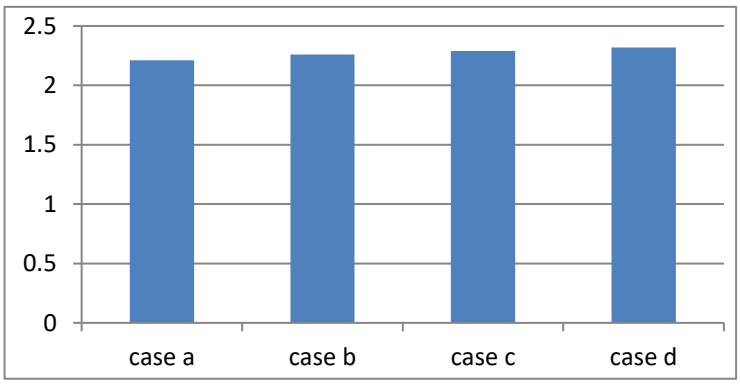

Figure 4-16 Influence of mesh element size on the maximum electric field intensity

The resulting maximum electric field intensity of the spacer is shown in Figure 4-16. The case a, b, c,l and d correspond to the build-in mesh sets of extremely fine, extra fine, finer, fine, respectively. As shown in Figure 4-16, the maximum electric field intensity of the four cases are 2.21×10^7 V/m, 2.26×10^7 V/m, 2.29×10^7 V/m, 2.32×10^7 V/m, respectively. In other words, compared to case a, the maximum electric field intensity has increased by 3.67%, 4.13%, 4.59%. The smaller the mesh element size is, the greater the electric field intensity will be. The difference between the largest electric field intensity, case d, and the smallest electric field intensity, case a, is 0.1×10^7 V/m, which means that the mesh element size of four cases is sufficiently small and meet the requirement of the industrial application. The mesh condition of case C is employed throughout this section.

The electric field distribution of the spacer is also influenced by the boundary conditions of the simulation model, especially the computational domain. As illustrated in Figure 4-13, the red lines indicate the boundary of the computational domain, *x* denoting the axial coordinate and *y* denoting the radial coordinate. The influence of the computational domain on the maximum electric field intensity of the

spacer is investigated in this part. The parameters of the axial coordinate and radial coordinate are listed in Table 4-2 and Table 4-3, respectively.

Table 4-2 Parameters of the axial coordinate

Case	Axial coordinate of the boundary of domain (mm)
a	1000
b	1200
c	1400
d	1600

Table 4-3 Parameters of the radial coordinate

Case	Radial coordinate of the boundary of domain (mm)
a	400
b	600
c	800
d	1000

The influence of the computational domain on the maximum electric field intensity of the spacer is shown in Figure 4-17 and 4-18.

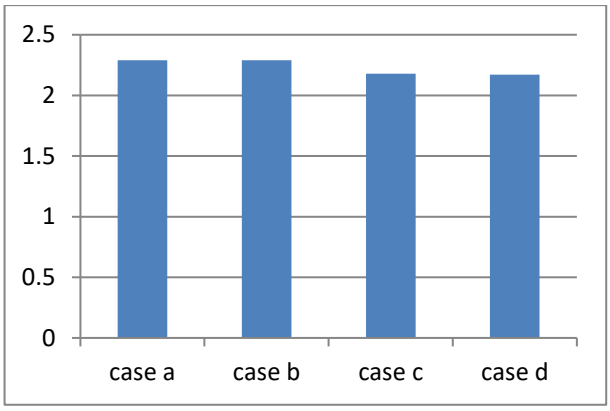

Figure 4-17 Influence of the axial coordinate on the maximum electric field intensity

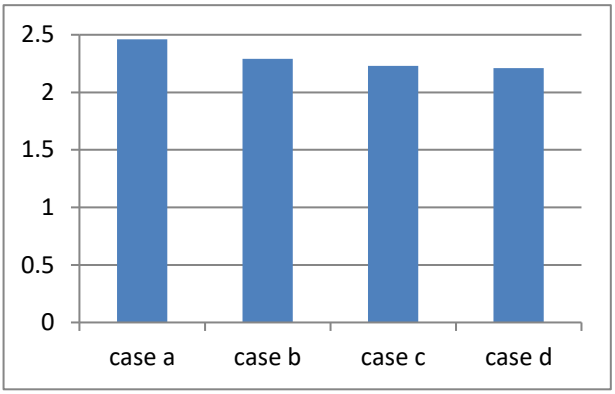

Figure 4-18 Influence of the radial coordinate on the maximum electric field intensity

It can be seen that the larger the axial coordinate of the computational domain is, the smaller the maximum electric field intensity of the spacer will be. When the axial coordinate is 1000mm, the maximum electric field intensity is 2.29×10^{7}V/m. When the axial coordinate is 1600mm, however, the maximum electric field intensity is 2.17×10^{7}V/m. As shown in Figure 4-16, compared to case a, the maximum electric field intensity of case d has decreased by 5.24%. In terms of the radial coordinate, the maximum electric field intensity reaches 2.46×10^{7}V/m when the radial coordinate is 400mm. Compared to case a, the maximum electric field intensity of case d has decreased by 10.16%.

4.4 Implementation of Model in COMSOL

4.4.1 Definition of Equations

The model was implemented in COMSOL 5.0. Despite its friendly user interface for dealing with multi-physics problems, COMSOL experiences severe convergence difficulties for convection dominated transport problems. A stabilization scheme based on false diffusion has to be employed to obtain a converged solution to the governing equations. COMSOL consists of a group of individual simulation programs called Modules. The advantage of COMSOL is that its overall structure allows the coupling of different simulation programs, thus enabling the mutual influences between different physical processes fully coupled and considered.

In the present work, the charge transport equations in Chapter 3, Equations (3.17) and (3.18), in the gas are defined through the Coefficient Form PDE interface, the only choice following an extensive study of the functionalities of each module. In this interface, the default equation is in the following format:

$$e_a \frac{\partial^2 NP}{\partial t} + d_a \frac{\partial NP}{\partial t} + \nabla \cdot (-c\nabla NP - \alpha NP + \gamma) + \beta \cdot \nabla NP + aNP = f \tag{4.1}$$

where NP is a user defined variable representing the number density of positive ions. The meaning of all other variables can be found in the COMSOL user manual [8]. For the present steady state case, the following settings need to be made:

$$\cancel{e_a \frac{\partial^2 NP}{\partial t}} + \cancel{d_a \frac{\partial NP}{\partial t}} + \nabla \cdot (-c\nabla NP - \alpha NP \cancel{+ \gamma}) \cancel{+ \beta \cdot \nabla NP} + aNP = f_{NP} \tag{4.2}$$

$$\cancel{e_a \frac{\partial^2 NN}{\partial t}} + \cancel{d_a \frac{\partial NN}{\partial t}} + \nabla \cdot (-c\nabla NN - \alpha NN \cancel{+ \gamma}) \cancel{+ \beta \cdot \nabla NN} + aNN = f_{NN} \tag{4.3}$$

where NN is a user defined variable representing the number density of negative ions. The coefficients are defined in Table 4-4 for the present work. It must be noted that using the Coefficient Form PDE interface, COMSOL expresses the divergence and gradient operators mathematically based on Cartesian coordinate system. This means for cylindrical polar coordinate system; some terms are missing. Thus, the user has to compensate for any curvilinear coordinate system that is used. The cylindrical polar coordinate system is chosen in the simulation and two compensating terms need to be added as source terms. We have chosen the cylindrical polar coordinate system and we

need to add two compensating terms as source terms, as given in Table 4-4. Test simulation has shown that without these terms the results will not be correct.

Table 4-4 COMSOL implementation settings for charge transport equations

Terms	c	α (alpha)	a	f_{NP}
Positive ion (NP)	D^+	$b^+ \cdot \nabla\varphi$	$K_r \cdot n^-$	$S_{IP} + (D^+ \frac{\partial n^+}{\partial r} + n^+ b^+ \frac{\partial \varphi}{\partial r})/r$
Negative ions (NN)	D^-	$-b^- \cdot \nabla\varphi$	$K_r \cdot n^+$	$S_{IP} + (D^- \frac{\partial n^-}{\partial r} - n^- b^- \frac{\partial \varphi}{\partial r})/r$

The Electrostatics Module is used to obtain the solution for Equation (3.20). Its domain of application is the gas part of the problem under study. Equation (3.20) is coupled to Equations (3.17) and (3.18) through the space charge term in Equation (3.20) and the electric field terms appearing in Equations (3.17) and (3.18). The two charge transport equations in the gas are given their own boundary conditions, as shown in Table 4-5. They are linked to the surface layer or the solid domain through current density on the interface. Equation (3.7) is solved by the Electric Currents Module. The electrical conductivity needs to be provided.

The implementation of the surface layer is a critical part in the work. It is represented by a zero-thickness surface with its surface conductivity given by $\Delta r\sigma_{vs}$ which has a unit of Ω^{-1}. In fact, this surface layer is also axisymmetric, therefore the solution is obtained along a curve, i.e. the curved surface profile line as shown in Figure 4-11(d). This is realized by including the factor $2\pi r$ in the fluxes on both sides of Equation (3.23). Equation (3.23) is defined in the Coefficient Form Boundary PDE Module. The COMSOL default equation is in the form

$$e_a\frac{\partial^2 VL}{\partial t^2} + d_a\frac{\partial VL}{\partial t} + \nabla \cdot (-c\nabla VL - \alpha VL + \gamma) + \beta \cdot \nabla VL + aVL = f \tag{4.4}$$

where the user defined variable *VL* represents the potential along the surface layer and coefficient *c* should be given a value of $2\pi r\Delta r\sigma_{vs}$. The source term *f* in Equation (4.4)

corresponds to the right-hand side of Equation (3.23). Care has however to be taken in producing correct COMSOL command codes to implement the source terms and the unit normal vector of the boundary faces of different computational domains.

4.4.2 Boundary Condition and Interface Condition

The case under consideration is steady state and the applied DC voltage is up to 1100 kV. Because of the high electrical conductivity of the copper material and low leakage current through the insulator, the potential drop in the electrode is negligibly small. The potential equation is therefore not solved in the electrode part. In the computation, the surface of the electrode is fixed at the given voltage such as 1100 kV or at earth potential (earthed electrode and metallic bushing wall). All boundary and interface conditions are summarized in Table 4-5.

It has to be noted that the role of the surface layer critically depends on its electrical conductivity and its thickness. The use of the interface conditions $\varphi_g = \varphi_l$ and $\varphi_s = \varphi_l$ is based on the assumption that a meaningful and converged solution to Equation (3.23) can be obtained. If the surface conductivity integrated over the circumference, which is equal to $2\pi r \Delta r \sigma_{vs}$ is too low, a converged solution to Equation (3.23) will not be achieved and the computation will diverge. This is equivalent to the situation that the potential in the surface layer is undetermined. In such a case, the surface layer should not be included in the model.

Table 4-5 Details of boundary and interface conditions used in the charge transport model.

Equation	Boundary description	Conditions
Gas, potential, Equation (3.20)	Live electrode surface bounding the gas domain	A potential equal to the given DC voltage in Volt is imposed.
	Earthed metallic wall	A zero potential is imposed.

	On interface with insulator or surface layer	$\varphi_g = \varphi_l$ in the presence of a surface layer; $\varphi_g = \varphi_s$ in the absence of a surface layer.
Gas, positive ion, Equation (3.17)	All solid surfaces (live electrode surface, insulator surface, and earthed metallic wall surface)	Perfect absorber when $\vec{n} \cdot \overrightarrow{E_g} > 0$ (*); perfect rejecter ($n^+ = 0$) when $\vec{n} \cdot \overrightarrow{E_g} < 0$
Gas, negative ion, Equation (3.18)	All solid surfaces (live electrode surface, insulator surface, and earthed metallic wall surface)	Perfect absorber when $\vec{n} \cdot \overrightarrow{E_g} < 0$ (*); perfect rejecter ($n^- = 0$) when $\vec{n} \cdot \overrightarrow{E_g} > 0$
Insulator body, Equation (3.7)	Live electrode surface bounding the insulator domain	A potential equal to the given DC voltage in Volt is imposed.
	Earthed electrode	A zero potential is imposed.
	Interface with surface layer or gas domain	$\varphi_s = \varphi_l$ is imposed in the presence of a surface layer; whereas $-\sigma_{VI}\nabla\varphi_s \cdot \overrightarrow{n_s} = e\left[\boldsymbol{E_g}(n^+b^+ + n^-b^-) - (D^+\nabla n^+ - D^-\nabla n^-)\right] \cdot \overrightarrow{n_s}$ is imposed in the absence of a surface layer. $\overrightarrow{n_s}$ here is the unit normal vector on the solid domain boundary.
Surface layer, Equation (3.23)	Live electrode bounding the top end of the surface layer	A potential equal to the given DC voltage in Volt is imposed.

	Earthed electrode	A zero potential is imposed.
All equations	On symmetric axis	The radial derivative of all solved quantities is zero.

(*) $\vec{n}$ is an outgoing unit normal vector from the boundary face of a domain. For example, for the live electrode surface boundary for the gas domain, the unit normal vector goes out from the gas domain (going into the live electrode). ***Eg*** as a vector is the electric field vector in the gas domain.

4.4.3 Convergence Control

It is well known that the Finite Element Method (FEM) can experience severe convergence difficulties for convection dominated transport phenomena. In the present work, the electric field strength near the conductor can be very high, leading to strong drift of charged particles. As a result, convergence at high applied voltage becomes more difficult. The stiffness of the boundary conditions due to the very nature of the FEM makes convergence of the solution process even more difficult. Therefore, the only way left to promote convergence is the addition of selective false diffusion to the numerical algorithms.

For cases with a simple domain, convergence can be improved by the use of refined meshes. This approach however cannot be adopted for large domains with strong local electric field. A domain as shown in Figure 4-19 has been used for the study of convergence control because analytic solution is available for comparison. In view of the fact that stronger false diffusion is needed at locations where drift is stronger and diffusion is weak, it is natural to relate the false diffusion coefficient to the local gradient of the charged number densities. The total diffusion coefficient is thus

$$\mathrm{D} = \mathrm{D}_o\left(1 + \frac{L\left|\frac{\partial n}{\partial r}\right|}{n_0 + 0.1n}\right) \tag{4.5}$$

where D_o is the true diffusion coefficient, n_0 the equilibrium charge number density in the gas which is chosen as the reference value, and L is a length scale. Equation (4.5) means that once oscillation in charge number density is initiated during the solution

process the gradient of the charge number density will be much higher than the true value and strong false diffusion will operate to suppress the instability. Once the solution is converged, the false diffusion will decrease. A typical set of results are given in Figure 4-19 and Figure 4-20 where no physical diffusion is included and no generation of ions is considered. The ions come into the domain from one of the radial boundaries. So only strong convection in the form of drift operates. It can be seen that the scheme works on a very coarse mesh system with a typical mesh size of 5 mm at the middle of the domain. The obtained solution of the number density of the ions agrees very well (within 5%) with the solution with an extremely fine mesh and without the use of false diffusion coefficient.

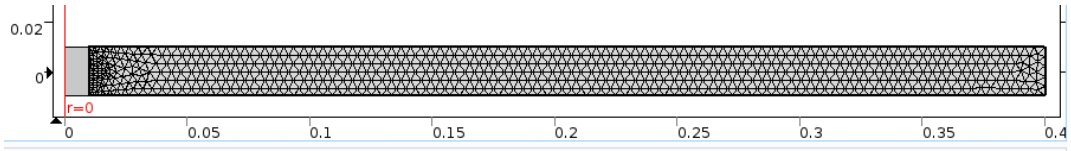

(a)Mesh system

(b)Positive ion number density

(c)Negative ion number density

Figure 4-19 Effect of false diffusion coefficient on the solution of charge transport equations. Despite the large mesh size, the computation based on Equation (3.17) and (3.18) converges and the difference is less than 5% in comparison with the result of a much dense mesh system, L = 1cm.

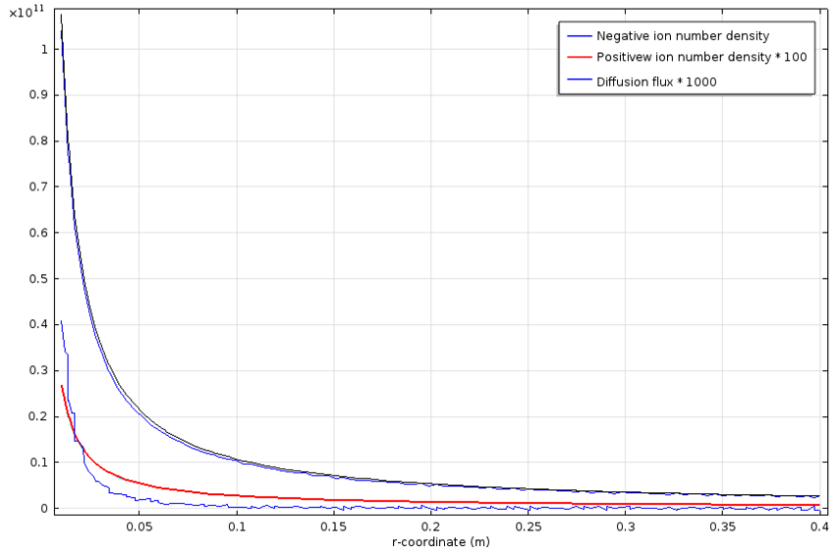

Figure 4-20 Results using the false diffusion technique to promote convergence of the computation. The two lines for each of the positive and negative ions are obtained from a dense mesh system and a coarse mesh system (as given in the top diagram of this figure).

The second practical scheme is to relate the false diffusion coefficient to a drift flux calculated from a set of typical parameters, not relating to the local values of the ion number density. The relationship is

$$\mathrm{D} = \mathrm{D}_o(1 + \theta h|bE_T|) \tag{4.6}$$

where θ is a percentage value, b the mobility of the ions and h the typical mesh size at locations where the gradient of charged particle number density is high. E_T is a typical electric field strength. This scheme applies a uniform false diffusion coefficient over the whole domain and works better for cases with complex distribution pattern of the ions. h = 0.005 m and θ=0.01 is chosen in the present work. E_T needs to be chosen based on the distribution of the electric field in the domain. It has been found that E_T = 1.0×10^5 V/m is a suitable value for an applied voltage of 2 kV. A linear increase of its value with the applied voltage ensures good convergence of the computation.

The effect of introducing this false diffusion coefficient is checked in Figure 4-21 for the case of 800 kV with the geometry given in Figure 4-8. Other details of the simulation will be given in the Results section. As can be seen, the addition of false

diffusion to the solution process only results in a negligible percentage (2%) of diffusive current in comparison with the negative ion drift current. This diffusive current has an oscillatory nature. The false diffusion leads to a slightly higher percentage difference (6%) to the current of the positive ions. However, the total current is controlled by the negative ions and the introduction of the false diffusion coefficient based on Equation (4.6) ensures the convergence of the computation yet without affecting the final results in a substantial way. This validates the approaches that are used in the present work.

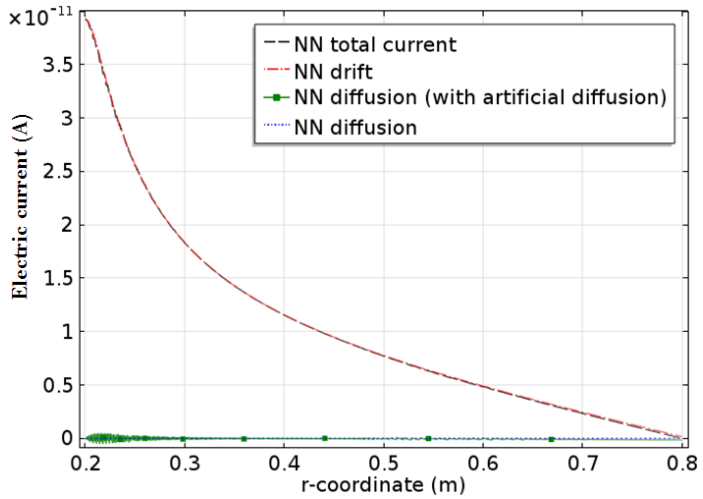

(a)

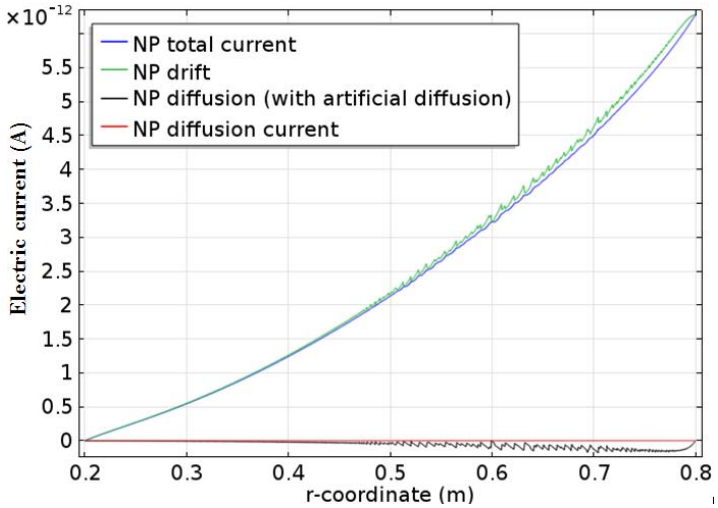

(b)

Figure 4-21 The effects of adding false diffusion in the computation to promote convergence of the solution process. Results are plotted along line AB in Figure 4-8.

4.5 Summary

In this section, the modelling implementation and mesh refinement are demonstrated and investigated. The basic features and core technology of the FEM are introduced. Four typical cases are studied in terms of the influence of mesh size. Convergence control algorithms for drift (convection) dominated transport phenomena are developed to stabilize the oscillations and promote the computational convergence. Results are analysed in detail, especially the influence of added artificial diffusion in the final results. It has been quantitatively shown that the control scheme significantly improves the convergence of the computation yet with little contribution to the flux of the charged particles, thus not affecting the distribution of the charged particles in space. The addition of a surface layer in the model and the derivation of the coupling conditions, interface conditions and its influenced are investigated. The physical mechanism of the charge's movement and accumulation process and its influence has been studied in-depth.

4.6 Reference

[4.1] G.P. Nikishkov, "*Introduction to the Finite Element Method*," University of Aizu, Japan, 2007.

[4.2] B. Evgeny, "*Introduction to the Finite Element Method*," Riga Technical University, 2001.

[4.3] Bathe, K. Jürgen and L. Edward, "*Numerical Methods in Finite Element Analysis*," Englewood Cliffs, NJ: Prentice-Hall, 1976.

[4.4] M. Leonard and K. K. Moon, "Convergence of the classical rayleigh-ritz method and the finite element method," in *29th Structures, Structural Dynamics and Materials of Conf.*, Williamsburg, 1989, pp.509-515.

[4.5] R. Courant, "Variational methods for the solution of problems of equilibrium and vibrations," *Bulletin of the American Mathematical Society*, vol. 49, pp.1-23, 1943.

[4.6] R. W. Clough, "Finite element analysis of axi-symmetric solids," *Journal of the*

Engineering Mechanics Division, vol. 23, no.91, pp. 345-378, 1965.

[4.7] *Finite Element Mesh Refinement*. Available: https://www.comsol.com/multiphysics/mesh-refinement

[4.8] Multiphysics COMSOL, "*Reference Manual for Version 4.4*", pp. 162-168, 2013.

CHAPTER 5 COMPUTATIONAL STUDY OF THE STEADY STATE INSULATION BEHAVIOUR OF AN EPOXY SPACER USED IN HVDC BUSHING

Following the development of the charge transport model and its implementation in COMSOL ensuring computational convergence, the results predicted by the model are first verified in this chapter. The model is then used to study the charge accumulation process on an epoxy spacer used in an HVDC wall bushing for use on 1100 kV systems.

The focus of the present work is on the behavior of the insulator (spacer) considering its immediate environment because the wall bushing has a complex structure and it is not possible to consider all the structural details. Before a study on the simplified arrangement is carried out, there is a need to have some general knowledge on the electric field within a broader environment around the insulator to guide the simplification of the geometry. Therefore, in Section 1 the three-dimensional electric field distribution around the insulator is calculated in a simplified approach, i.e. using a fixed electrical conductivity in the gas domain. The charge transport model needs also to be verified by experimental results before it is used on the insulator in the wall bushing. This is given in Section 2. Section 3 is devoted to a computational analysis of the electric field distribution considering the effect of charge accumulation. The time dependent computational case analysis is provided in Section 4. Finally, a summary of the work in this chapter is given in Section 5.

5.1 Three-Dimensional Calculation of the Electric Field Distribution around the Spacer

5.1.1 Mesh System and Boundary Conditions

Equation (3.9) is used in both gaseous and solid insulator domain with the corresponding electrical conductivity. The conductivity of the epoxy material is 1.6×10^{-16} S/m and that of the gas is 3×10^{-16} S/m (manufacturer supplied value).

Tetrahedral mesh is employed to fit the geometry. In order to ensure acceptable spatial resolution in the results, fine meshes are used in regions where electric potential varies rapidly. using the tools provided by COMSOL, the mesh size is controlled by a set of parameters as listed in Table 5-1 below. Element size, which is a COMSOL defined variable, is the longest side of a tetrahedral element. Element growth rate is used to control the growth in element size of adjacent meshes, representing the ratio of mesh size of two adjacent elements. Curvature factor determines the size of boundary elements compared to the curvature of the geometric boundary. Resolution is used to control the number of layers of elements are created in narrow regions approximately.

Table 5-1 Parameters that are used in the computation to control the mesh size.

Maximum element size (mm)	Minimum element size (mm)	Maximum element growth rate	Curvature factor (mm)	Resolution of narrow region
133	5.71	1.35	0.3	0.85

The mesh system in different parts of the domain is shown in Figure 5-1. In this section, our attention is on the distribution of electric field in the central part of the bushing where the spacer is situated. Given the length of this central barrel, it is acceptable to consider only the space enclosed by the metallic barrel which is 3 m long. The inner diameter of this barrel is 1.35 m. Because the distance from the insulator surface to the shielding tube (Figure 4-3 and Figure 4-4) is longer than the distance from the spacer surface to the inner surface of the metallic barrel, it is reasonable to only consider the components shown in Figure 5-1.

The largest mesh size is by the wall of the barrel where the potential varies slowly, see Figure 5-1(a). A size of 133 mm is found sufficient. Further reducing the mesh size in this region does not significantly change the potential distribution. Moving towards the central conductor, the mesh size gradually reduces. It can be seen in Figures 5-1 (b) and 5-1(c) that the mesh size is smallest at the edge of the metallic components

where the electric field strength is expected to be strong.

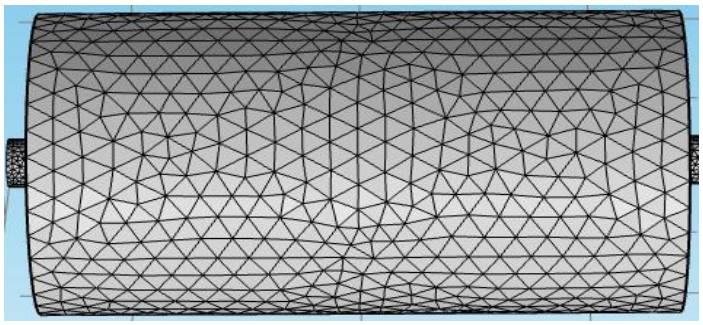

(a) External view of the central part of the bushing

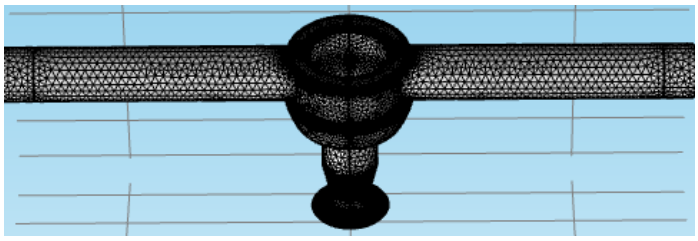

(b) Internal view of the central part of the bushing

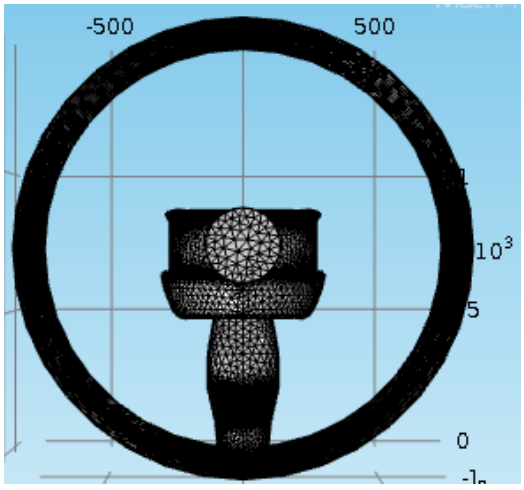

(c) Cross sectional view of the bushing

Figure 5-1 Overall configuration of the mesh in the 3D modelling work.

The boundary conditions need to be set. As shown in Figure 5-2(a), the central

conductor including the metallic connector that joins the conductor with the top of the spacer is set to a voltage of 1100 kV. The bottom of the spacer is set to ground potential. The surface of the metallic barrel is also set to ground potential (Figure 5-2(b)). At the two ends of the domain, the potential gradient in the longitudinal direction is set to zero to ensure that the potential changes from ground level on the barrel surface to the set high voltage at the conductor surface. This completes the boundary conditions.

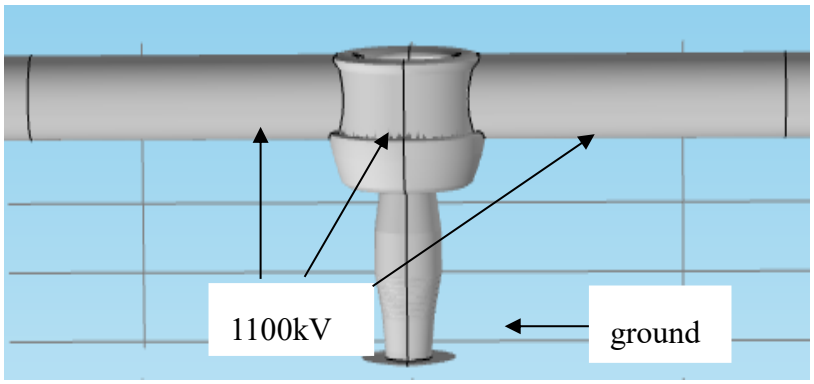

(a) Internal view of the boundary conditions

(b) External view of the central part of the bushing

Figure 5-2 Boundary condition settings. The high voltage of 1100kV (DC) is applied to the central conduct, and the out shell of the spacer as well as the housing is grounded.

5.1.2 Results and Analysis

The electric potential and electric field distribution in the plane cutting through the axis of the spacer but is aligned perpendicular to the axis of the central conductor is

shown in Figure 5-3. It is apparent that more than 50% of the potential drop in the gas domain is within a region with a typical thickness of 200 mm. In the epoxy spacer, the potential drop is within an even smaller thickness due to the difference in electrical conductivity (Figure 5-3(a)). Strong electric field occurs at the top edge and the bottom edge of the bowl-shaped connector, as expected. The maximum value reaches 1.9×10^7 V/m, equivalent to 190 kV/cm. The breakdown field strength of SF_6 at 6 bar is close to 350 kV/cm, which is well above the maximum electric field. This is consistent with the design principle. It is worth pointing out that the strong electric field at the bottom of the connector, especially near the upper part of the spacer may affect the local electric field distribution when charge transport is considered in Section 3, which will be discussed in more details.

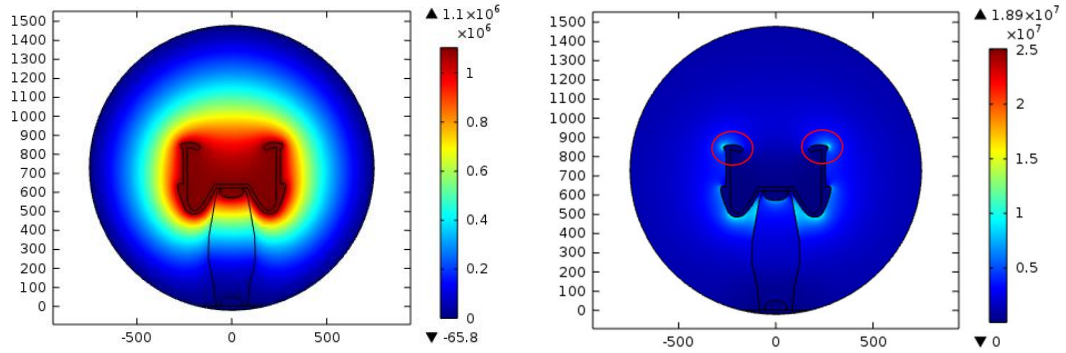

(a) *(b)*

Figure 5-3 (a) electric potential distribution and (b) electrical field distribution in the spacer.

The electric field distribution in the epoxy spacer is shown in color contour in Figure 5-4. It is apparent that strong electric field is induced near the top contact with a maximum value of 7.2×10^7 V/m, which is controlled by the shape of the contact tip and the size change of the epoxy spacer. It reduces gradually towards the bottom.

The electric filed strength along the surface of the spacer is given in Figure 5-5. The maximum electric field intensity along the edge is 5.51×10^6 V/m, which takes place near the upper part of the spacer (5-5(a)). Moving downwards the electric field decreases. Local electric field enhancement is observed along the surface where

corrugation (ridges and furrows following each other) is used to increase the creepage.

The potential and electric field distribution in a plane cutting through the axis of the spacer and the axis of the central conductor is also checked. Results show that the distribution of both the potential and electric field distribution around the epoxy space is very close to the distribution shown in Figure 5-3. The difference is in the region where the central conductor is. This however does not affect the field around the insulator. Therefore, it is possible to use an axisymmetric domain for the study presented in Section 3.

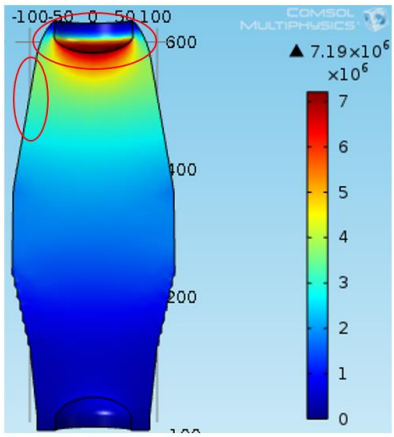

Figure 5-4 Color contour of electric distribution in the epoxy spacer.

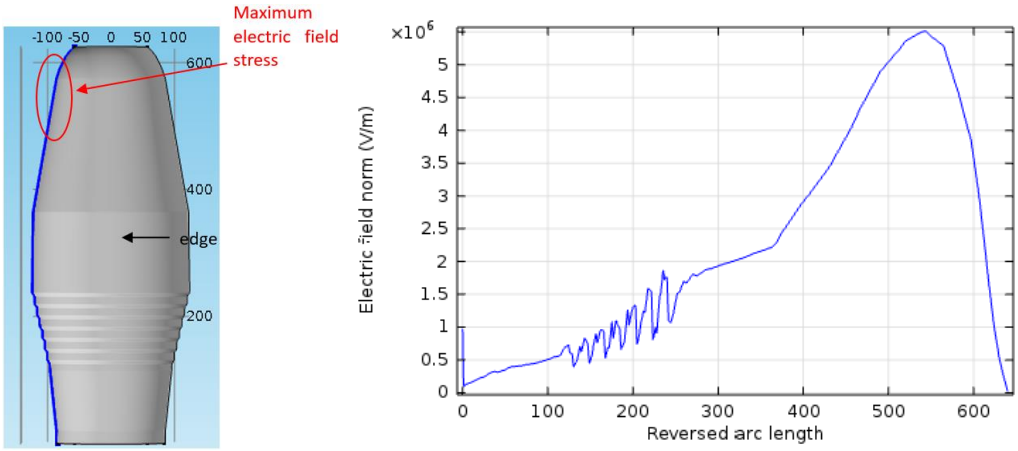

(a) *(b)*

Figure 5-5 (a) the blue line indicates the edge on the insulator surface and (b) electric field intensity along the profile.

5.2 Validation of the Charge Transport Model

Despite the discussions presented in Chapter 3 of the physical mechanisms dominating the charge transport phenomenon under DC stress, there are still uncertainties in the properties of epoxy and gas, especially those involving the generation and transport of charged particles. Therefore, model validation is essential to build confidence in its validity. In this section, two experimental cases involving different gases and voltage levels are modelled and results obtained from the model established in the present work are compared with the experimental results to demonstrate the validity of the model.

5.2.1 Epoxy Insulator in SF_6 at 200 kV

The first experimental case that is modelled is from [5.1] with different insulator shapes. The conditions are the same as those specified for the experiment. In the experiment, they used four types of cylindrical spacers, 4 cm long and 4 cm in diameter, as shown below in Figure 5-6 (a). The insulator samples are made of epoxy resin containing alumina (Al_2O_3) or silica (SiO_2) as filler. The dashed regions represent the embedded electrodes (contacts). The pressure of SF_6 varied between 2-3 bar. No material properties are given in [5.1]. The electrical conductivity of epoxy material, in the absence of information provided by the authors, is given a value of 1.89×10^{-16} S/m for epoxy filled with Al_2O_3 microns [5.2]. This is the best value that can be obtained from literature. The other properties that are needed for the computation are reviewed in Chapter 2. The insulator is placed between two parallel plane electrodes with a diameter of 20 cm. The insulator and the electrodes are placed in a steel vessel, as shown below in Figure 5-6 (b).

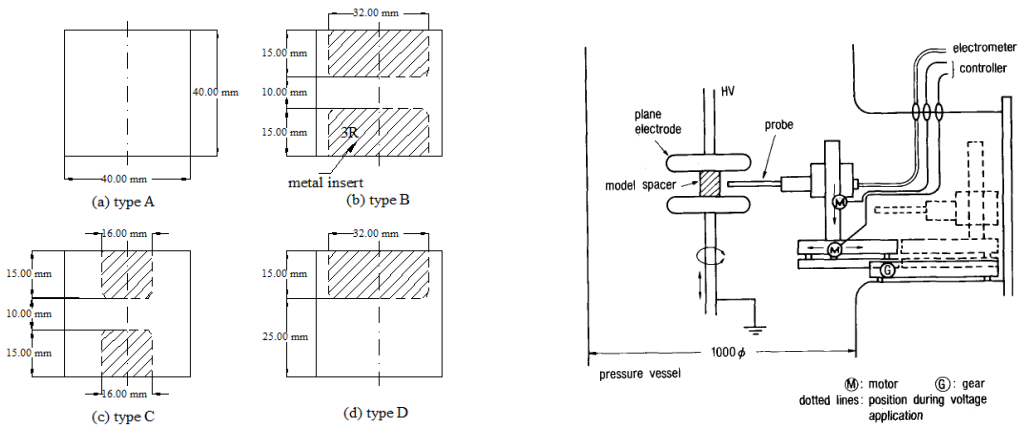

(a) *(b)*

Figure 5-6: (a) Schematic confirgurations of four types of insulators used in the experiment [5.1]. (b) The experimental setup in the vessel.

It is to be noted that the measurement was taken for different application duration of the DC voltage, from 2 to 200 hours. And the surface charge density measurment was performed vertically (along Z- direction, the axial direction, from Z=0 (grounded plane electrode) to Z=4 cm (high voltage electrode). At each axial position, meadurement was also taken in the azimuthal direction with an intervals of 30 degrees. From the experimental results, steady state is approched within two hours from the application of the DC voltage.

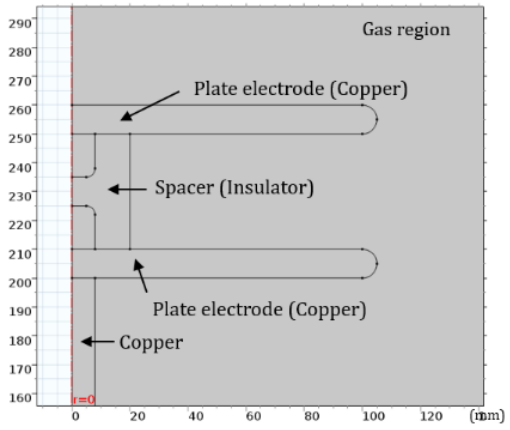

Figure 5-7 Cross sectional view of the computational domain based on the experimental system used in the [5.1].

The two parallel disk electrodes have a thickness of 10 mm. The computational domain is shown in Figure 5-7. The insulator is cylindrical with a radius of 20 mm. The computational domain has a width of 500 mm and is 460 mm long in its axial direction.

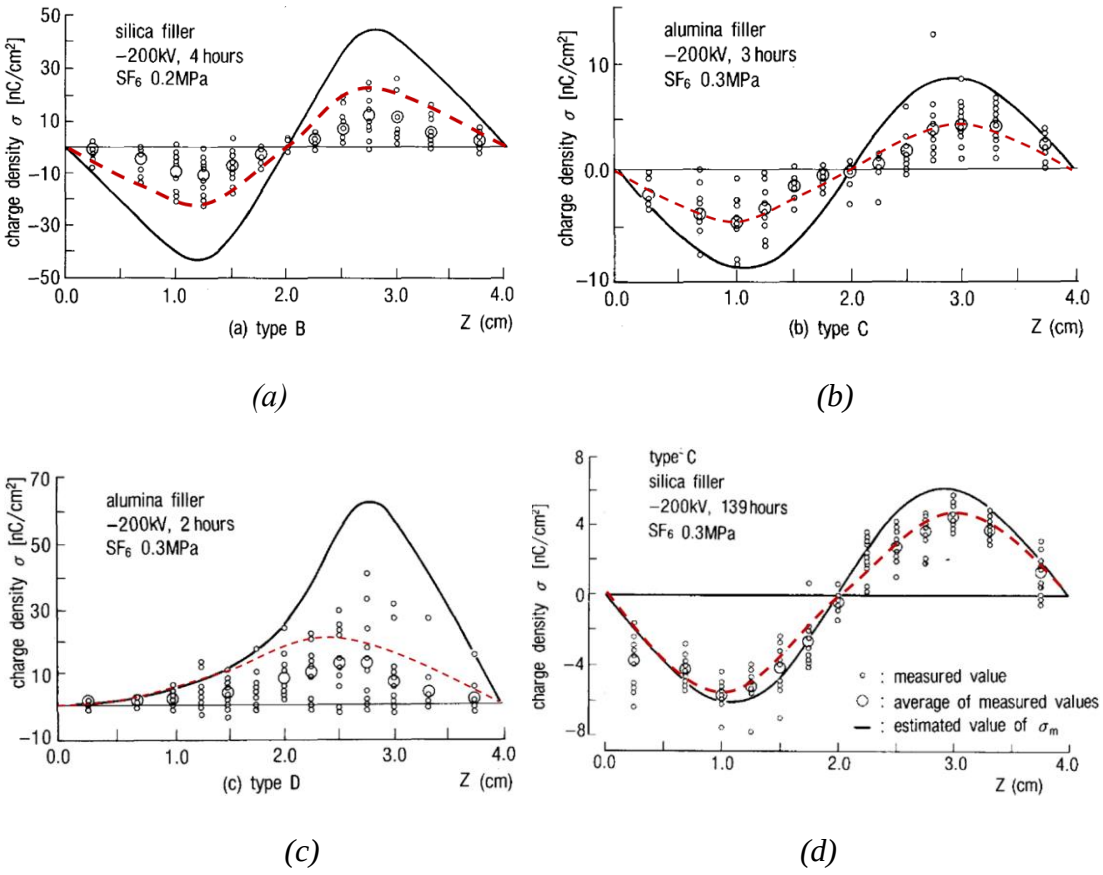

Figure 5-8 Comparisons of measurement and simulated results. Small circles – measured surface charge density in the experiment; large circles – average value of measured charge density; solid curves – from simple model in [5.1]; red dashed curve – present work.

Form the measurement, it is clear that the surface charge is not uniformly distributed along the circumference of the cylinder insulator. It has a large variation. This non-uniformity in the azimuthal direction is observed in most of the measurment and seems to be unavoided in practice. The calculated surface charge density is shown in Figure 5-8 by the red dashed lines. It is fairly close to or slightly larger than the measurements

averaged in the azimuthal direction. Our prediction is reasonable because the experimental system approaches steady state in 2 to 5 hours [5.1]. In addition, the present model leads to much closer results than the simple estimation in [5.1] which is shown by the solid lines in Figure 5-8.

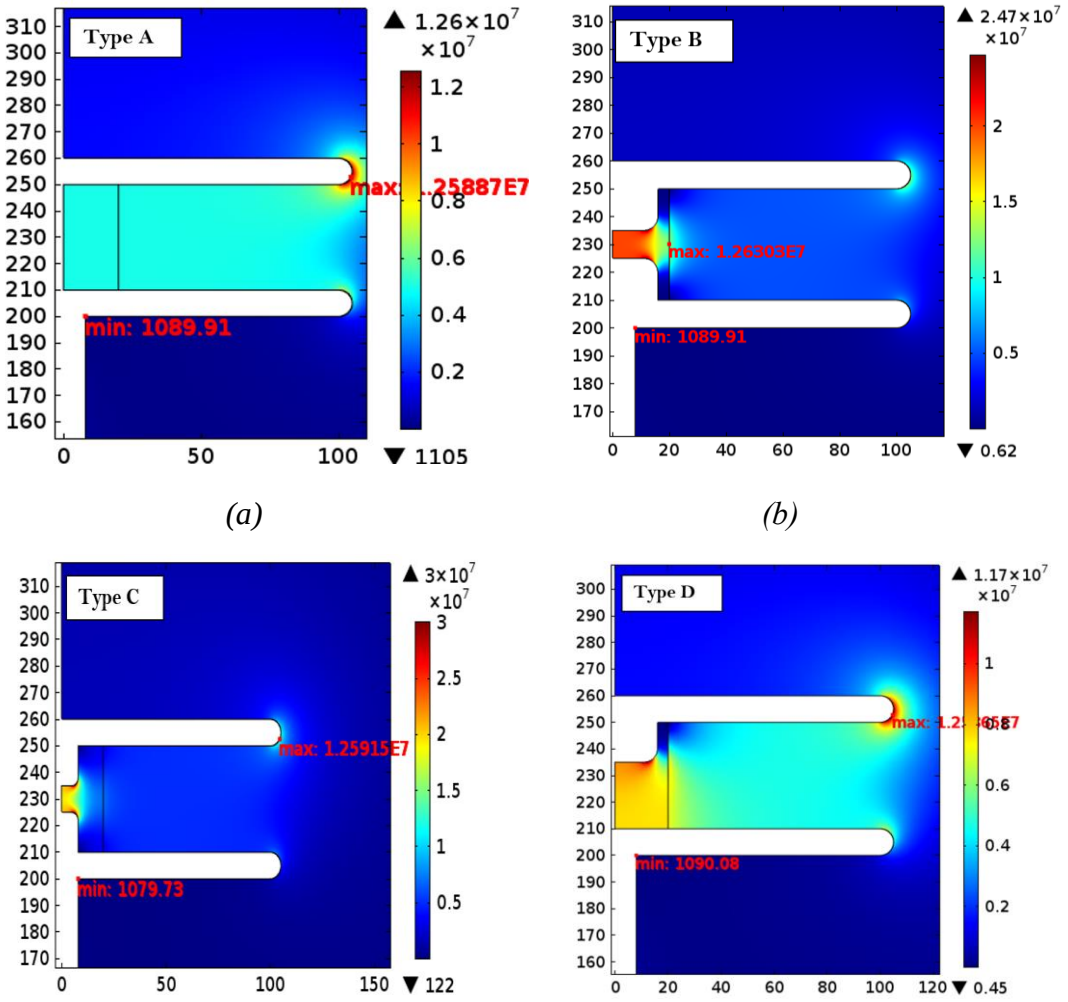

(a) *(b)*

(c) *(d)*

Figure 5-9 Color diagram of electric field distribution obtained using different types of insulator. The applied voltage is -200 kV, the inserted filler is Alumina(Al_2O_3).

Figure 5-9 reveals important relationships between the shape of the insulator and the distribution of the electric field on the interface. As shown in Figure 5-9, changing the

profile of the embedded electrode leads to significant difference in the electric field distribution. Without the embedded electrode into the insulator (case A, i.e. type A), the electric field remains almost constant around 5×10^6 V/m and has only a tangential component along the surface of the insulator. However, with type B, the electric field changes remarkably, especially at the middle part of the insulator where most potential drop takes place. The tangential component along the interface increases to its maximum at the middle point because of the decrease in electrode gap length in comparison with case A. The normal component is however zero at this middle point due to symmetry. When the diameter of the electrode that is embedded in the insulator body is reduced in case C, the radial thickness of the insulation material between the electrode and the surrounding gas increases, which leads to a more uniform tangential component of the electric field along the interface (Shape C in Figures 5-9 and 5-10).

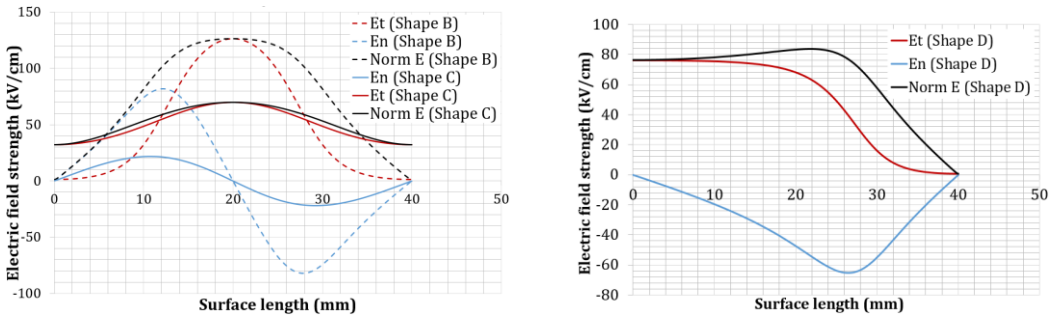

(a) *(b)*

Figure 5-10 Surface electric field distributions of shape B, shape C and shape D. The applied voltage is -200 kV.

As can be seen in Figure 5-10, the normal component of the electric field exhibits negative symmetry about the middle point of the insulator interface in Cases B and C (solid and dotted blue lines in Figure 5-10(a)). The highest field strength is 127 kV/cm for shape B and 70 kV/cm for shape C.

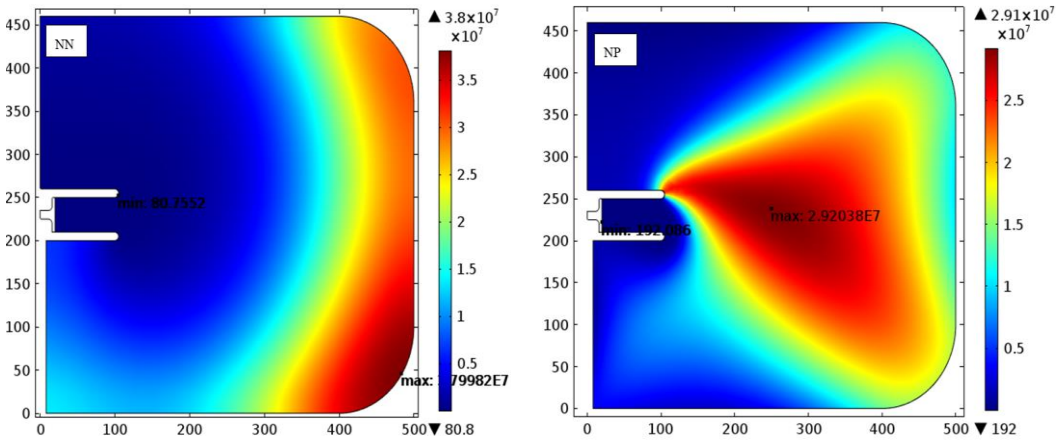

(a) negative ion *(b) positive ion*

Figure 5-11 Positive and negative ion number density in SF_6 gas at an applied DC voltage of - 200 kV of type B.

As shown in Figure 5-11 the application of -200 kV to the top electrode attracts positive ions to move towards its surface (Figure 5-11(b)). Negative charges are expelled towards the earthed boundary, leaving very low number density near the insulator. Due to shielding effect, the upper and lower surfaces of the top electrode (negative polarity) do not attract many positive ions near them because of the lower field strength.

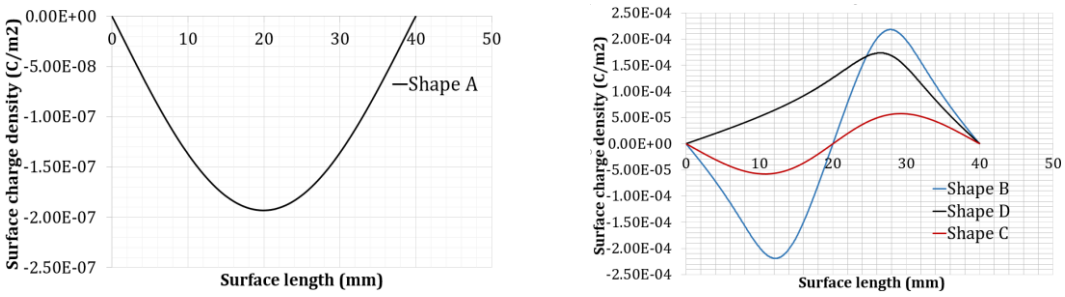

(a) *(b)*

Figure 5-12 The surface charge distributions of four types sample spacers. The applied voltage is -200 kV.

Figure 5-12 shows the variation of the surface charge density for different shapes. Obviously, less charge is accumulated on the surface of shape A because the current

is flowing in the axial direction only inside the insulator and in regions near the interface. With both embedded electrodes, the radial electric field component becomes stronger and more charges accumulated on the interface, as in cases B and C. Insulator type B has more charges accumulated on its surface because of the stronger radial electric field in comparison with case C.

5.2.2 Epoxy Insulator in Air under 15 kV

This case was from Winter and Kindersberger [5.3] with an epoxy insulator placed in a test chamber filled with air at atmospheric pressure, as shown below in Figure 5-13 (a). The insulator has a length of 132 mm and diameter of 80 mm, the embedded aluminum electrodes has a height of 29 mm. The insulator samples are made of two Al_2O_3-filled epoxy resins based materials EP1 and EP2 with similar filler content but different base materials. The insulator is installed between a high voltage electrode and a grounded plate electrode. The high voltage electrode and the insulator are surrounded by a grounded outer screen to create defined field conditions. The computational domain in the present work was constructed based on the geometric information given in [5.3], especially its Figure 1. The material properties used are also identical to those used in their simulation (given in captions of their Figure 9).

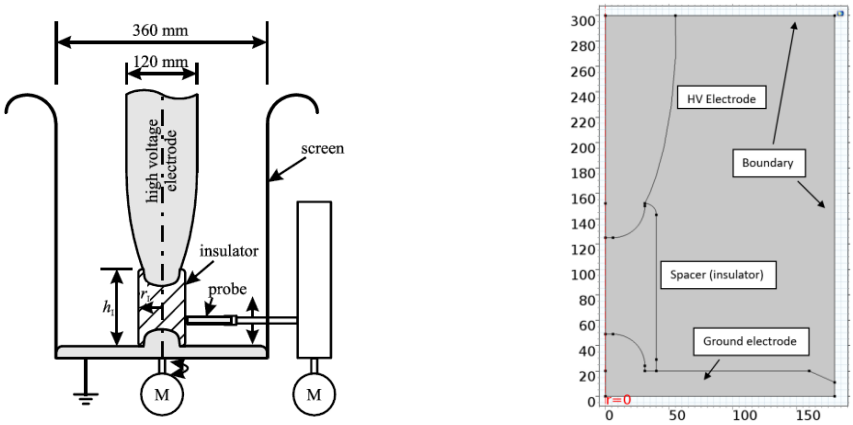

(a) *(b)*

Figure 5-13 (a) Electrode arrangement, cylindrical insulator and probe for the measurement of the surface potential in [5.3]. (b) is the mathematical model based on the experimental system.

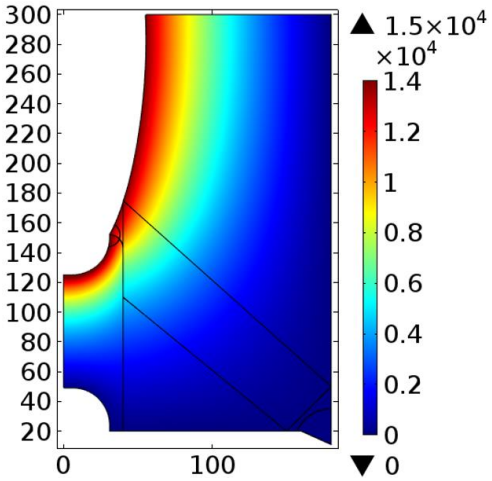

Figure 5-14 Electrical potential distribution under 15 kV.

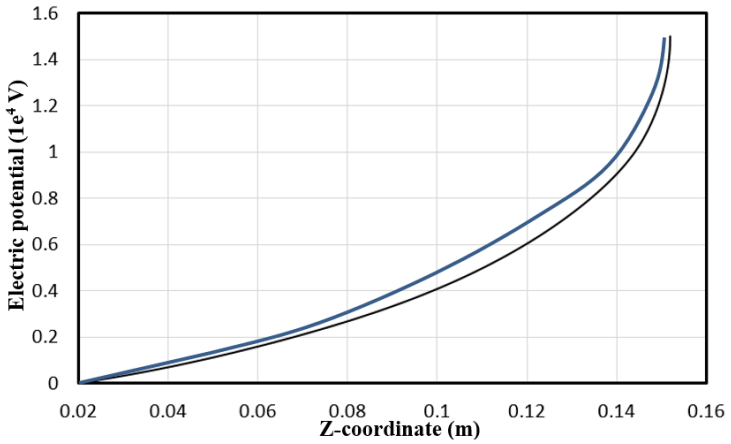

Figure 5-15 Predicted electrostatic potential distribution along insulator surface (black curve) and measured values (time = 8000 hours) given in [5.3] (blue curve).

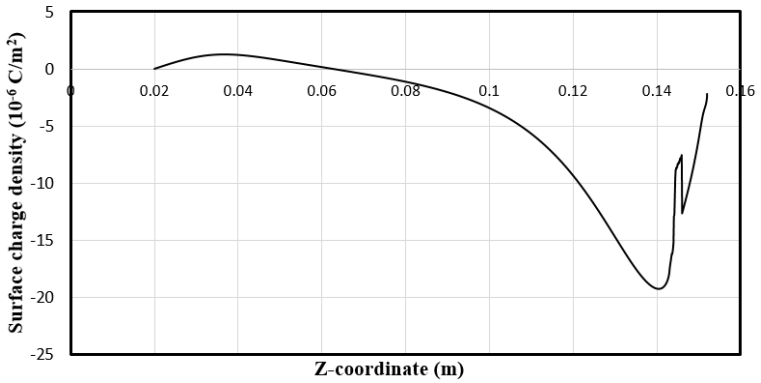

Figure 5-16 Predicted surface charge density along the insulator surface for an applied voltage of 15 kV.

The current density of ions in the model consists of three components, the drift current, the physical diffusive current and the artificial diffusive current. The artificial diffusion coefficient of ions is related to the mobility of the ions and a characteristic field strength [5.4]. This characteristic field strength is increased until the solution is converged. It has been found that the ion current density in gas due to artificial diffusion is only 0.3% of the total current density, thus justifying the use of false diffusion to stabilize the solution process. A comparison of the electric potential along the surface of the insulator are given in Figure 5-14 and Figure 5-15. The predicted distribution from the present work is slightly lower than the measurement. This is reasonable since steady state corresponds to a time of infinity. The predicted peak surface charge number density is 1.92×10^{-5} C/m^2 (Figure 5-16) which compares well with the value of 1.75×10^{-5} C/m^2 given in [3]. The spike in Figure 5-16 at z=0.144 is due to the curvature change at that point.

Despite the very good agreement, our calculated negative ion number density distribution is slightly different from that reported in [5.3], especially the high-density strip shown in Figure 5-17. The strip in our case is slightly wider and joins the electrode surface while in [5.3] it joins the insulator surface, as marked in Figure 5-17.

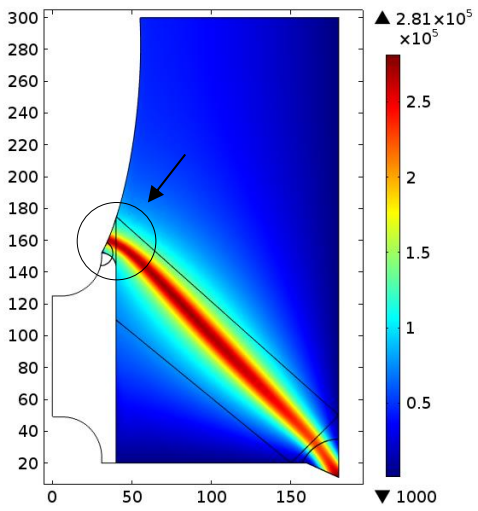

Figure 5-17 Distribution of negative air ions in gas domain with a pressure of 1bar and applied voltage of 15 kV.

5.3 Computational Analysis of the Performance of an 1100 kV Epoxy Spacer

Following the verification of the charge transport model in last section, it is applied to an HVDC epoxy spacer designed for application in wall bushings up to 1100 kV. In the present work, we use two geometries of the central electrode with the simple one shown in Figure 5-18. The simplification is based on the consideration that in the original design the local electric field near the top part of the epoxy spacer is enhanced due to the use of the bowl-shaped connector. This simplification minimized the enhancement effect so it is possible to study the electric field due to charge accumulation. The more complicated geometry will be introduced later when relevant results are discussed.

Unless stated otherwise, all results presented in this section are obtained using an epoxy electrical conductivity of 1.6×10^{-16} S/m (manufacturer supplied value). The spacer itself is axis-symmetric and two electrodes are embedded into it. The maximum diameter and height are 246 mm and 620 mm, respectively. The original design contains a section of the surface with ridge-furrow shaped corrugation to increase the creepage distance. SF_6 gas is at 6 bar absolute. A temperature of 300 K is used in the

present work. The maximum mesh size is 3 mm in regions where electric field is changing slowly in space. A typical mesh size of 0.3 mm is used near the conductor and insulator surfaces to ensure adequate spatial resolution. Further reduction in mesh size leads to negligible change in the solution. Relatively strong relaxation should be used to guarantee convergence of the solution process at very high applied voltages.

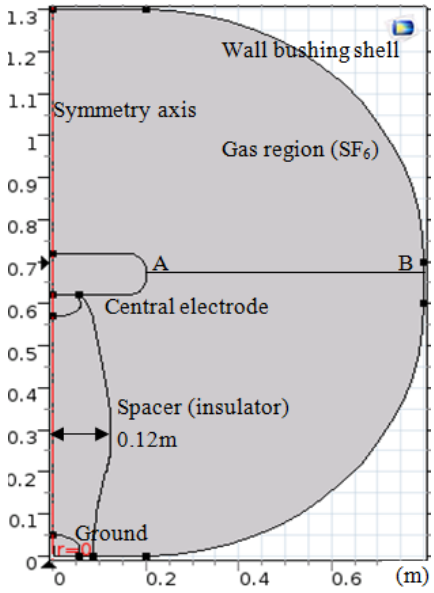

Figure 5-18 Cross sectional view of the simplified insulator system.

5.3.1 Overall Features of the Charge Accumulation Process around the Spacer

Charge accumulation is a consequence of charge movement in the insulation media, whether gas or solid. The flux of charge in the epoxy material is proportional to the local electric field strength since the electrical conductivity is fixed. This is however not the case in gas because the electrical conductivity of gas depends on the charge number density and also the mobility. Unlike in epoxy, charges in gas such as SF_6 are allowed to have very different number density depending on the transport mechanisms. Accumulation of charge occurs when the divergence of the initial charge flux is not zero. At the solid surface, it is the difference in the normal direction charge fluxes in gas and epoxy that leads to the accumulation in the absence of a surface layer. When reaching a steady state, the accumulated charge alters the potential distribution which

adjusts the local normal electric field components in gas and in epoxy to balance the charge fluxes.

The concept of surface layer refers to the situation where the ability of the material near the insulator surface to conduct current is greatly enhanced or very different from the bulk material due to coating, ageing or other surface modification. The thickness of this layer with different behavior is usually small (<0.1 mm). A surface layer with distributive electrical conductivity provides an additional dimension (along the surface) for the balance of electric currents across the gas-solid interface, therefore helping smoothen (minimize) the electric field strength and surface charge density along the insulator surface.

To explain the phenomenon, a simple case with a fixed low electrical conductivity in SF_6 is simulated, shown as Case A in Figure 5-19. This case is used for comparison. The electrical conductivity in SF_6 is set to only 1% of that in epoxy. The applied voltage is 800 kV. As a result, little current can pass the interface due to the relatively low electrical conductivity in SF_6 and the current density in epoxy in the tangential direction of the insulator surface is much larger than that in the normal direction. Local enhancement of electric field is observed where the surface is crest and furrow shaped (Case A in Figure 5-19). Positive charges are accumulated on most of the insulator surface in order to increase the normal electric field component in gas near the surface to increase the normal current density component in the gas (Figure 5-20). The electric potential along the insulator surface is given in Figure 5-21.

In Case B, the electrical conductivity of SF_6 is set to a value that is estimated using the ion number densities obtained from the charge transport model in the present work (5.35×10^{-18} S/m) and the ion mobility. When a smaller value of electrical conductivity for epoxy (3.33×10^{-18} S/m [5.3]) is used, the gas now becomes slightly more conductive than epoxy and as a result the normal electric field component in epoxy has to be enhanced by accumulated negative charges (Case B in Figure 5-20) in an attempt to balance the normal current density from the solid. The field strength near the top of the insulator is significantly enhanced (Case B in Figure 5-19) while on the surface of the lower part of the insulator the field is suppressed. This is linked to the very different potential distribution shown in Figure 5-21, demonstrating the fact that

negative charge accumulation occurs when the gas is more conductive than the solid insulation material.

When the charge transport process is fully considered (Case C), the electric field becomes slightly stronger than Case A. Based on the number density of positive and negative charges and the mobility, we obtain an electrical conductivity of SF_6 in the range from 2.14×10^{-18} S/m to 5.35×10^{-18} S/m. The value at the middle of the insulator surface is 3.0×10^{-18} S/m, which is less than 3% of the epoxy conductivity (1.6×10^{-16} S/m). Therefore, this case is similar to Case A with mainly positive charges accumulated on the surface of the insulator (Case C in Figure 5-20). The potential curve is also similar to Case A as shown in Figure 5-21.

It is therefore very clear that the polarity of the charge accumulated on the insulator surface and modification of the surface potential both depend on the relative magnitude of the effective conductivities of epoxy and gas.

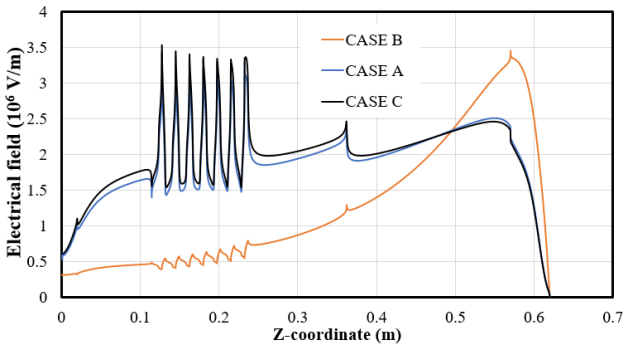

Figure 5-19. Case A (Blue line): 1.6×10^{-16} S/m for epoxy and 1.6×10^{-18} S/m for SF_6; Case B (Yellow line): 3.33×10^{-18} S/m for epoxy and 5.35×10^{-18} S/m for SF_6; Case C (Black line): solution by charge transport model with 1.6×10^{-16} S/m for epoxy.

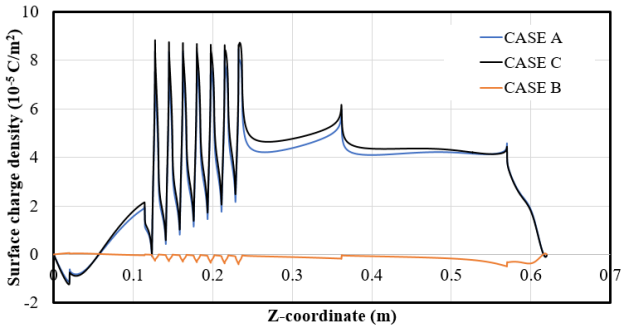

Figure 5-20 Surface charge density along insulator surface. Case A (Blue line): 1.6×10^{-16} S/m for epoxy and 1.6×10^{-18} S/m for SF_6; Case B (Yellow line): 3.33 $\times10^{-18}$ S/m for epoxy and 5.35×10^{-18} S/m for SF_6; Case C (Black line): solution by charge transport model with 1.6×10^{-16} S/m for epoxy;

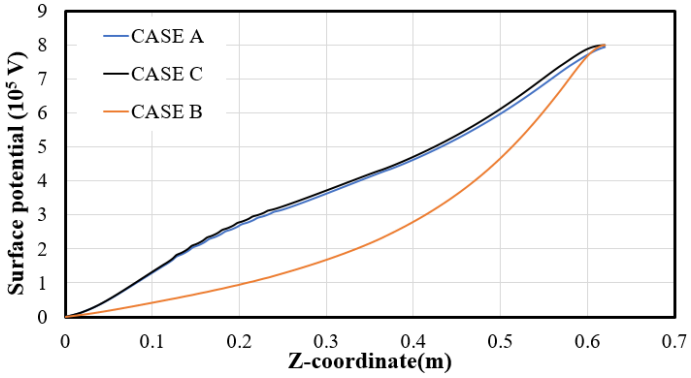

Figure 5-21. Case A (Blue line): 1.6×10^{-16} S/m for epoxy and 1.6×10^{-18} S/m for SF_6; Case B (Yellow line): 3.33 $\times10^{-18}$ S/m for epoxy and 5.35×10^{-18} S/m for SF_6; Case C (Black line): solution by charge transport model with 1.6×10^{-16} S/m for epoxy.

5.3.2 Nonlinearity of the System

In equilibrium state without any applied electric field, the ion pairs number density attains a value of $\sqrt{\frac{S_{IP}}{k_r}}$, which is 1.13×10^{10} m^{-3}. When the ions drift in an applied electric field and with the boundary conditions given in Table 1, the ion number density develops severe non-uniformity in the gas domain, as shown in Figure 5-22. The maximum value is around 3.6×10^{6} m^{-3}, much lower than the equilibrium value.

Positive ions are expelled from the conductor and insulator surface while negative ions are attracted towards the electrode surface. There is a strip of relatively higher negative ion number density as shown by the broken rectangle in Figure 5-22 b). The reduction in ion number density in comparison with the equilibrium value means that without ionization source due to electric discharge near the insulator (corona or partial discharge), the effective electrical conductivity of SF_6 can vary over a few orders of magnitude through the change in ion number density. Thus, we must solve the charge transport equation directly to account for current conduction in the gas, instead of using the concept of electrical conductivity.

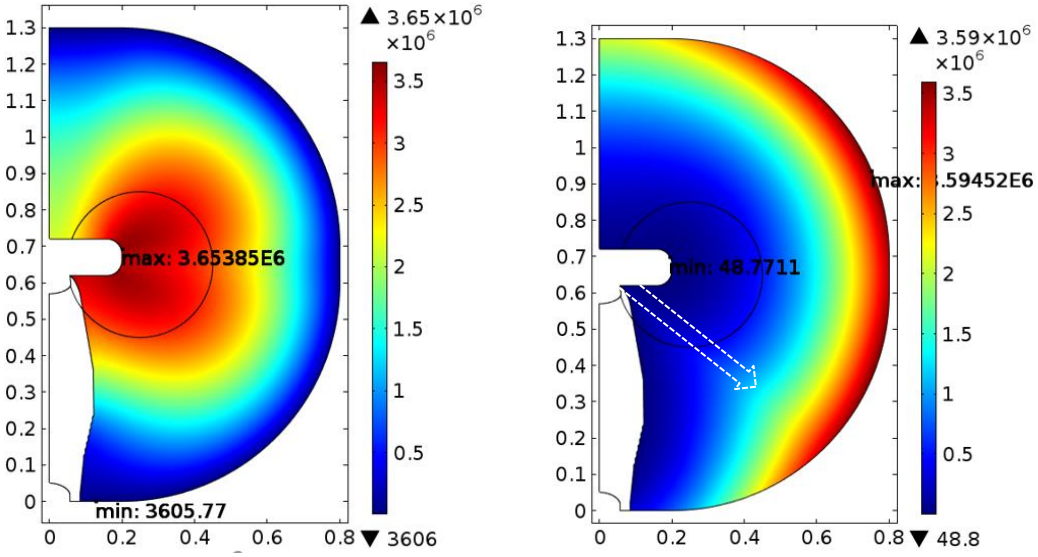

(a) *(b)*

Figure 5-22 Density distribution of positive (a) and negative (b) SF_6 ions in the gas domain at an applied voltage of 800 kV.

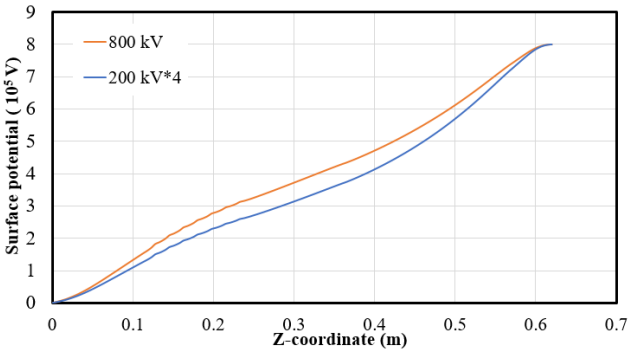

(a)

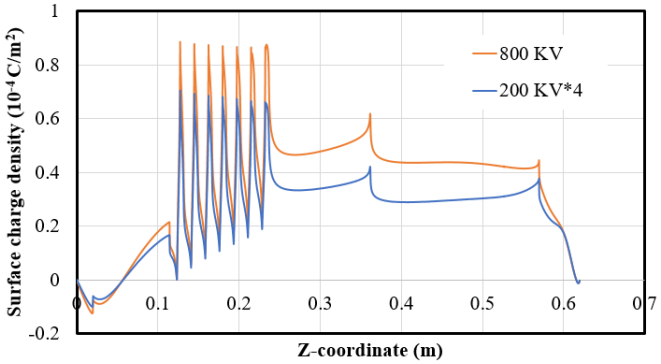

(b)

Figure 5-23 Electric potential distribution (a) and surface charge density (b) along the insulator surface at 200 kV and 800 kV.

Figure 5-23 shows the electric field distribution along the insulator surface at different applied voltages. The difference of the distribution at 200 kV multiplied by a factor of 4 and that at 800 kV represents the nonlinearity of the system. This also applies to the surface charge number density in Figure 5-22 b). Examination of the governing equations indicates that it is the recombination terms that contribute to this nonlinearity.

5.3.3 Influence of Surface Profile of the Magnitude of Accumulated Surface Charge

Under steady state, the normal electric field component on the interface is related to charge accumulation. The field component tangential to the insulator surface is however affected by the total effective conducting cross sectional area normal to the

tangential current component. In the original design, the lower part of the insulator has ridge-furrow shaped corrugation on its surface. Our modelling results (Case C in Figure 5-19) show that this surface profile in fact leads to a maximum electric field strength, 3.5×10^6 V/cm at 800 kV, that is higher than that near the top of the insulator (2.5×10^6 V/cm). In contrast, the field strength with a smooth surface has a lower maximum field strength in comparison with that containing the corrugation (Figure 5-24). It is to be noted that the smoothness of the surface has a significant influence on the peak electric field. The two peaks at z = 0.23 m and z = 0.36 m in Figure 5-24 are due to the sudden change of the surface tangential direction, leading to small radius of curvature on the surface. Therefore, in practical insulator design and manufacturing, the smoothness of the surface can have a significant effect on the local electric field.

It is clearly shown that the effective electrical conductivity in SF_6 varies along the insulator surface by a factor of 2. In the absence of a surface layer, minimum surface charging can be achieved if the effective electrical conductivity of the gas is approximately equal to that of the insulator. Ideally, the electrical conductivity distribution of the solid insulation material along the insulator surface should also be optimized based on the effective electrical conductivity of the gas at steady state which can be calculated using the mobility of the ions and ion number densities.

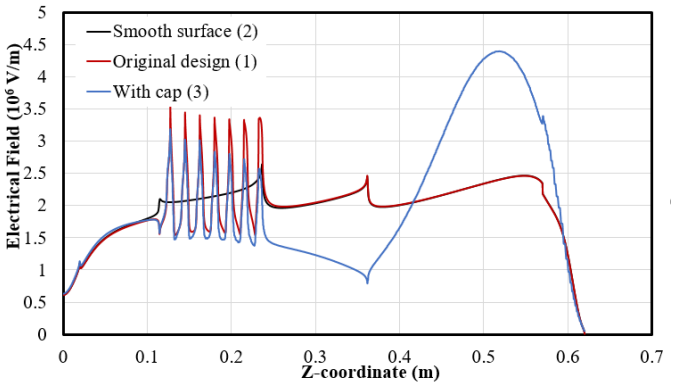

(a)

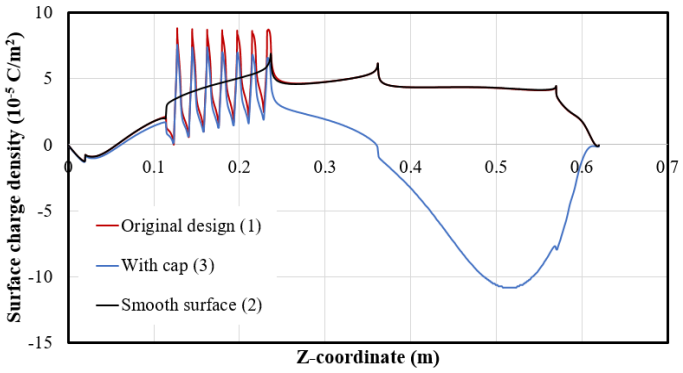

(b)

Figure 5-24 Electric field strength (total field) (a) and surface charge density (b) at the insulator surface for three cases: original design (1); crest-furrow corrugation replaced by smooth surface (2), and central conductor replaced by a cap (3).

5.3.4 Effect of Shielding of Triple Junction

The triple junction is always a matter of concern in the operation of insulator if it is not well shielded. Results in Figure 5-25 show that with the shielding cap of the connector the total electric field becomes much higher than the simple geometry given in Figure 5-25b). The maximum field strength with the cap appears at a vertical position that is level with the bottom of the cap. It increases from 2.4×10^{6} V/m with the simple shape central electrode to 4.4×10^{6} V/m with the shielding cap, an increase of 83%. Much more negative charges are accumulated on the surface in this region as well.

A close examination reveals that in the present case the electrical conductivity of epoxy is 1.6×10^{-16} S/m (manufacturer supplied value) which is much larger than the effective electrical conductivity of SF_6 which is in the range of 2.14×10^{-18} S/m to 5.35×10^{-18} S/m. Thus, epoxy is much more conducting than SF_6 and the gas gap between the inner downwards side of the cap and the upper part of the insulator is exposed to a high potential and the electric field is thus enhanced. The electric field vector given in Figure 5-26a indeed shows that there is a dominant normal electric field at the surface in the upper part of the insulator. With a higher epoxy electrical conductivity, the idea of using this shielding cap does not suppress the electric field,

instead it enhances the field strength which is not favored.

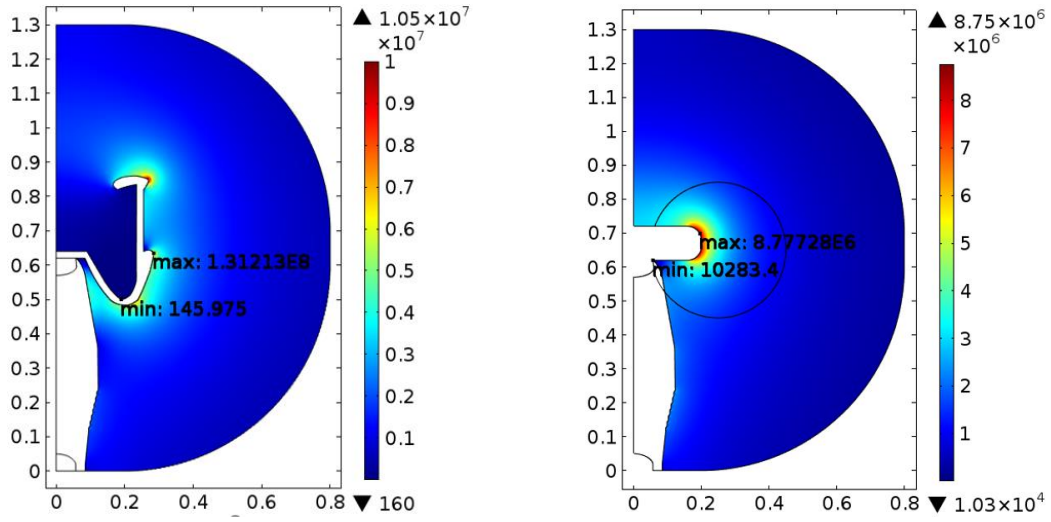

(a) *(b)*

Figure 5-25 Electric field strength distribution in the gas domain with a shielding cap a) and with a simlifed central conductor b) for the insulator at 800 kV.

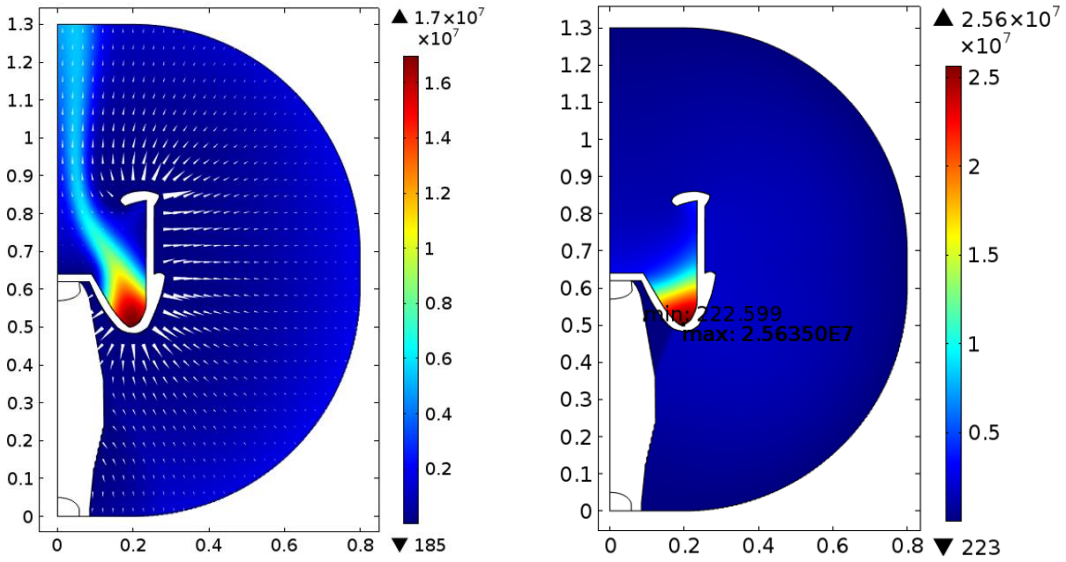

(a) *(b)*

Figure 5-26 Positive (a) and negative (b) ion number density distribution in the gas domain with the shielding cap on the high voltage side of the insulator.

Computation was also performed at 200 kV and 1100 kV for the insulator with the shielding cap. The distribution of ion number density is similar to Figure 5-26. Results in Figure 5-27 and Figure 5-28 show that at all three voltage levels the use of the shielding cap greatly enhances the local electric field near the top of the insulator. The maximum electric field at the upper-outer edge of the cap is 2.5×10^7 V/m at 1100 kV. The maximum electric field along the insulator surface is 6×10^6 k/m, as shown in Figure 5-28. Compared with the 800-kV case with the central electrode shown in Figure 5-22, there is a much larger amount of negative charge accumulated on the insulator surface, therefore changing the local potential distribution and also local electric field on the surface.

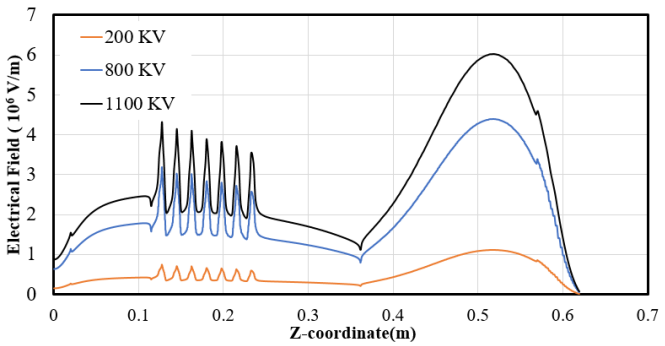

Figure 5-27 Electric field on the insulator surface at three applied voltages of 200 kV, 800 kV and 1100 kV with the shielding cap.

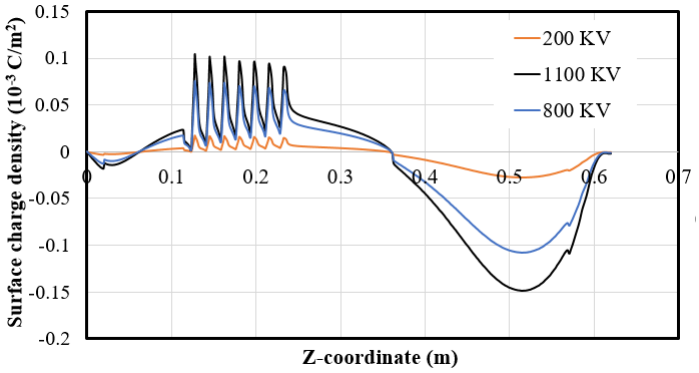

Figure 5-28 Surface charge density distribution at three applied voltages of 200 kV, 800 kV and 1100 kV with the shielding cap.

5.4 Computational Analysis of the Performance of an 1100 kV Epoxy Spacer with Surface Layer

5.4.1 Insulator Behaviour under Different Applied Voltages

In this section, a surface layer is considered and it has a typical thickness of 50 um, as assumed in most publications. Its volumetric electrical conductivity is 1.8×10^{-11} S/m, much higher than that of epoxy. The choice of this higher electrical conductivity is for the study of the role of the surface layer in affecting the electric field distribution near the insulator surface. The other discharge conditions are summarized in Table 5-2. The typical mesh size is 0.25 mm near the gas-solid interface. The effect of introducing a false diffusion coefficient has already been checked in Chapter 4. A segregated solver is used to obtain the solutions. It offers better convergence compared with the other solvers for the case under study.

Table 5-2 Key parameters used in the computation

Conditions	Modelling Group 1	Modelling Group 2
Applied voltage (DC)	2 kV to 800 kV	800 kV
Electrical conductivity of epoxy for the isulator body	1.6×10^{-16} [S/m]	1.6×10^{-16} [S/m]
Ion Mobility	4.8×10^{-6} [m^2/(Vs)]	4.8×10^{-6} [m^2/(Vs)]
Recobination coefficient	2.27×10^{-13} [m^3/s]	2.27×10^{-13} [m^3/s]
Ion pair gengeration rate	2.9×10^{7} [1/(m^3s)]	0.1, 2.9, 5, 10, 100 $\times10^{7}$ [1/(m^3s)]

In this section, two groups of case are modelled. The cases in the first group contain the same surface layer but at different applied voltage. It is important to know that when the applied voltage increases, how the ion number density distribution changes and also how the space charge density is influenced by the increase in the applied voltage. In the second group the ion pair generation rate is changed to studey its

influence on the ion number density and electric fiedl distribution because it is a model parameter whose accurate value is not known and may change at different geometric locations.

Before presenting the results, the presence of ions in the gas needs to be discussed. With the data given in Table 5-2, the number density of both positive and negative ions at equilibrium with no applied electric field is 1.13×10^{10} m^{-3}. With this number density and a mobility of 4.8×10^{-6} $m^2/(Vs)$, we can work out an equivalent electrical conductivity of 1.74×10^{-14} S/m. This value is much larger than the value of 3.31×10^{-18} given in [5.3]. Different literatures give different values. In the present work, the concept of electrical conductivity can no longer use because the negative and positive ion number density changes drastically in the presence of a strong electric field. Without going into details, it can be seen from Figure 5-29 that there are 4 locations with enhanced electric field. These locations are the surface of the central conductor interfacing with the gas, around the surface of the two tips of the two electrodes interfacing with epoxy, and finally along the middle section of the insulator surface. The vectors in red clearly show the direction of the electric field, which is also the direction of drift movement of the ions.

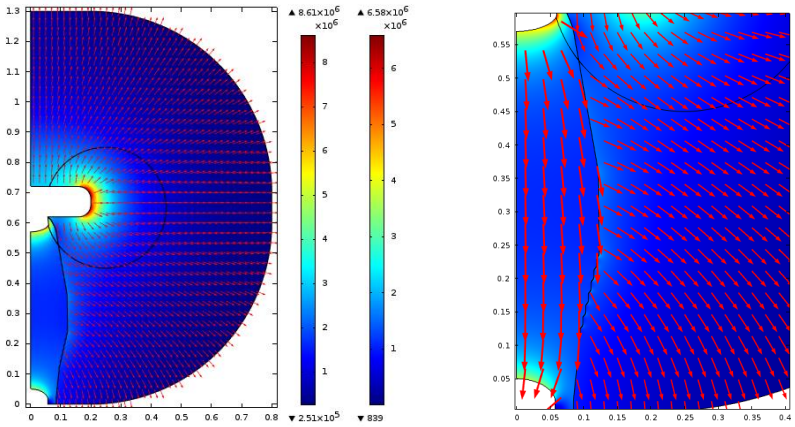

(a) *(b)*

Figure 5-29 (a) Color diagram of electric field distribution, the first color scale column is for the gas region and the second one is for the solid region. The applied voltage is 800 kV. The red vector represents the electric field. (b) Zoomed view of spacer.

As we have assumed, the metallic wall is an ideal absorber for positive charges and ideal rejector for negative ions. Under the influence of an applied electric field, negative ions move towards the live electrode surface and the insulator surface. The only source to generate the ions is due to the ion pair. Due to the removal of the ions by drift, the number density near the metallic wall becomes low, reaching a value of 1.0×10^{6} m^{-3} at a location of 5 cm from the metallic surface of the wall.

The highest value appears near the central electrode with a value of 6.2×10^{6} m^{-3}, as shown in Figure 5-30 (a). The arrows in Figure 5-30(b) indicate that negative ions approach the central conductor surface at a right angle, which is what we normally expect. However, they approach the insulator surface at different angles, depending on the location on the surface. The positive ions behave in an opposite manner from that of the negative ions. Because the electric field pushes the positive ions away from the conductor and insulator surface, the positive ion number density becomes very low near the insulator surface and reaches a maximum near the earthed wall (Figure 5-30(c)). The maximum number density of the positive ions is 5.9×10^{6} m^{-3}, slightly lower than that of the negative ions, 6.2×10^{6} m^{-3}. Both are three orders of magnitude lower than the equilibrium value which is equal to $\sqrt{\frac{S_{IP}}{k_r}}$, effectively reducing the electrical conductivity of the gas.

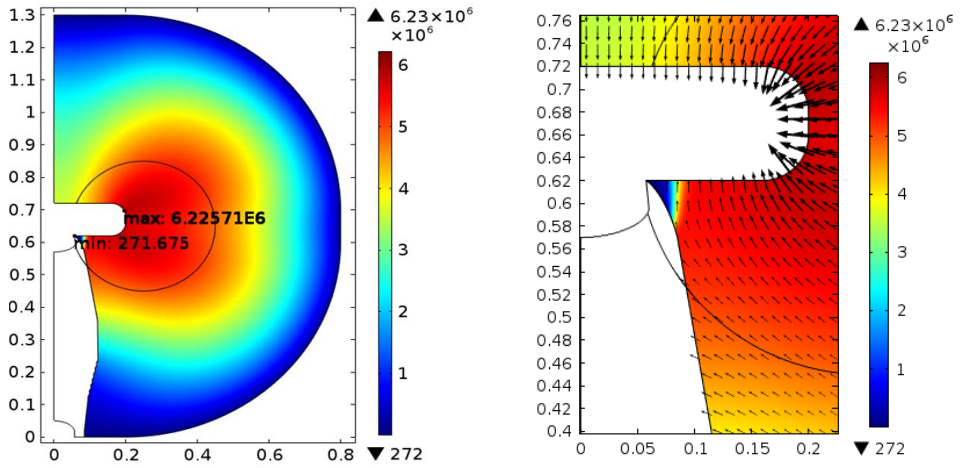

(a)Negative ions *(b) Zoomed view*

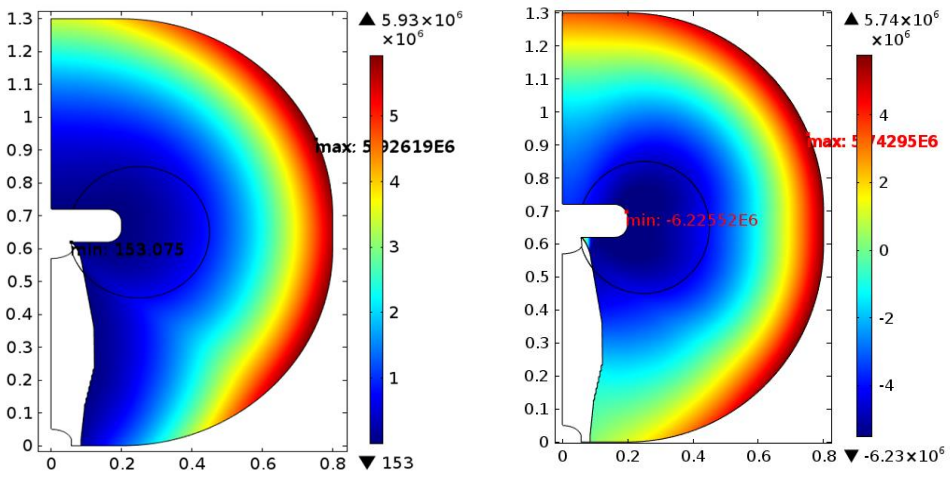

(c) Positive ions *(d) Difference in ion number density*

Figure 5-30 (a) Negative ions distribution. (b) Zoomed view around the triple junction point. (c) Positive ions distribution. (d) Difference in positive and negative ion number density leading to space charge. The applied voltage is 800kV.

With the presence of a positive central conductor, it naturally attracts the negative ions to move towards its surface. Thus, the number density of negative ions is high ($5\times10^6/m^3$) along the surface of the upper half of the insulator. It is interesting that most of the negative ions avoid moving into a small region immediately by the triple junction, as shown by the vector for drift velocity in Figure 5-30 (b), thus leaving an extremely low number density of negative ions. Most of the positive ions are attached to the wall bushing out shell.

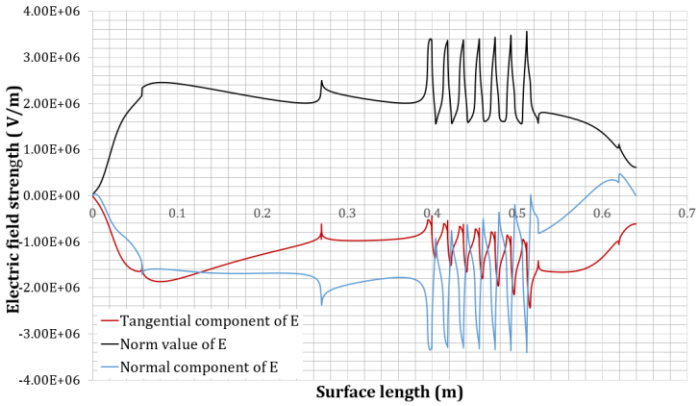

Figure 5-31 Electric strength of the surface layer within the real spacer shape, the applied voltage is 800 kV.

Results in Figure 5-31 and Figure 5-32 show that the electric field intensity along the surface profile line varies drastically. In the region close to the central conductor, the electric field is extremely high, reaching 4.0×10^6 V/m. It attenuates quickly to 1.5×10^6 V/m at 10 cm away from the top end of the surface layer domain before increasing again at the middle of the surface layer profile line with a field strength of 3×10^6V/m. On contrast, the tangential component of the electric field is less varying (red curve in Figure 5-31). In order to reduce the maximum electric field strength along the insulator surface and to make the electric field distribution more uniform, optimization of the structure of the central conductor especially the region close to the triple junction will be necessary.

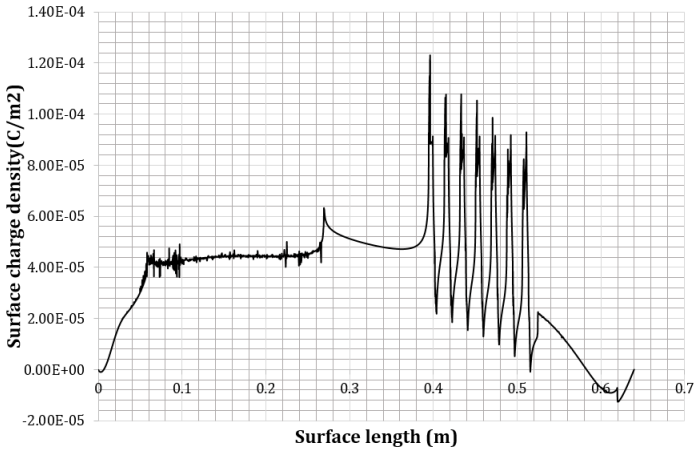

Figure 5-32 Surface charge density within the real spacer shape, the applied voltage is 800 kV.

5.4.2 Insulator Behaviour under Influence of Ion Pair Generation Rate

As discussed before the existence of the ions in the surrounding area of the spacer is due to the generation of the ion pairs by cosmic rays which is the only mechanism considered in the present model. Thus, it is expected that the generation rate will affect the maximum number density of the positive and negative ions. When the ion pair generation rate is 1×10^6 IP/(m^3s), the equilibrium value of the ion number density is 2.1×10^9 m^{-3} . It is 6.64×10^{10} m^{-3} for $S_{IP} = 1\times10^9$ IP/(m^3s).

With an applied voltage of 800 kV, the maximum number density of the positive ions increases by a factor of 1000 when the ion pair generation rate increases from 1×10^6 IP/(m^3s) to 1×10^9 IP/(m^3s). The distribution profiles are similar, as can be seen from Figure 5-33.

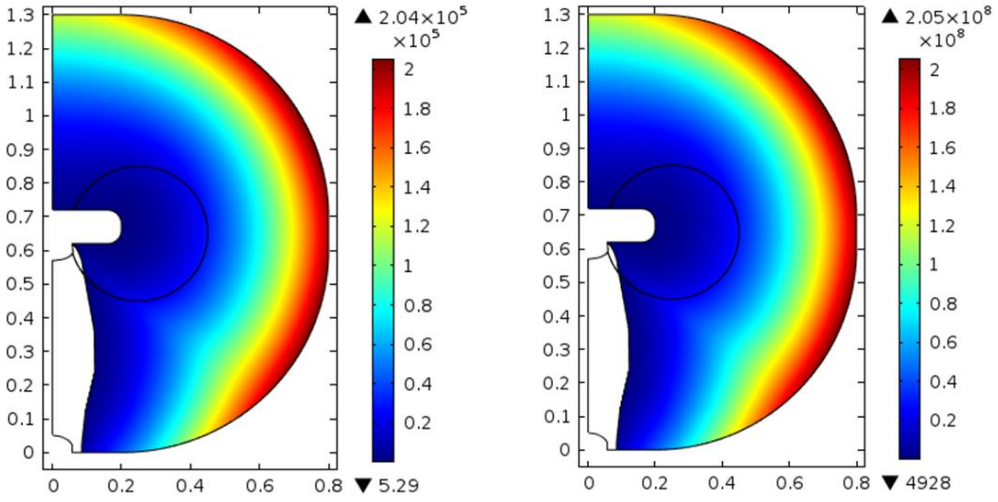

(a) *(b)*

Figure 5-33 Positive ions number density distribution with ion pair generation rate set to (a) 1×10^6 IP/(m^3s); (b) 1×10^9 IP/(m^3s). The applied voltage is 800 kV.

However, with an applied voltage of 2kV, the positive ion number density distribution exhibits a fundamental change in their pattern when the ion pair generation rate increases from 1×10^6 IP/(m^3s) to 1×10^9 IP/(m^3s), as shown in Figure 5-34 and Figure 5-35. On the one hand, the maximum value of the number density increases from 7.0×10^7 m^{-3} to 2.2×10^{10} m^{-3}, an increase by a factor of 314, the minimum value of the number density behaves differently. With the increase in the generation rate, the minimum value drops from 2.4×10^7 m^{-3} to 5.2×10^6 m^{-3}.

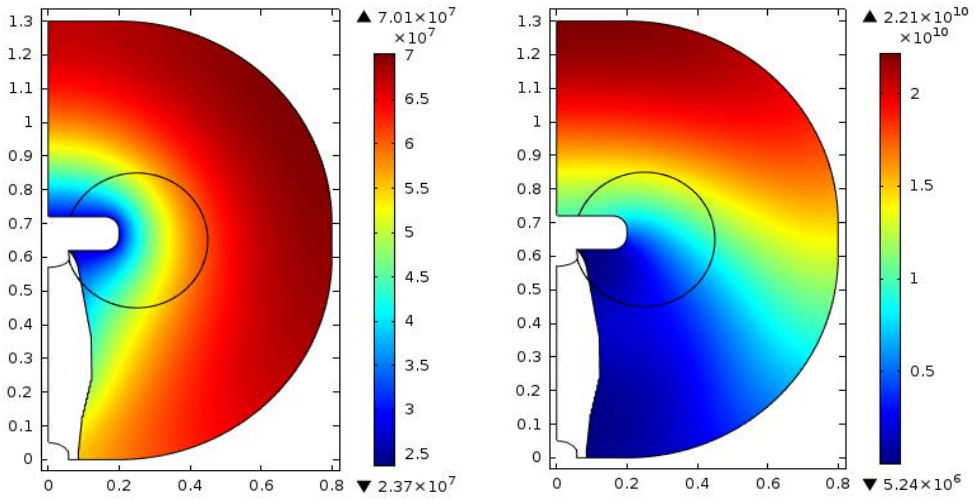

(a) *(b)*

Figure 5-34 Positive ions number density distribution. (a) ion pair generation rate is 1×10^6 IP/(m^3s); (b) ion pair generation rate is 1×10^9 IP/(m^3s). The applied voltage is 2 kV.

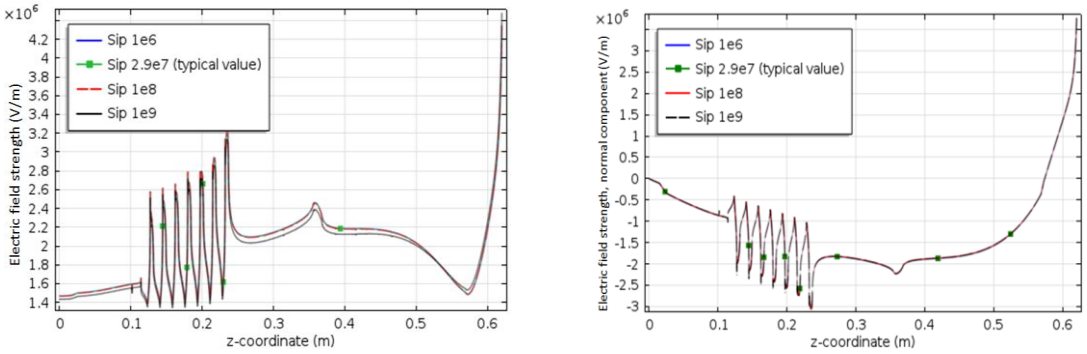

(a) *(b)*

Figure 5-35 (a) Comparison of the electric field strength on the surface layer in gas region with four different ion pair generation rates, (b) is the normal component.

According to the charge carrier density under equilibrium state equation, when the ion pair generation rate is 1×10^6 IP/(m^3s), $n^+ = n^- = 0.21\times10^{10}/m^3$ and when it is 1×10^9 IP/(m^3s), $n^+ = n^- = 6.64\times10^{10}/m^3$. The overall ion density is quite lower than the equilibrium value, this is because when the applied DC voltage increases, the ions will

drift at a higher speed, take a control volume to consider, the number density inside of the control volume decreases with the higher speed.

5.5 Summary

The comparison in Section 5.2 indicates that the charge transport model established in the present work correctly considerers the important mechanisms responsible for charge accumulation on insulators under HVDC stress. The predicted surface charge distribution and surface potential distribution closely follows the measurement. The dominant mechanisms responsible for charge accumulation are clearly explained with examples.

It has been found that the difference between the effective electrical conductivity of the gas and that of the epoxy controls the enhancement of the normal electric field component along the insulator surface. For a given geometry this field component is minimized when the two effective electrical conductivities are close to each other, providing a theoretical guidance for the optimization of the conductivity distribution inside the epoxy insulator through the use of gradient material. The model developed in this work is able to aid the optimization process.

The effectiveness of the original design of the connector is also studied. It is shown that the shape profile of the lower part of the connector shields the strong electric field at the triple junction but enhances the normal electric field near the upper part of the insulator surface, leading to strong accumulation of negative charge. Therefore, it is not an optimized design.

Finally, our results also show that the use of the ridge-furrow shaped corrugation on the surface of the lower part of the insulator does not significantly increase the creepage, instead it induces strong electric field. Therefore, it is not an effective measure to increase the dielectric strength of the whole spacer. It is recommended that smooth surface should be used.

5.6 Reference

[5.1] H. Fujinami, T. Takuma, M. Yashima and T. Kawamoto, “Mechanism and effect of DC charge accumulation on SF_6 gas insulated spacers”, *IEEE Trans. Power Del.,* vol. 4, no. 3, pp. 1765-72, 1989.

[5.2] S. Singha and M. J. Thomas, “Dielectric properties of epoxy nanocomposites”, *IEEE Trans. Dielectr. Electr. Insul.,* vol. 15, no. 1, pp. 12-23, 2008.

[5.3] A. Winter and J. Kindersberger, “Transient field distribution in gas-solid Insulation systems under DC voltages”, *IEEE Trans. Dielectr. Electr. Insul*., vol. 21, no.1, pp. 116-128, 2014.

[5.4] Multiphysics COMSOL, "Reference Manual for Version 4.4”, pp. 162-168, 2013.

CHAPTER 6 EXPERIMENTAL INVESTIGATION OF THE EFFECT OF CHARGE TRANSPORT AND SURFACE CHARGE ACCUMULATION ON HVDC INSULATOR

The experimental cases reviewed in Chapter 2 employed insulator samples of relatively small size (typically 50 mm in length and 40 mm in diameter). The applied voltage was up to 300 kV. The gases used include SF_6 and air. In the operation of real insulation systems, partial discharges always exist although their severity varies. There can also be minor surface irregularities on the electrode or even minor surface defects on the insulator itself. The test results obtained in laboratory under strictly controlled conditions may not reflect the true insulation behavior of insulators.

The experimental work in this chapter aims at a study of the discharge behavior of epoxy insulators in different gases (SF_6 and CO_2), at different gas pressures (1 bar – 3 bar) and with various applied HVDC voltages (200 kV to 400 kV) under conditions close to real operational environment. It is expected that the experiments performed in this chapter will represent discharge and insulation behavior of real insulation system. The experiments were performed at the SGCC (State Grid Corporation of China) Wuhan Ultrahigh Voltage (UHV) Test Base with support from Tsinghua University, China Electrical Power Research Institute (CEPRI) Wuhan Branch and Pinggao Group.

An electrostatic potential probe was used to measure the potential distribution along the insulator surface after the application of an HVDC voltage for a specified period and both electrodes were earthed. Some of the measurements were repeated where practical conditions allow to do so.

6.1 Experimental System

The experimental system consists of four parts, the HVDC voltage supply, the test chamber, insulator driving mechanism, and the potential measurement circuit, as shown in Figure 6-1.

The HVDC power supply is able to deliver a DC voltage of 800 kV for both positive and negative polarities with a maximum current of 30 mA. Figure 6-2 is a photo of the control panel of the voltage supply (with only Chinese characters displayed). However, the meaning of relevant readings will be explained when they are quoted in the text. The voltage supply has been regularly calibrated with an accuracy of better than 0.1%. The other three parts of the experimental system will be explained in the following sections.

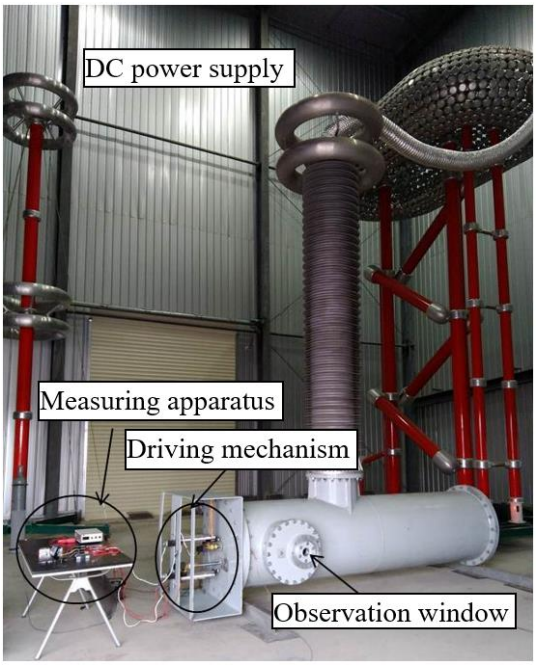

Figure 6-1 A photograph of the experimental system, including DC power supply, test chamber, insulator driving mechanism and potential measuring circuit.

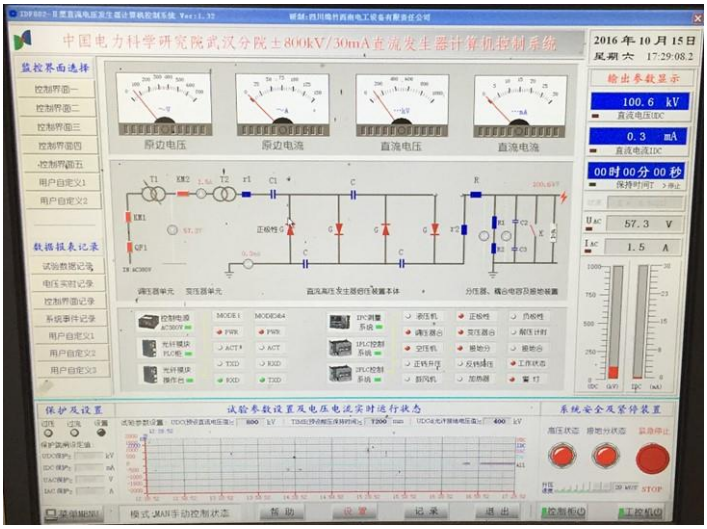

Figure 6-2 A photo of the front control panel of the HVDC supply. The instant output voltage and current are shown on the top-right corner of the panel with blue background.

6.1.1 Test Chamber

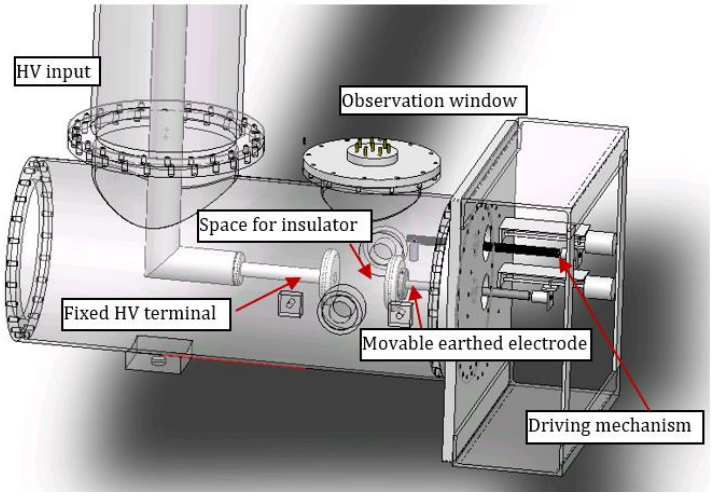

Figure 6-3 Schematic diagram of the internal structure of the test chamber used in the present work. The position of the observation window in this diagram should be at the back side of the chamber, referring to Figure 6-1 for correct position of the observation widow.

As shown in Figure 6-3, the DC voltage is applied to the fixed high voltage terminal a bushing installed vertically. The bushing has a height of 1.80 m which was originally designed for a voltage level of 1100 kV. The test chamber has an internal diameter of 0.80 m. The insulator under test was connected to the fixed and movable disk-shaped electrodes. The movable earthed electrode can be displaced or rotated by step motors via the driving mechanism (on the right-hand side of the diagram). As the experimental setup has to be gas tight, the movable rods through the holes on the end cover of the chamber have to be properly sealed to eliminate any gas leakage. More details of the experimental arrangement in the test chamber will be given in the following sections.

Before sealing the observation window cover for a high voltage test, an ultraviolet camera was used to identify locations of severe partial discharges while the chamber is filled with air. Severe discharges were observed at the location of connection between the high voltage disk-shaped electrode and the metallic insertion into the insulator at a voltage of 100 kV in air with high humidity. The metal and insulator surfaces near the connection was then cleaned and the insulator realigned with the disk-shaped electrodes. This effectively eliminated the strong partial discharge originally observed.

The second location for strong partial discharge in air (when the chamber was open) was near the edge of the high voltage disk-shaped electrode due to the non-satisfactory smoothness of the metallic surface. Partial discharges were not detected using PD detectors after the chamber was sealed and filled with SF_6 at higher pressure.

6.1.2 Test Sample and Measurement System

(a) *(b)* *(c)*

Figure 6-4 Photos of (a) epoxy insulator; (b) end of insulator with metal insertion; and (3) insulator connected to the disk-shaped electrodes by a bolt.

The insulator and electrodes are shown in Figure 6-4. The insulator is made of epoxy composite material and prepared by Pinggao. There is a metallic insertion of 20 mm deep and 20 mm in diameter. The disk-shaped electrodes as shown in Figure 6-4 (c) are connected to the insulator through a bolt. The insulator has an overall length of 150 mm and diameter of 50 mm at one end and 55 mm at the other end. The diameter of the disk-shaped electrodes is 100 mm. A photo of the insulator in its test position is given in Figure 6-5 where the electrostatic measurement probe is also shown.

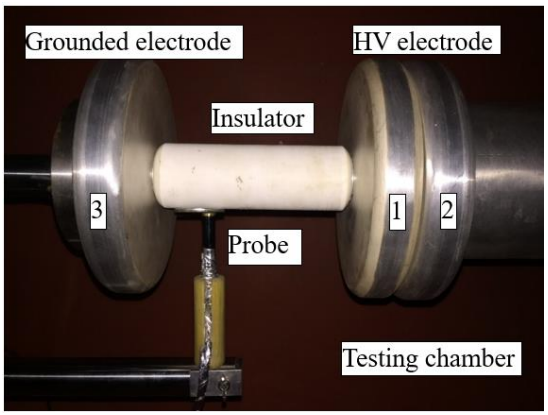

Figure 6-5 Arrangement with an electrostatic probe in the testing chamber.

The electrostatic potential probe used in the present work is Trek 6000B5C with matching conversion circuit (Model 347). It has a DC measurement range of 0 – 3000 V. The sensing head has a diameter of 11.2 mm (Figure 6-6). The technical specification of the sensor is listed in Table 6-1. The sensor was parked at a shielded location (on the left-hand side of disk 3 in Figure 6-5) for protection when a high voltage was applied to the insulator. On completion of the voltage application, the high voltage was reduced to zero and the HVDC feeder wires earthed. The two disks on the high voltage side (disk 1 and disk 2) were then separated physically by the driving mechanism to provide physical insulation from the voltage source. Thus, the high voltage end of the insulator is floating during the measurement process. The probe was then moved towards the insulator for potential measurement. The output of the probe at the measurement locations has been calibrated against a standard HVDC voltage source (0.1% accuracy) which is connected to a thin strip of conducting foil tightly and smoothly attached to the insulator surface.

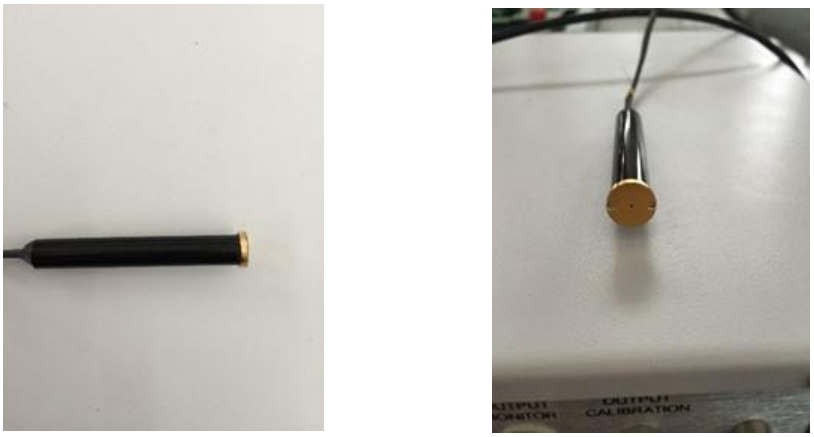

(a) *(b)*

Figure 6-6 Photograph of electrostatic probe.

The position of the insulator during the measurement is changed by the driving system, as shown in Figure 6-7. The four motors (M1 – M4) are connected to four drive boards (B1 – B4) which share a single controller. The positional coordinates (longitudinal and rotational) are read from the four-tape measure strap attached to the end of the

shafts or the guiding tracks (Figure 6-7b).

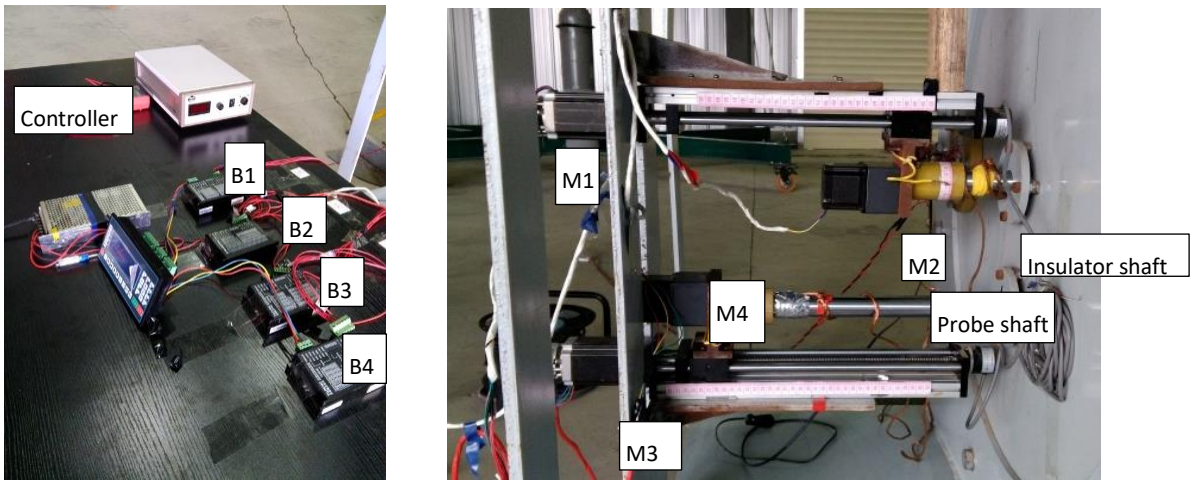

(a) *(b)*

Figure 6-7 Diagrams showing a) motor control circuits; b) driving mechanism for insulator and probe. M1 – insulator displacement motor, M2 – insulator rotation motor, M3 – probe displacement motor, M4 – probe rotation motor.

Table 6-1 Technical specification of the electrostatic probe and measurement circuit.

Measurement range	0 to ±3 kV DC or peak AC
Voltage monitor output	Better than ±0.05% of full scale
Voltage display	Better than ± 0.1% of full scale
Voltage of power supply	90 to 127 V AC or 180 to 250V AC, at 48 to 63 Hz
Power consumption	50 VA max
Operation Temperature	0˚C to 40 ˚C
Relative humidity	Up to 90%, noncondensing
Altitude	Up to 2000 meters

6.2 Experiment Preparation and Procedure

Due to the length and weight of the insulator positioning shaft and the insulator itself, the insulator does not stay on the central axis when its high voltage end is detached from the high voltage disk-shaped electrode. Instead it moves slightly downwards while travelling towards the high voltage side. On the other hand, the probe shaft moves in a line parallel to the central axis because of the low weight of the shaft and the probe itself. This means the gap length between the insulator surface and the probe can be affected by the insulator position. This was resolved in the measurement by parking the insulator at the same position in different measurement rounds.

Another factor that changes the gap length between the insulator surface and the probe is that the diameter of the insulator changes from one end to another end. In the experiment, the end with larger diameter was connected to the earthed electrode, as shown in Figure 6-8. The decreasing diameter of the insulator towards the high voltage electrode cancelled part of the influence of the misalignment of the insulator shaft. Despite this there was still small variation of the gap length when the probe scanned through axial length of the insulator. Therefore, a calibration on the effect of the gap length variation on the potential reading needed to be carried out.

The calibration was done by first wrapping a layer of thin conducting foil around the whole insulator surface and then connected to a DC high voltage supply. The applied voltage is lower than 3 kV. The probe was then moved into its measurement position and displaced across the length of the insulator. It was found that when the gap length changed from 3 mm to 6 mm, the reading from the probe measurement circuit only varies by less than 1% at a voltage of 2900 V, and the effect of varying gap length between the insulator surface and the probe head is therefore ignored in our measurement.

In addition, due to the tolerance in the mechanical driving mechanisms, it is possible that a lightly different location can be reached when we move the probe or rotate the insulator from two opposite directions. This has also been checked in the experiment to assess the maximum error. Repeated scans have shown that the spatial repeatability is better than 2 mm or 10 degrees.

The following preparation or checks have to be carried out before the experiment.

1) A calibration system should be used to support and insulate a dummy insulator having the same dimensions as the test insulator but with conducting surface. It is then charged to a known DC voltage. A probe should then be positioned with its head surface parallel to the tangential surface of the insulator to calibrate the probe reading when the gap length between the insulation surface and the probe head is varied within a chosen range.
2) Firm and proper earthing of the test chamber is extremely important to avoid discharge to the probe cable and other electronic equipment placed nearly bt the chamber.
3) Good electrical contact and connection has to be ensured when the insulator is installed to minimize the occurrence of partial discharges. For this purpose, each time after installing the insulator and before closing the observation window cover, an ultraviolet camera needs to be used to detect if there is excessive partial discharges around the insulator. After this check, the observation window cover can be installed, followed by gas filling.

The following procedure needs to be followed in the execution of an experimental shaft:

The insulator has to be cleaned and dried before installation unless it is deliberately left as untouched. After placing it between the electrodes, its surface has to be cleaned again before the test chamber is sealed.

Before the application of the high voltage, the experimenter has to ensure that the probe cable inside the chamber and the sensor head will not be exposed to strong electric field or near high potential conductor during the application of high voltage. This is because the sensor will be earthed during the application of the high voltage and no discharge to the sensor or cable is allowed.

On completion of a prescribed length of voltage application on the insulator, the applied high voltage can be reduced to zero and the feeder wire be earthed, either by the power source or through manual earthing.

The guiding tracks should be stiff enough to maintain a sufficiently stable gap length

between the insulator and the probe head. If this is not possible the variation in gap length during the translational movement of the probe should be recorded so necessary correction can be applied later based on calibration data.

The insulator is to be detached from the high voltage disk-shaped electrode by the step motor based driving mechanism. Once the insulator reached its parking position, the probe is first rotated then moved in the axial direction and finally positioned properly at a location close to the earthed end of the insulator.

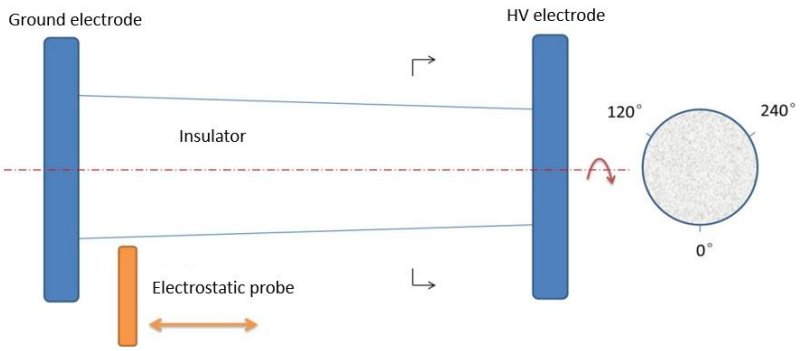

Figure 6-8 Schematic diagram showing the direction of axial and circumferential scan of the insulator surface by the probe.

6.3 Results and Analysis

Two epoxy insulators of the same shape and dimensions were used in the experiment. A set of experiments were performed following a planned order based on consideration of the operational issues. N_2, SF_6 and CO_2 were used in the experiment. The procedure given in Section 6.2 has been followed in the measurement

6.3.1 Experiment with N_2

The pressure of nitrogen gas is 1.1 bar absolute. The purpose of this round of test is to provide some baseline data for late comparison with the behavior of the insulator in SF_6 and CO_2. The applied voltage and the application time are summarized in Table 6-2.

Table 6-2 Applied voltage and voltage application time for experiment in nitrogen.

No.	Applied DC voltage (kV)	Voltage application time (h)	Total voltage application time (h)
1	+150	0.5	0.5
2	+150	0.5	1.0
3	+150	0.5	1.5
4	+170、223	Spark occurred	
5	+200	0.5	2.0
6	+200	0.5	2.5
7	+200	0.5	3.0

It is known that N_2 has a lower insulation strength in comparison with SF_6. In this round of experiment, the contact gap is able to withstand a DC voltage below 150 kV without spark. It is interesting to observe that at 170 kV surface flashover did not develop. Instead a spark discharge took place. This is believed to be associated with the micro burrs on the surface. Before the spark discharge, the potential distribution induced by the accumulated charge along the insulator surface was measured. Results are shown in Figure 6-9. The horizontal axis is labelled with measurement points, not the actual coordinate. Point 1 is 10 mm close to the earthed electrode and the last point corresponds to a point 10 mm away from the high voltage electrode surface, giving a spatial interval of 3.1 mm between two points.

Due to the relatively low applied voltage (150 kV), little surface charge was accumulated, giving only a maximum potential of 50 V in 1.5 hours. This voltage is small and the reading from the electrostatic potential has an uncertainty of 10 V, which does not allow us to make any sound judgement. The spark discharges however substantially changed the surface potential along the measurement line, as shown in

Figure 6-9(b). It is believed that the spark discharge generated a large amount of positive and negative charges in gas surrounding the insulator and these charges are attracted towards the insulator surface by the electric field. The polarity of the charge attracted depends on the direction of the electric field. Based on Figure 6-9(b), it is obvious that positive charges are accumulated on the surface near the earthed electrode while negative charges accumulated on that near the high voltage electrode. This is in agreement with what we expect.

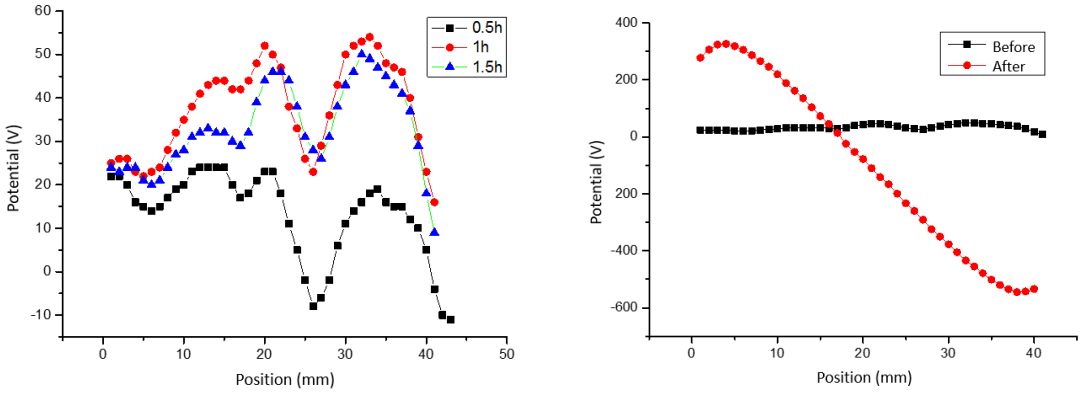

(a) *(b)*

Figure 6-9 Electrostatic potential along insulator surface after the application of 150 kV DC voltage for different time. Gas is N_2 at 1 bar. (a) measurement along a line of zero azimuthal angle (Figure 6-8) in N_2 before the occurrence of spark discharge. (b) comparison of potential measurement before and after spark discharges at an application time of 1.5 hours and 2 hours.

Two sparks occurred. After the second spark discharge at 223 kV, the voltage was maintained at 200 kV for another 1.5 hours with the potential distribution measured every half an hour. Measurement results in Figure 6-10 show that after the deposition of charges on the insulator surface during the spark discharge, little surface charge is further accumulated on the insulator surface because the potential distribution remains very close to each other except a small length immediately by the high voltage electrode.

Measurements were also taken around the azimuthal direction at a number of axial positions on the completion of 3 hours high voltage application within the range of 150 kV to 200 kV. The first point and last point on the horizontal axis represent the same point on the insulator surface. Point 1, which corresponds to the 0-azimuthal angle (Figure 6-8) acquires the highest or lowest voltage induced by the accumulated charges. It has to be noted that the position values displayed in the keys to the curves are referenced to the high voltage side. 0 mm indicated the point closest to the high voltage electrode. The general pattern is that the insulator surface potential along the 0^o axial line is most affected (Point 1) while the potential on the opposite of the surface (Point 9 in Figure 6-11) is least affected. Since the electrode-insulator assembly is axisymmetric, we can conclude that it is the asymmetric distribution of positive and negative space charges in the gas surrounding the insulator that causes the asymmetric charge accumulation on the insulator surface in the azimuthal direction. The cause for this asymmetry is the spark discharge. Therefore, the work in N_2 shows that:

- Charge accumulation in the absence of spark discharge between the two electrodes is insignificant at an applied voltage of 150 kV for the current configuration.
- Charge accumulation on the insulator surface can be severely affected by the development of ionization in the gas surrounding the insulator, such as a spark discharge striking between the disk-shaped electrode.

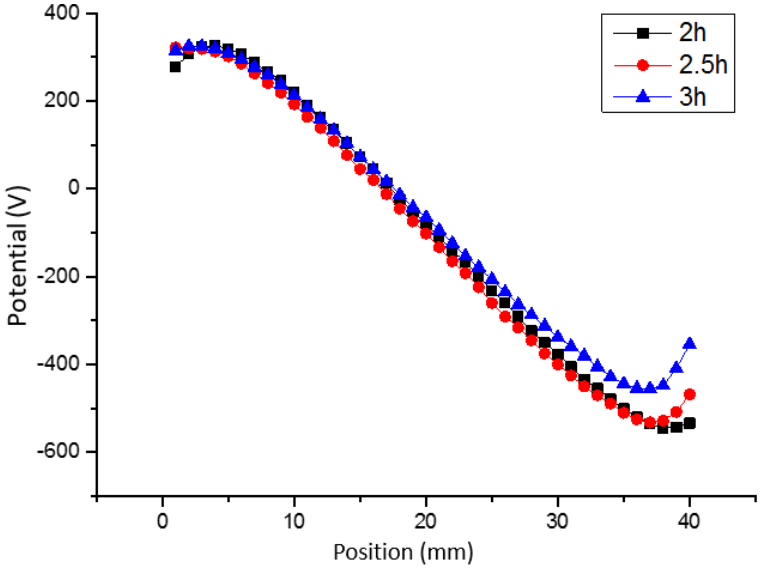

Figure 6-10: Evolution of surface potential distribution along 0º line at 200 kV. In the legend, 2h means a total voltage application time, but 30 minutes after the second spark discharge.

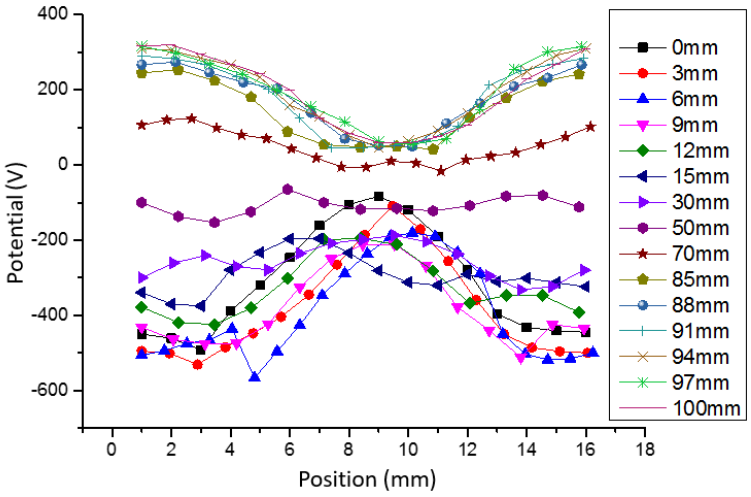

Figure 6-11: Surface potential distribution in the azimuthal direction at different axial positions. 0 mm is closest to high voltage electrode and 100 mm is closest to earthed electrode.

6.3.2 Measurement of Surface Potential in SF_6 at 1 bar

A. SF_6 at 1 bar Absolute

Experiment was first carried out with an SF_6 pressure at 1 bar. The potential distribution was measured every 30 minutes along the 0° axial line on the insulator surface. The insulator was the same as that used in the nitrogen test. From this test, measures have been taken to read the axial coordinate directly. The sequence of measurement is given in Table 6-3. The DC voltage remained constant at 200 kV.

Without spark discharge, substantial negative potential was induced by surface changes at the middle of the insulator over a length of 50 mm in the first 30 minutes, as shown in Figure 6-12. With an extention of the voltage application, the magnitude of the potential decreases and there is a trend of the charges to slightly move towards the high electrode. Both ends of the insulator are however at potential close to zero.

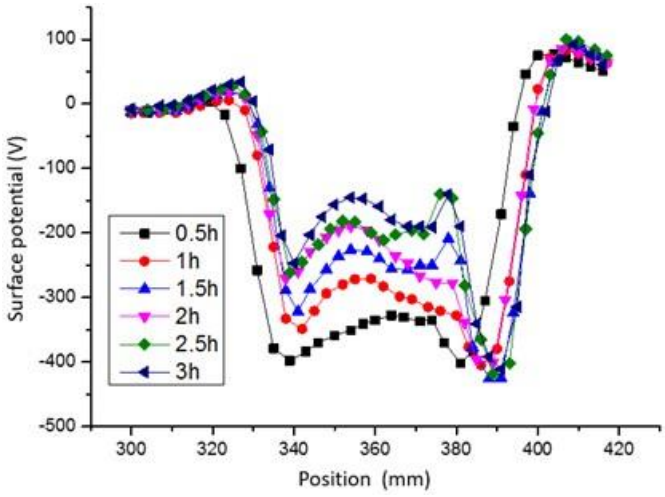

Figure 6-12 Surface potential distribution along the 0° axial line in SF6 at 1 bar. The applied voltage is 200 kV.

Table 6-3 Test sequence for SF_6 at 1.01 bar. The applied voltage is 200 kV and total application time is 3 hours, potential measurement was taken per half an hour.

Test number	Applied voltage/kV	Duration time/h	Total applied time/h
1	+200	0.5	0.5
2	+200	0.5	1.0
3	+200	0.5	1.5
4	+200	0.5	2.0
5	+200	0.5	2.5
6	+200	0.5	3.0

An important objective of the work in this section is to assess the charge dissipation rate, providing us information on the characteristics of charge transport in the absence of applied electric field. For this purpose, after the application of 3 hours of a voltage of 200 kV, the voltage was removed and the high voltage electrode was earthed for 13 hours. During this period, the accumulated charges start to diffuse into the gas and towards the earthed electrodes. For a more sensible comparison, the potentials before and after the 13-hour period of relaxation was measured on three axial lines, corresponding to 0°, 120° and 240° parallel to the axis of the insulator. Results are given in Figure 6-13.

Despite the very different distribution profile along the three lines, there are common features that can be extracted. Using the peak potential values, a ratio of around ¼ can be obtained. The average value ratio is in the range of 1/3- 1/5. Assuming a linear relationship between the charges and the potential (linear system) and an exponential delay of the potential, the average ratio of ¼ can be used to obtain a time constant of about 9.4 hours.

Another feature of the potential distribution along the lines is that on the 0° line, the

potential has the highest peak value of -440 V, moving towards the 120° line, the potential has peaks of +200 V and – 220 V. The peak is further reduced to 80V and -40 V on the 240° line, indicating the asymmetric nature of the charge distribution.

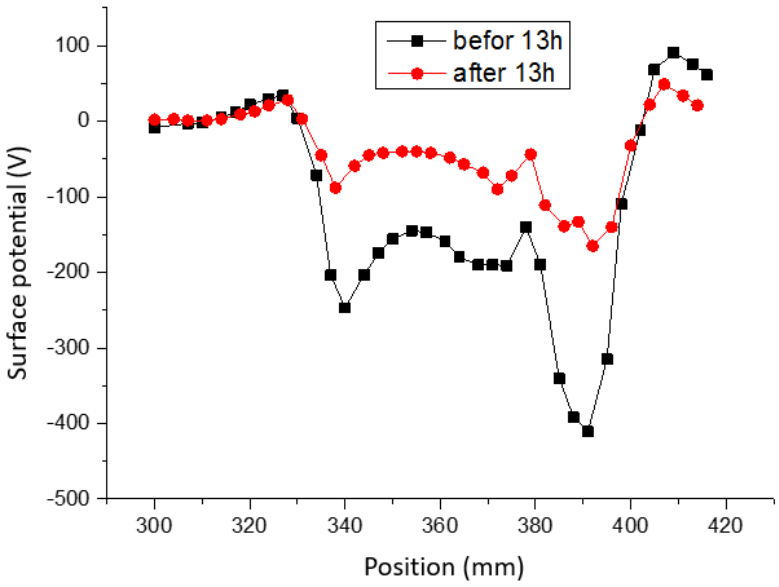

(a)

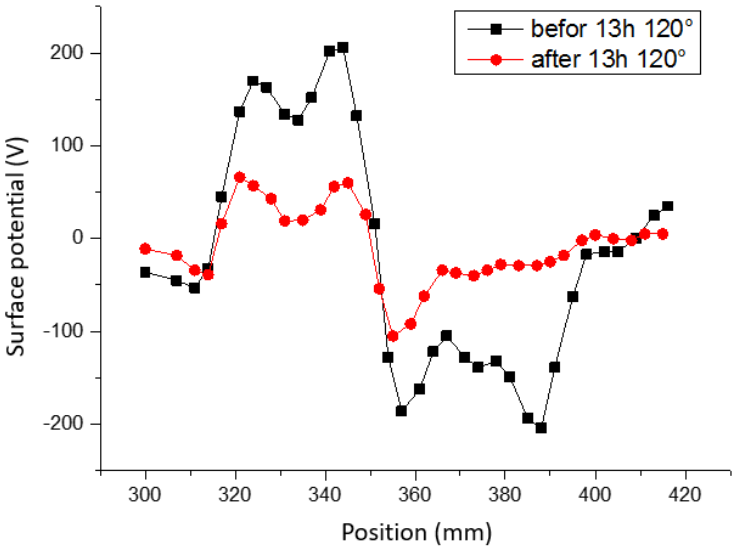

(b)

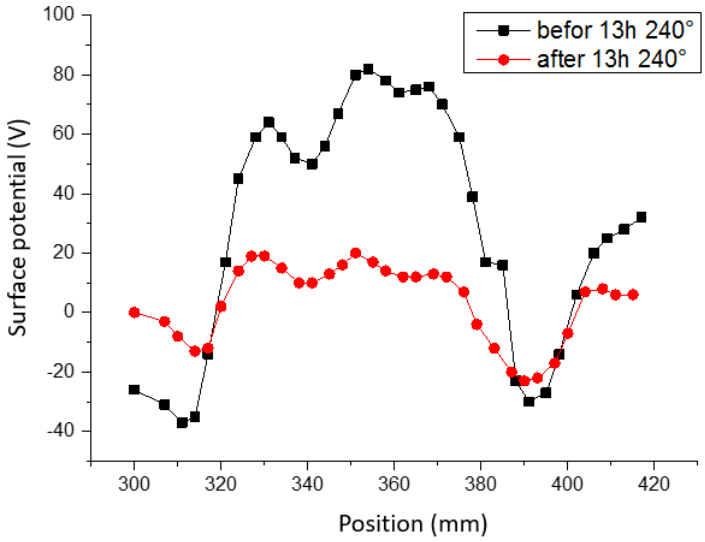

(c)

Figure 6-13 Change of surface potential along three axial lines on the insulator surface over 13 hours of charge relaxation in the absence of electric field. (a) along 0º line; b) along 120º line; and c) along 240º line.

B. Charge Accumulation in Epoxy Insulator in SF_6 during Spark Discharge

In order to study the effect of charge accumulation on the epoxy insulator during the process of spark discharge, the insulator is left as what it was on the completion of the experiment in section 6.3.2.1 and a higher voltage was applied. A spark developed at 325 kV. The voltage was removed and increased again from zero. Another spark developed at 322 kV, close to the voltage of the first one. Following the second spark, the potential distribution was measured and 300 kV was applied for different period of time with measurement of the potential distribution. Detailed experimental conditions were given in Table 6-4 when the flashover took place.

Table 6-4 Experiment arrangement to study the effect of spark discharge on the charge accumulation on insulator surface in SF_6 at a pressure of 1,01 bar.

Test number	Applied voltage/kV	Duration time/min	Total applied time /min
1	+325，+322	Spark	/
2	+300	10	10
3	+300	30	40
4	+300	30	70
5	+324	Spark	/
6	+300	30	100

Results in Figure 6-14 show that as a result of the spark discharge，more negative charges are accumulated near the high voltage electrode than the positive charges accumulated on the insulator surface near the earthed electrode (Figure 6-14a). during the further voltage application period of a DC voltage of 300 kV, the excessive charges (both positive and negative) accumulated on the insulator surface starts to diffuse with the possibility of neutralisation leading to an overall reduction in the potential value. Meanwhile, the drift of positive and negative electric charges in different directions under the applied DC field starts to induce fluctuation in the potential distribution. This is rather obvious at 70 minutes after the application of the 300-kV voltage following the spark.

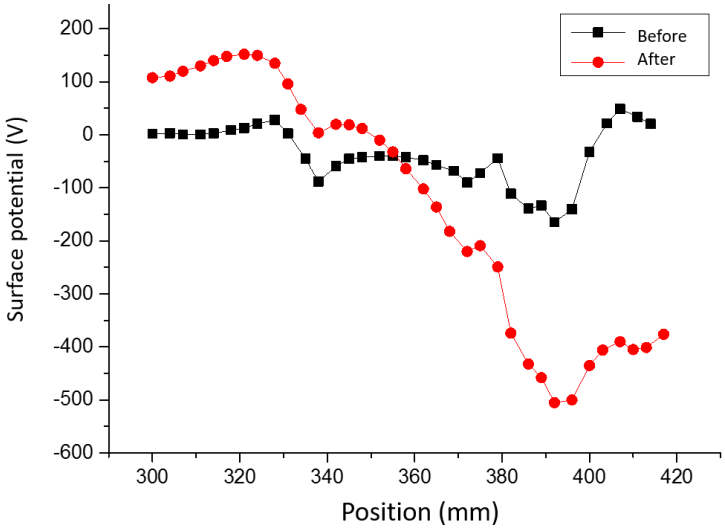

(a)

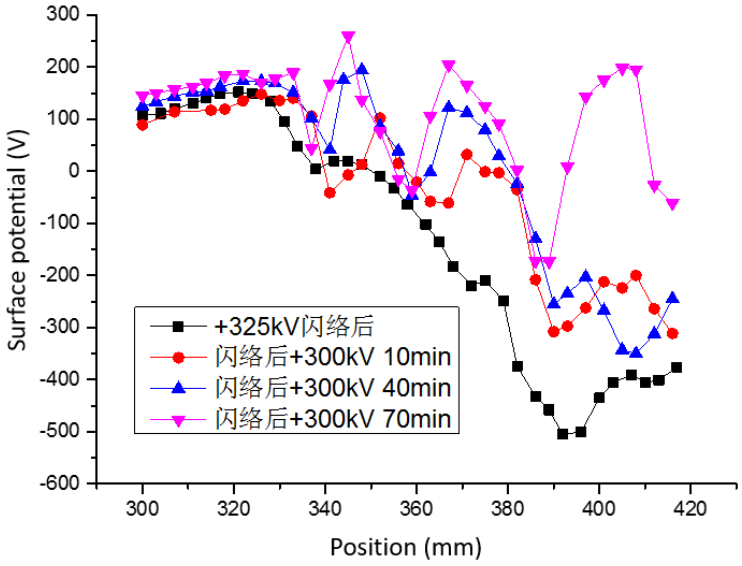

(b)

Figure 6-14：Variation of surface potential during and after two spark discharges between the contact gap. a) Comparison of distribution before and after spark; b) surface potential variation under an applied voltage of 300 kV. The curve labelled "before" is the result following the 13-hour charge relaxation period, given in Figure 6-13.

Theoretically speaking, the occurrence of a spark discharge nearby the insulator has two consequences. Firstly, there is abundance of positive and negative charges appearing in the gas for a limited time. Secondly, the conductivity of the gas will be changed. This means a flux of positive or negative charges will be formed immediately by the insulator surface depending on the local direction of the electric field. The tendency to attract opposite charges by the charges on the surface will have the effect of smoothening the charge distribution on the surface, therefore the potential distribution. Figure 6-15 show that higher potential distribution appears on the surface following another spark at 324 kV. Another important difference is that a rather smoothly changing high voltage peak occurs near the high voltage electrode. Within 30 minutes of further application of a 300-kV voltage, the peak slightly moves towards the high voltage electrode while slightly reducing its peak value. Again, this is a result of the drift of charges in the applied electric field.

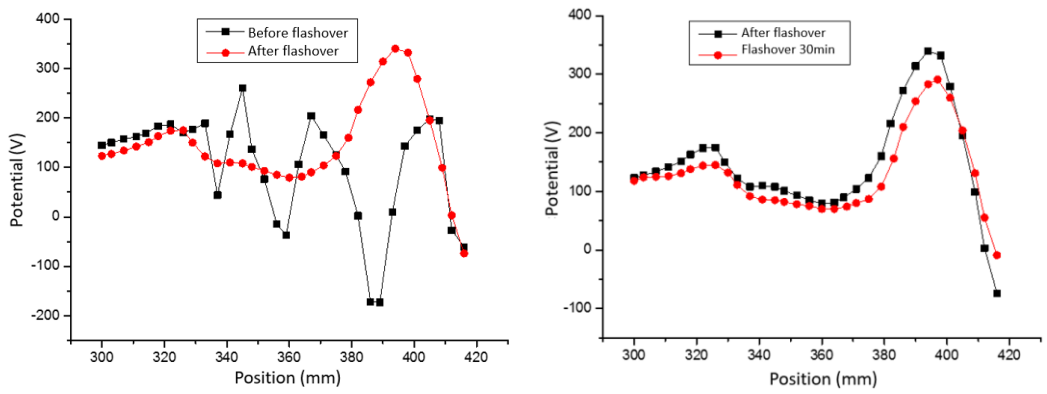

Figure 6-15: Change of potential distribution on insulator surface along the 0^o line due to spark distribution at 324 kV.

C. Effect of Changing Polarity of Applied Voltage and Spark at Negative Polarity

Results on the variation of potential distribution on the insulator surface due to spark at positive polarity have been obtained. In this section, we present the results on the change of potential distribution due to polarity reversal and spark at negative polarity.

Results in Figure 6-16 show that in 30 minutes of polarity reversal, there is already substantial change of potential at the middle length of the insulator, from 90 V to -100 V. In another 30 minutes, the peak potential value near the negative electrode drops from 290 V to 50 V.

Following another of polarity reversal, the voltage was increased negatively and a spark occurred at 325 kV. Compared with the positive polarity spark, the spark voltage stays more or less the same. However, the most apparent difference is that the spark at negative polarity results in much more accumulation of surface charge than in the positive case. The negative peak voltage reaches -1600 V at the middle length of the insulator (Figure 6-17).

Charge relaxation experiment was also carried out after the application of negative voltage, as shown in Figure 6-18. Since the potential distribution is rather smooth, it is possible to obtain a more accurate relaxation time for the charges. Assuming a constant relaxation time for all charges on the surface, using the potential values at location of 370 mm in Figure 6-18, we obtained a value of 26 hours, which is much longer than the situation following positive voltage application.

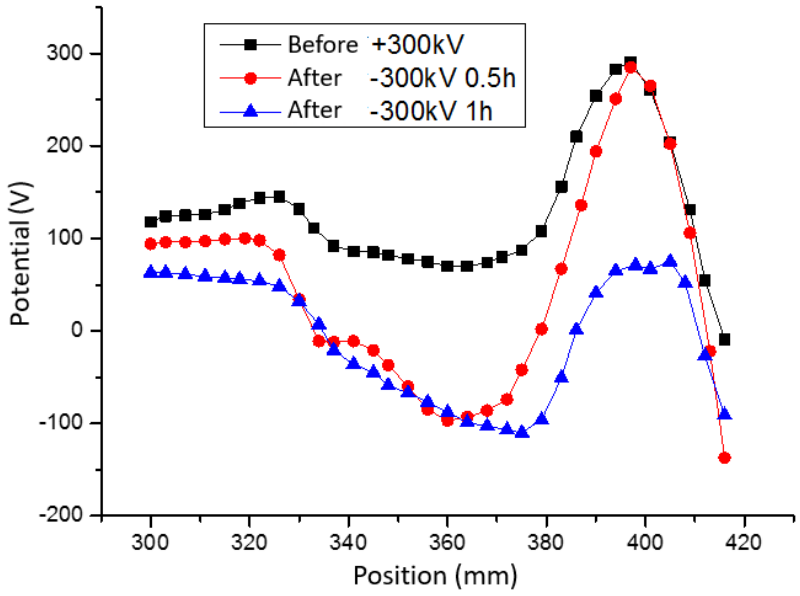

Figure 6-16 Variation of surface potential at 0º line due to polarity change from 300 kV to -300 kV.

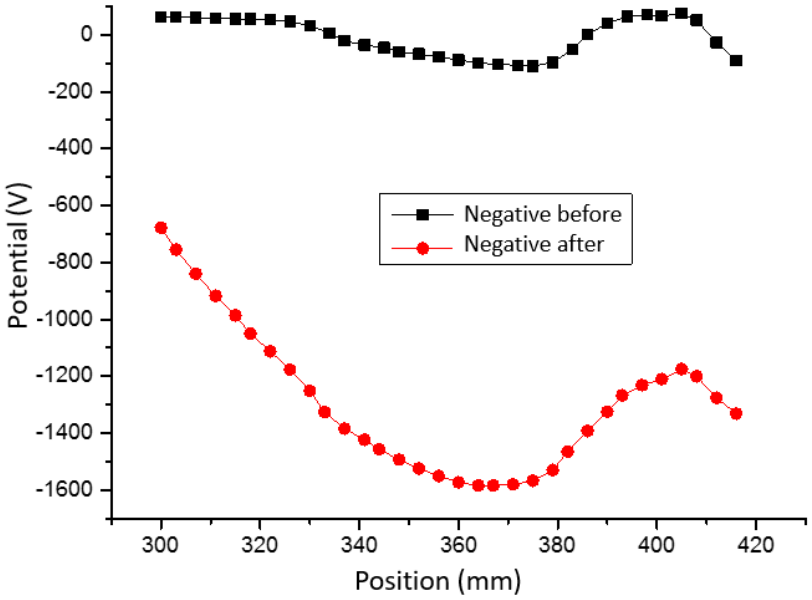

Figure 6-17 Variation of surface potential distribution at 0º line due to spark at negative polarity at -325 kV.

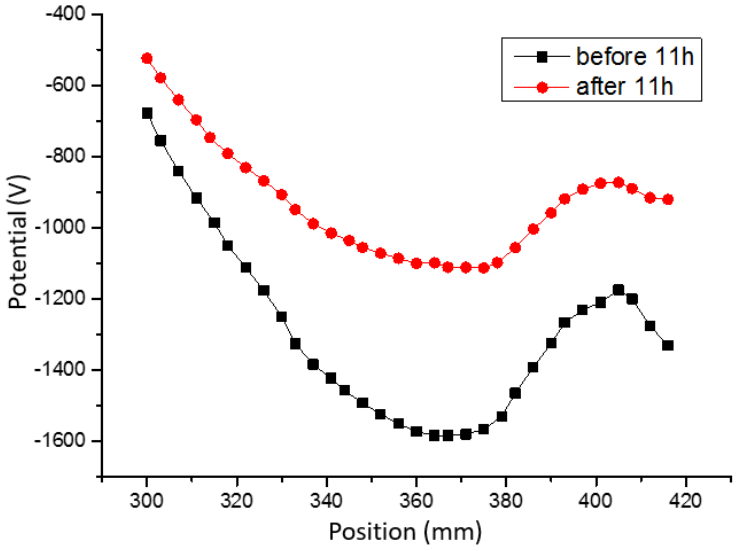

Figure 6-18: Variation of surface potential distribution along the 0º line due to charge relaxation over a period of 11 hours. The initial value is the potential distribution given in Figure 6-17.

6.3.3 Experiment with SF_6 at Increased Pressure at 4 bar

A. Test of Positive DC Voltage

The pressure of SF_6 used was 4 bar absolute. The experiment was performed under two voltage levels, the first one is 200 kV and the second voltage level is 300 kV. The voltage was increased to 300 kV after 200 kV application as listed in Table 6-5. The insulator was the same.

The first difference from the results is that by increasing the pressure to 4 bar, surface charge accumulation becomes weak with a maximum potential of 30 V and - 30 V. the distribution now exhibits more smoothness.

Table 6-5 SF_6 experiment, 4.1 bar, the applied voltage is 200 kV and 300 kV.

Test number	Applied voltage /kV	Duration time/h	Total applied time/h
1	+200	0.5	0.5
2	+200	0.5	1.0
3	+300	0.5	1.5
4	+300	0.5	2.0

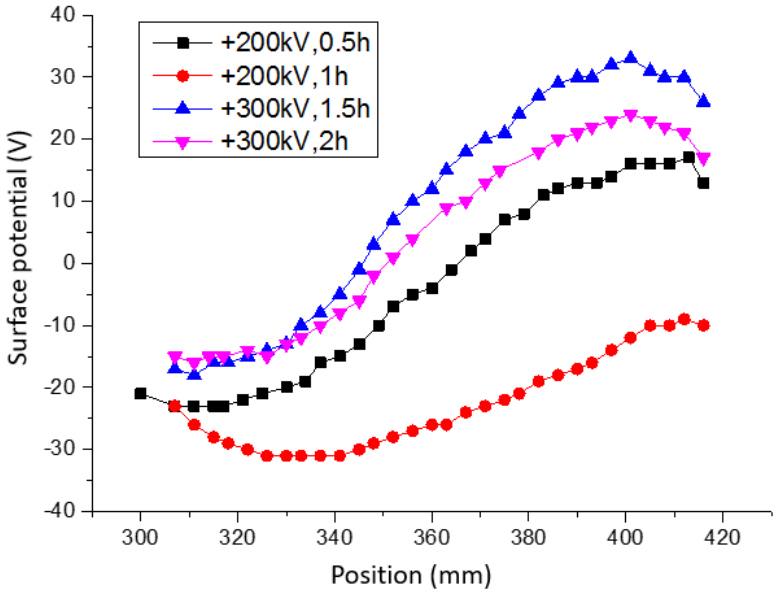

Figure 6-19: Surface potential distribution along the line of 0º in SF6 at 4.1 bar with different applied voltage.

Increasing the applied voltage to 400 kV at the end of the first 2-hour period of voltage application, the potential changes first near the high voltage electrode, as shown in Figure 6-19. It is expected that at high pressure, partial discharge in the gas is much more reduced and transport to the insulator surface from within the gas is drastically reduced. Therefore, charge accumulation on the insulator surface is more controlled by charge injection from the electrode. In one of the initial diagnostic experiments using ultra violet camera, it was found that there was discharge at the triple junction of the insulator at the high voltage side. Despite the improvement and cleaning, there will still be discharges close to the triple junction. This may be responsible for the potential behavior when the pressure is increased.

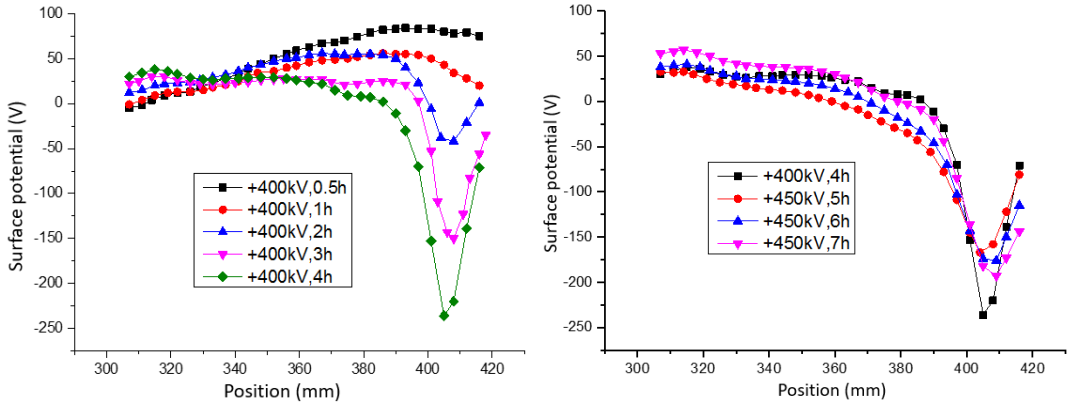

Figure 6-20 Surface potential distribution in SF6 at 4.1 bar along the line of 0º with applied voltage of 400 kV and 450 kV.

On the conclusion of the 7-hour application of voltage of 400 kV and 450 kV, as can be seen in Figure 6-20, another 9 hours of continuous voltage application is applied to find out the long-term change of surface potential, which is shown in Figure 6-21. The change is substantial and increased negative voltage gradually spread towards the earthed electrode.

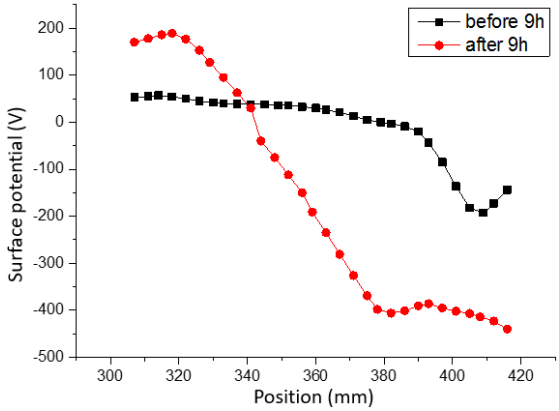

Figure 6-21 Surface potential variation during long time of voltage application.

B. Test of Polarity Reversal (-450 kV) in SF_6 at 4.1 bar

On the conclusion of the 9 hour long continuous voltage application as shown in Figure

6-21，the polarity was reversed and the voltage became -450 kV. The measurement arrangement is given in Table 6-6. Results in Figure 6-22 show that after the polarity reversal. The potential on the surface near the earthed electrode starts to change towards the opposite direction. It takes 4.5 hours to change its polarity. On the half length of the insulator on the high voltage electrode side, potential remains negative. Extending the voltage application for another 11 hours, the accumulated charges induce negative potential on the whole line at 0^{o}.

Finally, after the long-term application of negative voltage, another polarity reversal was done, from -450V to 450V. It can be seen from Figure 6-23 and Figure 6-24 that the most affected surface area is near the high voltage electrode, from negative voltage to positive voltage in 0.5 hour.

Table 6-6 Polarity reversal in SF_6 experiment at 4.1 bar, the applied voltage is - 450 kV.

Test number	Applied voltage /kV	Duration time /h	Total applied time/h
1	-450	0.5	0.5
2	-450	1.0	1.5
3	-450	1.0	2.5
4	-450	1.0	3.5
5	-450	1.0	4.5

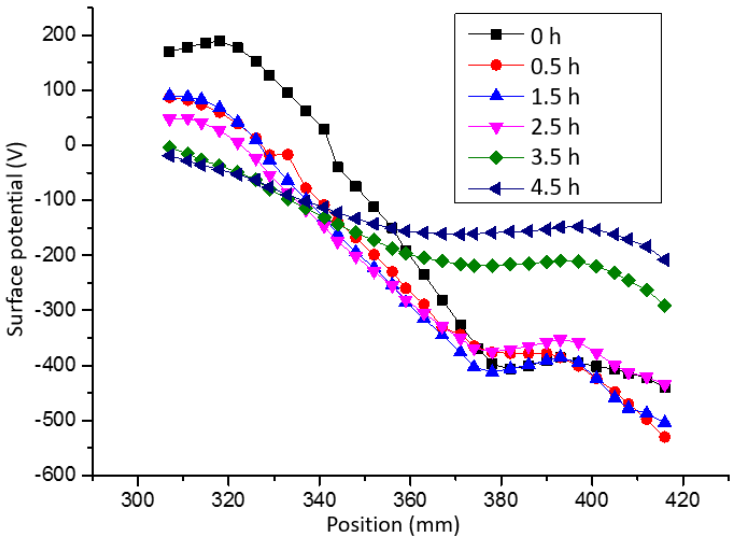

Figure 6-22 Surface potential distribution after polarity reversal (SF6, 4.1 bar, 450 kV to -450 kV, 0). The curve labelled as 0 h means the distribution before polarity reversal.

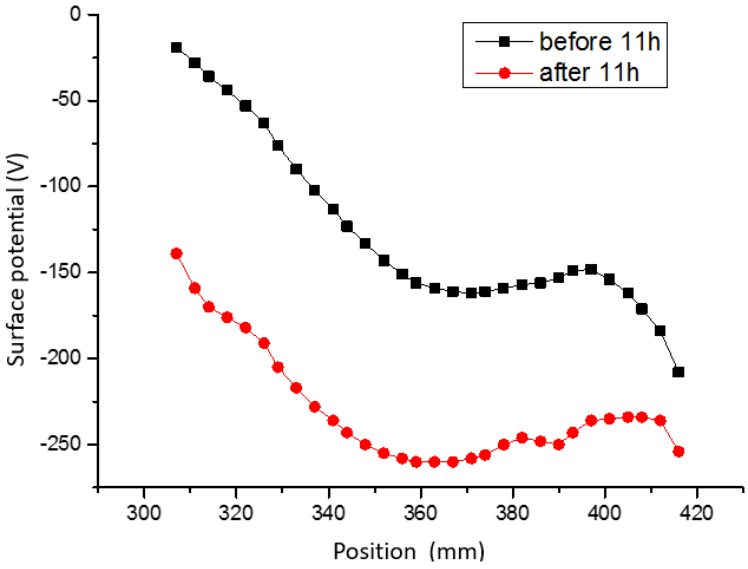

Figure 6-23 Surface potential distribution after polarity reversal for an extend period of 11 hours. Conditions are the same as in Figure 6-22.

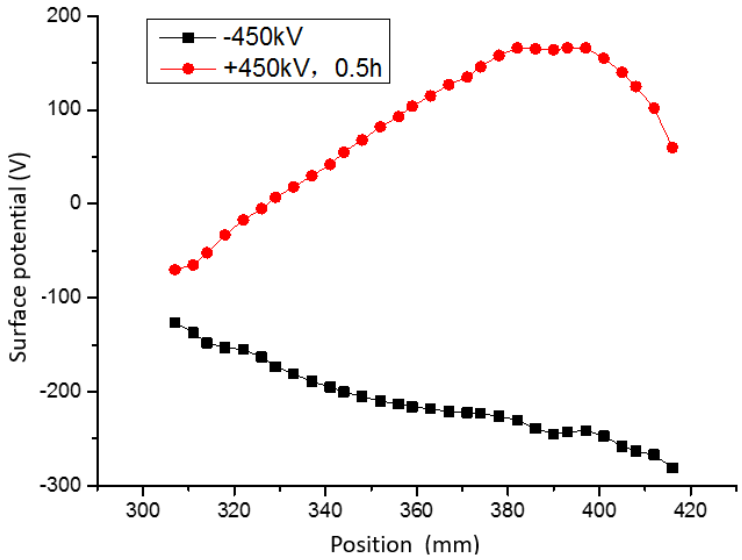

Figure 6-24 Surface potential distribution after polarity reversal from -450 kV to 450 kV along the 0o line.

6.3.3 Experiment with CO_2

Measurement of surface potential distribution in CO_2 was also made because SF_6 has been used as the buffer gas in the mixture of CO_2 with C_4F_7N and $C_5F_{10}O$ to replace SF_6 which is a strong global warming gas. The pressure of CO_2 is 4 bar. Another insulator of the same design was used in this experiment.

Potential measurement was taken before the application of HVDC voltage with results given in Figure 6-25. The surface charge is minimal inducing a maximum potential of 35 V. again the charge is not uniformly distributed around the azimuthal direction of the insulator.

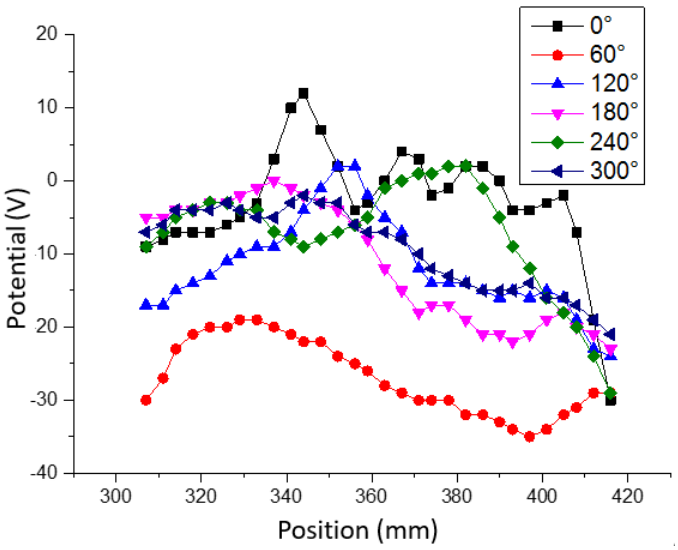

Figure 6-25 Potential distribution along lines at different azimuthal angles on the insulator surface in CO_2 at 4 bar.

With the application of 200 kV HVDC voltage, the potential on the whole line at 0° becomes positive, as shown in Figure 6-26. The potential grows to 200 V in 1 hours at 200 kV. Further increasing the voltage to 300 kV leads to an increase of 50 V in 0.5 hour. The voltage was further increased to 400 kV and a spark developed in 1 minute. A comparison of the potential distribution is given in Figure 6-27. It shows that the effect of spark discharge on surface charge accumulation is similar for N_2 and CO_2, while for SF_6 it is very different.

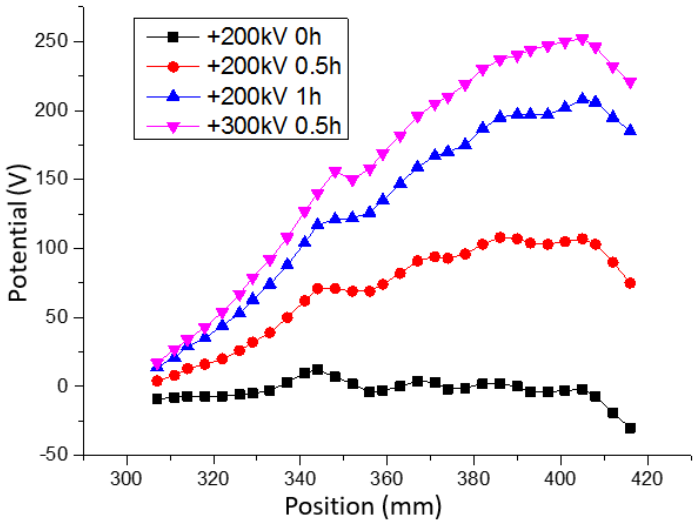

Figure 6-26 Potential distribution along the 0º line on the insulator surface at 200 kV and 300 kV.

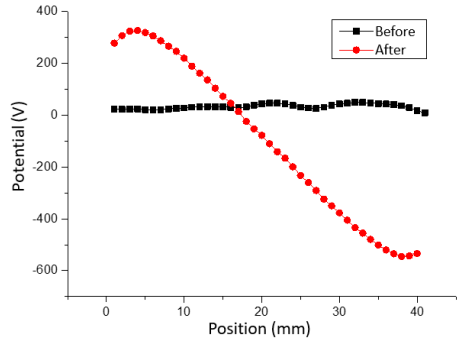

(a)Nitrogen (N_2), 150 kV, 1bar

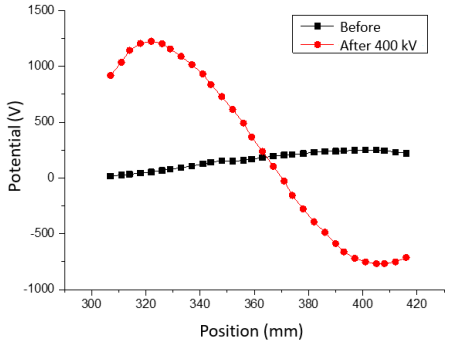

(b) CO_2 , 400 kV, 4 bar

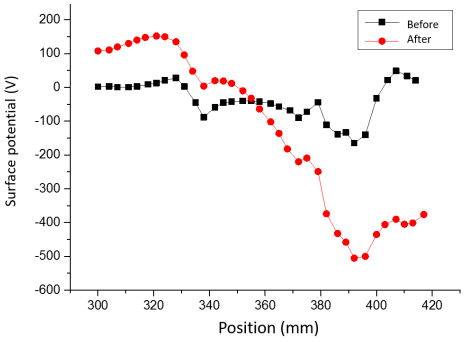

(c) SF_6, spark at 325 kV at 1 bar.

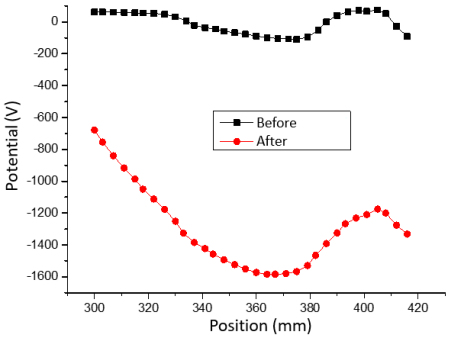

(d) Negative 325 kV, 1 bar

Figure 6-27 Comparison of surface potential distribution change following a spark discharge in different gases.

6.4 Discussion and Summary

Surface potential measurements were taken on the epoxy insulator for different gaseous environment. There is no attempt to convert the potential distribution to surface charge distribution due to the highly irregularity of the potential distribution. Presenting the potential distribution results enables a true representation of the real discharge situation and possible future interpretation of the results.

The most important feature of the work in this chapter is the findings of the role of spark discharge in the gaseous environment on the potential and surface charge distribution on the insulator surface. A spark discharge can drastically change the potential distribution on the insulator surface as a result of the short time appearance of the high charge number in the gas. An intensive spark leads to smooth distribution of surface potential at substantially increased values.

Results also show that spark in N_2 and CO_2 leads to rather similar distribution of potential along the axial line on the surface. The charge relaxation time is estimated based on the assumption of uniform charge relaxation over the insulator surface and exponential delay in potential during the relaxation period. It is in the range of 9 - 26 hours. This is only approximate because of the assumption. Nevertheless, it gives a good indication of the order of magnitude of the relaxation time. More work can be done, if time allowed, to attempt to obtain the surface charge distribution by applying a conversion method.

CHAPTER 7 CONCLUSION AND FUTURE WORK

7.1 Summary of Work

A steady state charge transport model for epoxy insulators used in HVDC applications has been developed and verified in the present work. Charges in gases of high electron affinity appear in the form of ions, both positive and negative. The most important feature of this model is the modelling of the ion transport mechanism in gas, in terms of conservation of the ion number. Results in Chapter 5 have shown that upon the application of a high DC voltage, the number density distribution in the region surrounding the insulator will be re-distributed with values of 3 orders of magnitude lower than the equilibrium ion number density in the absence of electric field. The drastic deviation of the ion number densities from their equilibrium value leads to the invalidity of the concept of electrical conductivity in the gas domain. This is because the ability to conduct electricity in the gas is no longer a material property.

Computational accuracy is always an important issue. A significant amount of effort has been spent to study the influence of mesh size and artificial diffusion to promote convergence. It has been found that the convergence of the computation using Finite Element Method is very sensitive to the settings for the boundary conditions. The triple junction is the point that causes computation divergence if its extreme electric field is not shielded.

The model has been verified by experimental results in different gases and at different voltage levels. All model parameters are carefully examined based on literature review and wherever possible measured values are used. Good agreement has been obtained between our model results and the experimental results, showing the validity of the model.

7.2 Conclusions

The following conclusions can be arrived at from the present work:

1) In strong electric field (but not leading to high electron number density), the number density distribution of ions in the gas is highly non-uniform and varies by several orders of magnitude. The concept of electrical conductivity as a material property becomes invalid. However, we can still derive an "effective electrical conductivity" from the results and the local electric field.
2) The polarity of accumulated surface charge depends not only on the shape of the insulator but also on the relative largeness of the effective electrical conductivity of the gas and that in the solid insulation material near the insulator surface. When the gas has a much lower electrical conductivity, positive charges are likely to appear on most of the insulator surface.
3) The system is nonlinear due to the ionization and recombination of ions. Its effect increases with the applied voltage because at higher voltage the effect of the nonlinear recombination term is magnified through the enhanced electric field.
4) Shielding of the triple junction is necessary in product design. However improper design of the shape of the shield can induce strong side effect by increasing the total field strength locally near the edge of the shield.

The experimental investigation conducted in Chapter 6 provides useful information on the effect of spark discharge on the distribution of surface potential. Our results show that

5) In the presence of moderate partial discharge around the insulator, the surface potential (also surface charge) exhibits highly non-uniform distribution in the azimuthal direction. This non-uniformity is less severe at the middle section of the insulator. Therefore, in the design of HVDC insulators, we need to always take this type of non-uniformity into account.
6) The presence of a spark discharge near the insulator surface leads to significant change and rapid re-distribution of the surface charge density. There is indication in the results that part of the surface that is directly exposed to the path of the spark discharge is much more affected than that is hidden away.
7) For the epoxy insulator used in the study, a charge relaxation time of 9-26 hours

is estimated for epoxy insulator in SF_6 at 4 bar.

7.3 Limitations and Future Work

Computational and experimental investigation of the behaviour of epoxy insulators used for HVDC wall bushings has been carried out. There are a number of limitations. Further work can be carried out to enhance the applicability of the model.

1) The properties of positive and negative ions in SF_6 gas are given different values in different publications. No values are available for the experimental cases used for model verification. We have used the best possible value from the literature. This might lead to some uncertainty in the computational results.
2) The electrical conductivity values of the epoxy material is assumed constant in the present work. In reality, there will be a temperature distribution. The coupled modelling of the thermal field and electric field is necessary in the modelling of insulators operating in a real network where load current leads to temperature rise. The modelling can however take huge amount of computational time using fine meshes. This can be part of the future work.
3) Charge trapping inside the epoxy material is not considered in the model because my focus in the present work is on charge accumulation on the surface in steady state. The extension of the mode into a transient model considering charge trapping inside the material will make it a much more powerful tool to predict the ageing of the insulation material under DC stress.

LIST OF PUBLICATIONS

Q. Liu et al., “Charge Transport and Accumulation around a Spacer Insulator for Application in HVDC Wall Bushing.”, accepted by IEEE Transactions on Dielectrics and Electrical Insulation, 2017.

Q. Liu et al., "A Model for Charge Transport around Insulator under HVDC Stress", published in Proceedings of the 13th International Electrical Insulation Conference, Birmingham, UK, 2017.

Q. Liu et al., "Charge Transport and Accumulation around a Spacer Insulator in an HVDC Wall Bushing", published in Proceedings of the 21st International Conference on Gas Discharges and Their Applications, Nagoya, Japan, 2016.